Ionic transport in atomic and nano-dimensional structures in oxides

Harald Fjeld

Dissertation for the degree
of Philosophiae Doctor

Department of Chemistry
Faculty of Mathematics and Natural Sciences
University of Oslo

2010

Preface

This thesis represents parts of the requirements for the degree of Philosophiae Doctor (Ph.D.) at the University of Oslo. The doctoral scholarship was funded by the Department of Chemistry during the period of February 2006 to March 2010, of which one year was devoted to teaching obligations.

I would like to thank Truls Norby and Reidar Haugsrud for excellent guidance as supervisors. Your scientific knowledge and advices, encouragement, and fast and constructive feedback during manuscript writing have been of the greatest importance. I am also thankful to co-supervisor Svein Stølen who brought valuable contributions to the understanding of second order phase transitions and Landau theory.

I would also like to acknowledge the people at the Group for Solid-State Electrochemistry for creating an inspiring working environment where it is easy to feel comfortable. In particular, I have really enjoyed the office cohabitation together with Christian Kjølseth, in which numerous nice scientific and other valuable discussions have taken place. Kazuaki Toyoura, Demie Kepaptsoglou and Anette Gunnæs: thanks for your contributions and for being easy to cooperate with.

I am very grateful to my mother, father, brother and grandfather for providing crucial insight into the important aspects of life. I have learned a lot from you.

Finally, I would like to thank Helle for your love, positivism and understanding. You have truly been fantastic the last months.

Oslo, May 2010

Harald Fjeld

Contents

Summary

Oxides with high ionic conductivity represent a class of functional materials with characteristics suitable for electrochemical energy converters, such as fuel cells and batteries. This work addresses effects from changes in crystal structure and of grain boundaries on the ionic transport properties in different oxide materials.

Defects are a prerequisite for transport of charged species in solids, and in this thesis defect chemistry is the theoretical foundation. The first part describes the formation of defects and important aspects for the transport of charged species in the grain interior of oxides. Relevant literature is reviewed in the second part, emphasising various effects of interfaces on transport processes.

The gradual change in the crystal structure of the high temperature proton conductor $LaNbO_4$ through a second order phase transition and its relation to the activation enthalpy of mobility of protons were studied by means of first principles calculations and conductivity measurements. Above the transition temperature, the proton conductivity curve displayed Arrhenius-type behaviour, yielding an activation enthalpy of the mobility of protons of 35 kJ mol^{-1}. At the onset of and through the second-order phase transition the conductivity dropped off steeply, followed by a less steep decrease towards lower temperatures. This was interpreted as a gradual increase in the activation enthalpy with increasing degree of distortion of the crystal structure, reaching ~ 57 kJ mol^{-1} at 205 °C. The experimentally determined values were in agreement with the computational investigation, where activation enthalpies were determined to 39 and 60 kJ mol^{-1} in tetragonal and monoclinic $LaNbO_4$, respectively.

The intrinsic transport properties of the grain boundaries in many ceramics have previously been accounted for by a space-charge model. The model predicts depletion of positive charge carriers and accumulation of negative charge carriers in the space-charge layers adjacent to a positively charged core, which explains why many ionic conductors exhibit high intrinsic grain boundary resistance. Here, we have applied the model to analyse the transport properties of the grain boundaries in $BaZrO_3$, $LaNbO_4$ and $Er_2Ti_2O_7$ (all acceptor doped).

The pO_2-dependencies of the conductivity of acceptor doped $BaZrO_3$ indicated dominating ionic and mixed ionic and p-type electronic conduction for the grain interior under reducing and oxidizing conditions, respectively, while the grain boundaries showed an additional n-type electronic contribution under reducing conditions. Transmission electron microscopy revealed enrichment of Y in the grain boundary region. These findings indicate the existence of space-charge layers in the grain boundaries. Assuming a constant level of acceptors

through the space-charge layer (the so-called Mott-Schottky approximation), a space-charge potential of 0.5–0.6 V was obtained at 250 °C in wet oxygen.

An increase in the grain boundary conductivity upon a D to H isotope exchange under isothermal conditions, and a positive pH_2O dependency after quenching from different pH_2O made us conclude that protons were the major charge carrier in the grain boundaries of acceptor doped $LaNbO_4$. The higher functional pH_2O dependency of the conductivity of the grain boundaries as compared to grain interior suggested that protons were relatively more predominating as charge carriers in the grain boundaries than in the grain interiors. This behaviour was rationalised by noting that in the space-charge layers, doubly charged oxygen vacancies exhibit a quadratic decay compared to singly charged protons. Using a Mott-Schottky approximation, a space-charge potential of 0.66 V was obtained at 250 °C for this material.

The electrical properties of ceramics of $(Er_{1-x}Ca_x)_2Ti_2O_{7-x}$ (x = 0.02 and 0.005) with low and high contents of Si impurities at the grain boundaries were investigated by impedance spectroscopy as a function of pO_2, pH_2O and pD_2O in the temperature range 300 – 800 °C. For the grain interior, oxygen vacancies are the major charge carrier, with protons as a minor contributor at the lower temperatures. In the grain boundaries – as compared to grain interior – the singly charged protons were relatively more predominating than the doubly charged oxygen vacancies, again suggesting that negatively charged space-charge layers govern the electrical properties. In support of this, the samples with a lower content of Si in the grain boundaries exhibited an electrical response essentially similar to those containing more Si and even a secondary Si-rich phase.

The electrical response of $Er_2Ti_2O_7$ contained an additional impedance – the third in the Nyquist plots – which was suggested to be caused by chemical polarization of the mixed oxide ion and proton conducting grain interiors induced by blocking of oxygen vacancies at the grain boundaries. This was supported by the tear-drop shape of this contribution, the different response on the characteristic frequency when changing either pH_2O or the hydrogen isotope in the surrounding gas, and a good agreement between the experimentally and calculated value for the chemical capacitance.

All together, the electrical characterisations which were carried out on $BaZrO_3$, $LaNbO_4$ and $Er_2Ti_2O_7$ suggest that the grain boundary core-space-charge layer model can be well applied to oxides that conduct protons. The theory of chemical polarization induced by grain boundaries was applied on $Er_2Ti_2O_7$, which, as we see it, provides a first application of this theory on a mixed oxide ion and protonic conductor.

1. Introduction

Functional materials are crucial for everyday life as we know it in the 21st century. To justify such an airy statement, let us consider a few examples from modern consumer technology. In all types of electronics we find silicon transistors. Microwave dielectric materials are used in wireless communication for transmission of signals. Ga-based light emitting diodes find applications in display technology and, finally, transition metal oxides serve as the cathode in lithium-ion batteries. While these materials certainly differ in terms of applications, a common feature is that their defect chemistry is decisive for their properties.

In this thesis, defect chemistry makes up the theoretical foundation. Defect chemistry concerns the thermodynamic description of defects under equilibrium conditions, as well as the kinetics of the defect reactions. Both are important to understand in order to deal with electrical properties of materials, which, from an application point of view, are important for all of the above mentioned materials.

A wide range of solid oxides are known to conduct various types of charged species, both ionic (*e.g.* oxide ions and protons) and electronic (electrons and electron holes). Solid state ionics, which is an interdisciplinary research area where inorganic and physical chemistry as well as materials physics cross, concerns the thermodynamic description of the concentration of charge carriers and the mobility of the charge carriers in ionic solids. It therefore follows that defect chemistry is an important tool in solid state ionics.

This work focuses on ionic transport in solid oxides. Oxides with high and dominating ionic conductivity – which we may refer to as solid electrolytes – represent a class of functional materials with characteristics suitable for electrochemical energy converters, such as batteries and fuel cells. To achieve high conductivity, which is the key factor for high performance of such devices, the oxide should exhibit both high concentration and high mobility of the ionic charge carrier. A profound understanding of these phenomena will pave the way for better electrochemical energy converters, which may have beneficial impact on society's use of energy.

In oxides, as well as in other solids, ionic charge carriers migrate by activated diffusion. The temperature dependence of the mobility of an ionic charge carrier is related to the activation enthalpy of mobility, which is the parameter that in gross terms determines the mobility. Given that the structure is unaltered, the activation enthalpy of mobility is considered as constant throughout a temperature range. The impact of first order phase transformations on the transport properties is known for different classes of ionic conductors. A giant change in the charge carrier mobility while crossing the transformation temperature, ascribed to a

decrease in the activation enthalpy of mobility, occurs for *e.g.* AgI [1,2], Bi_2O_3 [3,4] and $CsHSO_4$ [5,6], whose ionic charge carriers are silver ions, oxide ions and protons, respectively. With respect to second order phase transitions and possible effects on mobility, the literature is scarce. Part of this work involves studies of the gradual change in the crystal structure of the high temperature proton conductor $LaNbO_4$ through a second order phase transition and its relation to the activation enthalpy of mobility of protons. How to interpret the conductivity data constitutes an important part.

In polycrystalline materials ions migrate through grain interior and across grain boundaries. It is recognized that grain boundaries of ionic conductors can exhibit an inherently low conductivity, even for high-purity materials, *e.g.* ZrO_2 [7,8], CeO_2 [9,10], $LaGaO_3$ [11] and $BaCeO_3$ [12] (all acceptor doped). For the already mentioned oxide ion conductors, the inherently low grain boundary conductivity originates from depletion of oxygen vacancies in the vicinity of the positively charged grain boundary core, the so-called space-charge effect. It was, therefore, of interest to apply this grain boundary core-space-charge layer model on proton conductors with low grain boundary conductivity. The investigations related to this effect conducted on the high temperature proton conductors $BaZrO_3$ and $LaNbO_4$ stand central in this thesis. Here we consider and discuss possible implications on the grain boundary defect situation arising from the fact that the concentration of the major charge carrier is dependent on water vapour pressure.

Interfaces introduce additional degrees of freedom when tailoring properties of materials. One interesting effect appears when two crystal lattices with different symmetry and/or different lattice parameters are joined. Then strain fields may develop in the interfacial region, and a conductivity enhancement up to two orders of magnitude was reported for the multilayer system consisting of Ca-doped ZrO_2 and Al_2O_3 [13]. The lower activation energy for the ionic interfacial conductivity suggests a higher ionic mobility in the disordered core regions than in bulk. The presence of interfaces may also change the overall transport properties from what is encountered in bulk. In the oxide ion conductor $Er_2Ti_2O_7$ it appears, for instance, that protons play an important role for the electrical properties of the grain boundaries. The discussion of this phenomenon in $Er_2Ti_2O_7$ constitutes the third and final topic in this thesis.

The thesis is based on five manuscripts that describe the results of five investigations. They have in common that they all are devoted to ionic transport in oxides. Before presenting those manuscripts, an introductory part will be given. In that part, relevant theory along with a literature review will be presented, hopefully making us well prepared for the forthcoming chapters. The experimental part should be considered as supplementary to what is given in the manuscripts. Here, special emphasis will be put on the electrical measurements, *i.e.*

impedance spectroscopy – both in terms of experimental details and fitting of data – because this is the main technique for the experimental work in this thesis. Then, the most important results are presented and discussed in the five manuscripts. Finally, a broader discussion covering four of the five investigations will be provided, taking further advantage of the introductory part. The manuscripts have been finished at rather different times, and the overall discussion will hopefully bring them together and allow for synergy and new insight.

2. Transport in ionic solids

This chapter deals with the fundamentals of transport of charged species in ionic solids. Central for this topic are defects, as their presence is a prerequisite for transport of charged species in solids. In such a broad sense, the term defect constitutes both ionic point defects and electronic defects (electrons and electron holes). We therefore start our treatment of transport of charged species by describing how defects form and introduce the thermodynamic framework that is used in defect chemistry.

In this thesis, the focus is on ionic transport in oxides. Many aspects of transport in solids are therefore not covered, and the examples provided are chosen to describe the relevant materials for this work. In this chapter we restrict ourselves to transport in the grain interiors. Chapter 3 deals with interfaces and some of the numerous aspects that interfaces introduce to transport of ionic charge carriers.

2.1 Point defects

In the grain interior of oxides, transport of ionic charge carriers only takes place in the presence of point defects. Point defects may be formed with or without neighbouring phases – such as surrounding oxygen gas – involved, and the processes are termed internal and external defect reactions, respectively.

2.1.1 Internal defect equilibria

Typical examples of internal defect reactions are Schottky and Frenkel disorders. Another example encountered in pyrochlore structured oxides is the site exchange reaction of the cations [14,15] (below written for $Er_2Ti_2O_7$ using Kröger-Vink notation)

$$Er_{Er}^{x} + Ti_{Ti}^{x} = Er_{Ti}^{/} + Ti_{Er}^{\bullet}. \qquad (1)$$

If we assume ideal conditions, *i.e.* defect concentrations are so low that they do not interact with each other, and that all sites are energetically equal, we can write the mass action law according to

$$K_{se} = X_{Er_{Ti}^{/}} X_{Ti_{Er}^{\bullet}} = \frac{\left[Er_{Ti}^{/}\right]}{\left[Ti\right]} \frac{\left[Ti_{Er}^{\bullet}\right]}{\left[Er\right]}. \qquad (2)$$

Here K_{se} denotes the equilibrium constant of the site exchange reaction, X site fractions and square brackets concentration of species. If we express the concentrations of species in terms of mole fractions, we obtain in the case of $Er_2Ti_2O_7$, [Er] = [Ti] = 2. Then, Eq. 2 equals

$$K_{se} = \frac{1}{4}\left[Er'_{Ti}\right]\left[Ti^{\bullet}_{Er}\right]. \quad (3)$$

Only when the concentrations of defects are expressed in terms of site fractions or properly converted into mole fractions as shown above, the equilibrium constant is directly related to the standard molar Gibbs energy of the defect reaction through $\Delta_d G^0 = -RT \ln K_d$, where the d subscript denotes a defect chemical reaction in general. $\Delta_d G^0$ is related to the standard molar enthalpy $\Delta_d H^0$ and entropy $\Delta_d S^0$ of the defect reaction through $\Delta_d G^0 = \Delta_d H^0 - T\Delta_d S^0$. This, in turn, allows us to write useful expressions relating the defect concentrations and their corresponding thermodynamic parameters, for example:

$$\frac{1}{4}\left[Er'_{Ti}\right]\left[Ti^{\bullet}_{Er}\right] = \exp\left(\frac{\Delta_{se}S^0}{R}\right)\exp\left(-\frac{\Delta_{se}H^0}{RT}\right). \quad (4)$$

At this point we should stress that the entropy term in Eq. 4 does not contain any configurational contributions[1], but rather consists of vibrational contributions only. Whereas $\Delta_d H^0$ is always a positive value for all internal defect reactions (due to breaking of bonds), $\Delta_d S^0$ may take both positive and negative numbers. Usually, when a vacancy is created, $\Delta_d S^0$ is positive and when an interstitial is created, $\Delta_d S^0$ is negative [16] (Sec. 5.2, p 116). This implies that formation of interstitial defects is additionally opposed by the reduction of vibrational entropy whereas the opposite is true for the formation of vacancies.

Because of the tremendous configurational entropy gain from the formation of point defects – as compared to the perfect crystal – all solids contain point defects to some extent. In Fig. 2.1 the defect concentration in our defect chemical example is plotted as a function of inverse temperature for a set of formation enthalpies and entropies.

[1] The configurational entropy is equal to the equilibrium constant when written properly. It is the balance between the configurational entropy and the enthalpy and entropy change of the defect reaction that determines the minima of the defect concentrations.

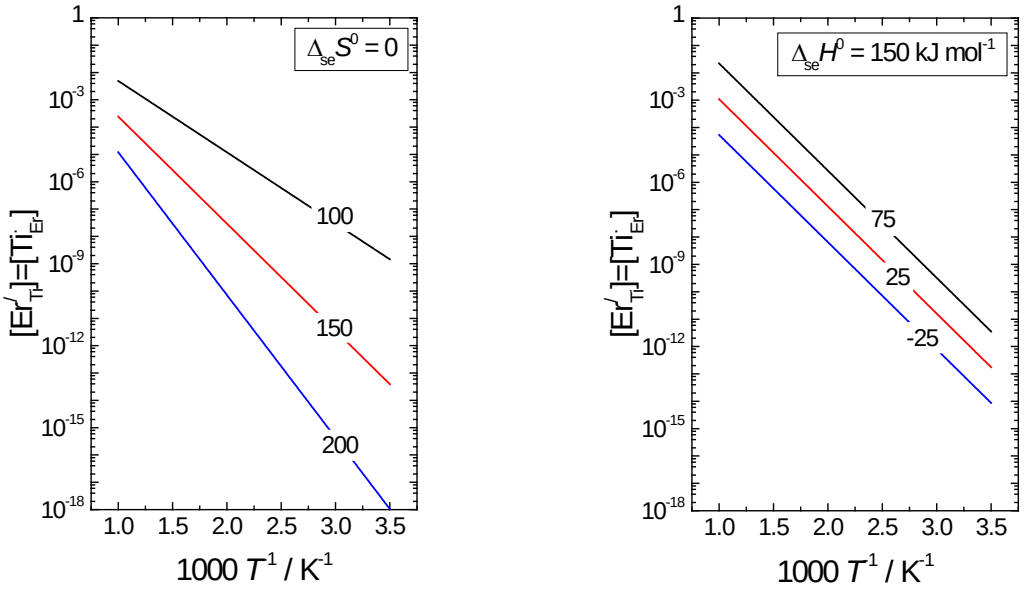

Fig. 2.1. Calculated defect concentrations (mole fractions) of Er'_{Ti} and $Ti^{\bullet}_{Er}$ as a function of inverse temperature. Left: $\Delta_{se}S^0$ is kept constant and $\Delta_{se}H^0$ varies as indicated in the figure. Right: $\Delta_{se}H^0$ is kept constant and $\Delta_{se}S^0$ varies as indicated in the figure.

The positive $\Delta_{se}H^0$ results in an increasing defect concentration with increasing temperature. We also observe that the defects are stabilized at a given temperature with increasing $\Delta_{se}S^0$. Finally, we may note that at room temperature these sets of thermodynamic parameters yield defect concentrations that are so low that extrinsic sources (dopants or impurities) for sure will dominate over the intrinsic defects.

2.1.2 External defect equilibria and doping effects

The formation of a fully ionised oxygen vacancy can be written equilibria

$$O_O^x = V_O^{\bullet\bullet} + 2e' + \frac{1}{2}O_2(g) \qquad (5)$$

We note that the formation of one oxygen vacancy is accompanied by the formation of two defect electrons and, furthermore, that the concentration of those defects can be changed by altering the oxygen partial pressure, pO_2.[2] The activity of regular species, *e.g.* O_O^x, will from now on be set to 1, which is reasonable for low defect concentrations. Also, when considered convenient, we will from now on allow ourselves to write concentrations of the defects as

[2] The interaction between the oxide and the surrounding oxygen gas can be written in different ways, in Eq. 5 as the formation of oxygen vacancies and electrons. It is equally justified to write the interaction between the oxide and O_2 as $O_i'' + 2h^{\bullet} = \frac{1}{2}O_2(g)$. It is, however, good practise to write defect reactions focusing on the material's major defects.

molar concentrations (per volume).[3] Thus, the square bracket notation can have different meanings (mole fractions or molar concentrations) in different contexts.

In Eq. 5, the defect electron is assumed to be delocalised. In this case, a standard state for the electron is not straightforward to define, and classical statistical thermodynamics can, therefore, not be applied. Here, we have chosen to replace the entropy term with $\mathrm{K}^{/}_{0,\mathrm{O}}$, and the corresponding mass action law of Reaction 5 then reads

$$\mathrm{K}^{/}_{\mathrm{O}} = \left[\mathrm{V}^{\bullet\bullet}_{\mathrm{O}}\right]\left[\mathrm{e}^{/}\right]^2 p\mathrm{O}_2^{1/2} = \mathrm{K}^{/}_{0,\mathrm{O}}\exp\left(-\frac{\Delta_{\mathrm{O}}H}{\mathrm{R}T}\right). \tag{6}$$

We use superscript slash to denote that the defect reaction contains delocalised electrons (or holes). It is expected that the enthalpy term in Eq. 6 is positive, because the reverse of Reaction 6, *i.e.* the oxidation of the oxide, is an exothermic process.

Internally, oxygen vacancies can be formed through an anion Frenkel disorder reaction

$$\mathrm{O}^{\mathrm{x}}_{\mathrm{O}} = \mathrm{V}^{\bullet\bullet}_{\mathrm{O}} + \mathrm{O}^{//}_{\mathrm{i}} \tag{7}$$

with corresponding mass action law

$$\mathrm{K}_{\mathrm{AF}} = \frac{\left[\mathrm{V}^{\bullet\bullet}_{\mathrm{O}}\right]}{\left[\mathrm{O}\right]}\frac{\left[\mathrm{O}^{//}_{\mathrm{i}}\right]}{\left[\mathrm{i}\right]} = \exp\left(\frac{\Delta_{\mathrm{AF}}S^0}{\mathrm{R}}\right)\exp\left(-\frac{\Delta_{\mathrm{AF}}H^0}{\mathrm{R}T}\right). \tag{8}$$

When electrons are exited across the band gap, an electron hole is left behind

$$0 = \mathrm{e}^{/} + \mathrm{h}^{\bullet}. \tag{9}$$

The equilibrium constant for the electronic disorder reaction is

$$\mathrm{K}^{/}_{\mathrm{B}} = \left[\mathrm{e}^{/}\right]\left[\mathrm{h}^{\bullet}\right] = \mathrm{K}^{/}_{0,\mathrm{B}}\exp\left(-\frac{\Delta_{\mathrm{B}}H}{\mathrm{R}T}\right). \tag{10}$$

Let us now find the defect concentrations as a function of $p\mathrm{O}_2$ for an example oxide, whose relevant defect reactions are described in Reactions 5, 7, and 9. Our example oxide can be, for example, a pyrochlore structured rare earth titanate (*e.g.* $\mathrm{Er_2Ti_2O_7}$) where substantial anion Frenkel disorder takes place [14], and which has a fairly reducible cation (Ti^{4+} can be reduced to Ti^{3+}). By aid of the electroneutrality condition,

[3] Using molar concentrations is often convenient, but it should be repeated that the equilibrium constant is directly related to the molar Gibbs energy only if the concentrations of the defects are expressed in terms of site fractions or properly converted into mole fractions. A proper scaling factor (depending on the oxide) is, therefore, implicitly incorporated into the equilibrium constant while using molar concentrations.

$$2\left[V_O^{\bullet\bullet}\right]+\left[h^{\bullet}\right] = \left[e^{/}\right] + 2\left[O_i^{//}\right], \tag{11}$$

we now have four equations and four unknowns. In order to find an analytical expression for the defect concentrations as functions of T and pO_2, we have to simplify the electroneutrality condition. These are known as Brouwer approximations, and result in our case in the following three approximations: 1) $2\left[V_O^{\bullet\bullet}\right]=\left[e^{/}\right]$, 2) $\left[V_O^{\bullet\bullet}\right] = \left[O_i^{//}\right]$, and 3) $\left[h^{\bullet}\right] = 2\left[O_i^{//}\right]$, valid in the low, intermediate and high pO_2 regimes. The pO_2 dependencies of the defects are now readily obtained by insertion of the relevant Brouwer approximation into the mass action laws, and are given in Fig. 2.2.

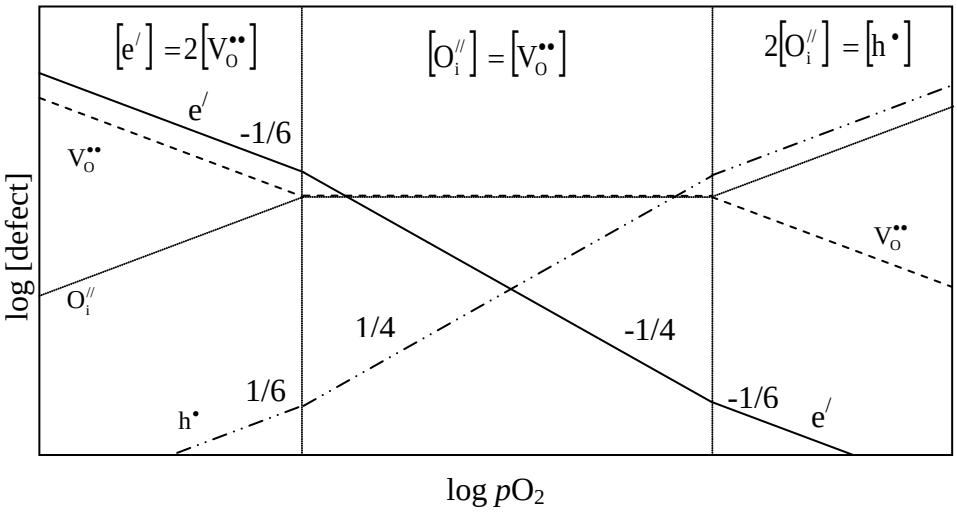

Fig. 2.2. Defect concentrations as function of oxygen partial pressure in an oxide dominated by Frenkel disorder. The Brouwer approximations are given within their valid pO_2 range. The slopes of the defect concentrations are also indicated. In the transition regions between two different Brouwer approximations, the simplifications (and their corresponding slopes) are no longer valid.

It is commonly encountered that one Brouwer approximation is valid for an oxide in a wide pO_2 and temperature range. In particular, for what is typically experimentally feasible[4], many ionic conductors exhibit only the intermediate pO_2 range behaviour where ionic defects dominate the electroneutrality condition.

Before we start off by calculating temperature dependencies for the defect concentrations, it is timely to introduce the concept of aliovalent doping, brought about by substitution of a regular lattice ion with an ion of different charge. The substitution may take place both on the anion and cation lattice, either on purpose or as an impurity. Usually, the mobility of the dopants is so low – at least compared to the charge carriers of the oxide – that the concentration of the dopant becomes fixed during the high temperatures of sample

[4] For conventional experiments, the upper limit for pO_2 is 1 atm. Low partial pressures of O_2 can be obtained by *e.g.* mixing known amounts of H_2O and H_2. pO_2 is then determined by the equilibrium constant for $H_2(g) + ½\ O_2(g) = H_2O(g)$.

preparation, and can be considered frozen-in at lower temperatures. If the dopant is effectively negatively charged (acceptor dopant), the concentrations of all positively charged defects, both in majority and minority, will increase, while the concentration of all negatively charged defects will decrease, and vice versa.

Let us now consider the same oxide as in Fig. 2.2. We assume that we are in the intermediate pO_2 range with the acceptor dopant concentration equal to C. At low C, internal defect equilibria rule the electroneutrality. When C approaches the intrinsic defect concentration level, the concentration of oxygen vacancies starts to increase, eventually increasing with the same slope as the acceptor dopant. For a set dopant level, the acceptors will be charge compensated by the oxygen vacancies at low temperatures, until the concentration of the interstitial oxide ions from the Frenkel disorder reaction reaches that level. At low temperatures, the concentration of electrons increases because reaction 5 is endothermic. In the high temperature region, the temperature dependence of the electronic defects becomes a function of both K_O and K_{AF}. For our choice of formation enthalpies ($\Delta_O H$ = 2/3 $\Delta_{AF}H^0$), this results in a reversed temperature dependency. The features are summarized in Fig. 2.3.

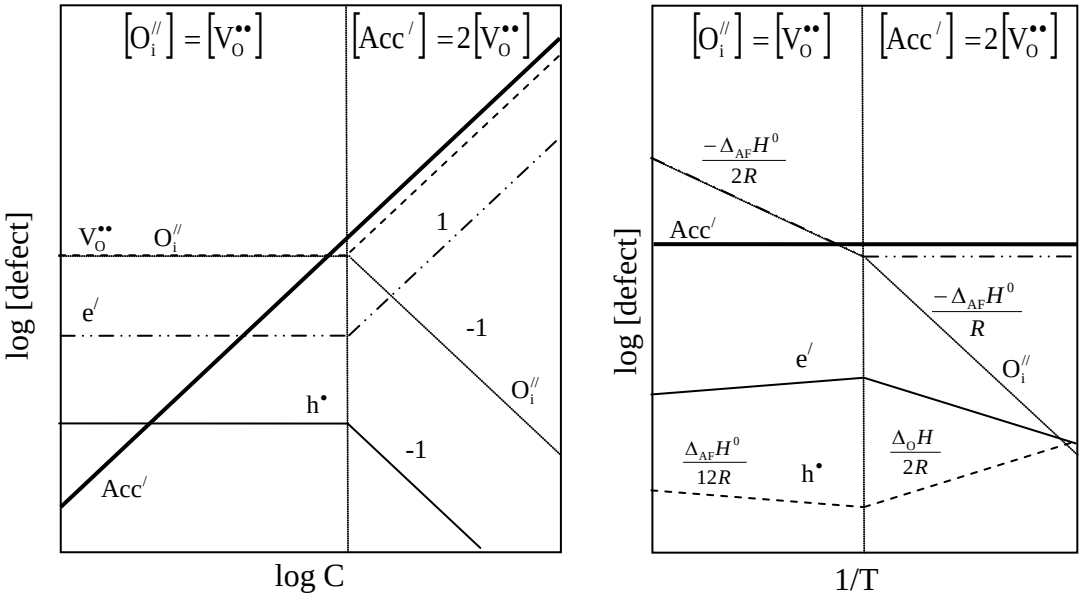

Fig. 2.3. Defect concentrations as a function of acceptor dopant concentration (left) and inverse temperature (right) for a Frenkel disordered oxide. In the temperature diagram, $\Delta_O H$ = 2/3 $\Delta_{AF}H$ was assumed. In the high temperature region the slope for the electron holes equals $\Delta_O H$/2R - $\Delta_{AF}H^0$/4R = $\Delta_{AF}H^0$/12R.

Several oxides may form hydrogen containing defects if they are exposed to a hydrogen containing atmosphere. In proton conducting oxides, the protonic defects reside on oxygen sites as hydroxide ions, (from now simply termed protons) and are formed when oxygen vacancies react with water vapour

$$H_2O(g) + V_O^{\bullet\bullet} + O_O^x = 2OH_O^{\bullet}, \qquad (12)$$

with corresponding mass action law

$$K_H = \frac{\frac{\left[OH_O^{\bullet}\right]^2}{[O]^2}}{\frac{\left[V_O^{\bullet\bullet}\right]}{[O]}\frac{\left[O_O^X\right]}{[O]}} pH_2O^{-1} = \exp\left(\frac{\Delta_H S^0}{R}\right)\exp\left(-\frac{\Delta_H H^0}{RT}\right). \quad (13)$$

For oxides that contain any significant amount of protons, $\Delta_H H^0$ is negative with reported values ranging between -200 and -20 kJ/mol (see *e.g.* Ref. 17). This implies that the concentration of protons increases towards lower temperatures. If the oxide is acceptor doped, the electroneutrality condition reads

$$\left[Acc'\right] = \left[OH_O^{\bullet}\right] + 2\left[V_O^{\bullet\bullet}\right]. \quad (14)$$

This defect structure has two simplifying cases; at low pH_2O and/or high temperatures the acceptors are fully compensated by oxygen vacancies and at high pH_2O and/or low temperatures the dopants are fully compensated by protons.

In the following, we will expand our treatment from the Brouwer approximations, that is, we will not simplify Eq. 14. By expressing the concentrations of the species in terms of mole fractions and by assuming that the concentrations of oxygen vacancies and protons remain small compared with that of oxygen sites ($\left[O_O^x\right] \approx [O]$), the mass action law reads

$$K_H = \frac{\left[OH_O^{\bullet}\right]^2}{\left[V_O^{\bullet\bullet}\right]\left[O_O^X\right]} pH_2O^{-1} \approx \frac{\left[OH_O^{\bullet}\right]^2}{\left[V_O^{\bullet\bullet}\right][O]} pH_2O^{-1}. \quad (15)$$

Combining this with the electroneutrality condition, the concentration of protons then reads

$$\left[OH_O^{\bullet\bullet}\right] = \frac{[O]K_H pH_2O\left(-1+\sqrt{1+\frac{8\left[Acc'\right]}{[O]\,K_H pH_2O}}\right)}{4}. \quad (16)$$

The concentration of the oxygen vacancies can now be obtained from the electroneutrality condition.

We will use $LaNbO_4$ [18,19] as our example oxide to study the defect structure of a high temperature proton conductor in more detail. For $LaNbO_4$, [O] = 4. The solid solubility of earth alkaline acceptors on the lanthanum site is about 1% [20], and the condition $\left[O_O^x\right] \approx [O]$ is therefore justified. In Fig. 2.4 we have used reported thermodynamic values for the hydration of $LaNbO_4$ [18] to plot the mole fractions of protons and oxygen vacancies as a function of pH_2O. The ratio of protons and acceptor dopants is also plotted for different acceptor dopant concentrations.

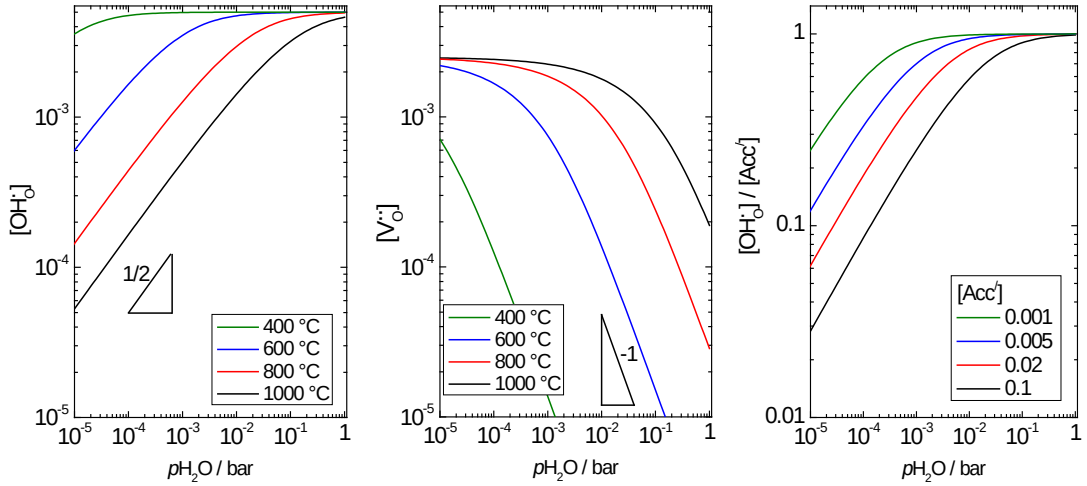

Fig. 2.4. Mole fractions of protons and oxygen vacancies as a function of water vapour pressure (left and middle) with [Acc$^{/}$] = 0.005. Ratio of the mole fractions of protons and acceptor dopants as a function of water vapour pressure at 600 °C (right). Enthalpy and entropy of hydration were set to -115 kJ mol^{-1} and -120 J mol^{-1} K^{-1}, respectively.

For this experimental window, the Brouwer approximation $\left[\mathrm{Acc}^{/}\right] = 2\left[\mathrm{V}_{\mathrm{O}}^{\bullet\bullet}\right]$ is reached at low $p\mathrm{H_2O}$ at 1000 °C. Then the concentration of protons is proportional to $p\mathrm{H_2O}^{1/2}$ (Fig. 2.4, left). $\left[\mathrm{Acc}^{/}\right] = \left[\mathrm{OH}_{\mathrm{O}}^{\bullet}\right]$ is met at high $p\mathrm{H_2O}$ at 400 and 600 °C. Then the concentration of oxygen vacancies is proportional to $p\mathrm{H_2O}^{-1}$ (Fig. 2.4, middle). In conventional experiments one may vary $p\mathrm{H_2O}$ within ~ 10^{-5} – 0.03 bar. Then, for this set of thermodynamic parameters and with [Acc$^{/}$] = 0.005, an experimental investigation under the extreme Brouwer approximations for a reasonable $p\mathrm{H_2O}$ interval will be difficult to carry out. This suggests that a rather large experimental window, both in terms of temperature and water vapour pressure, has to be investigated in order to enter both of the extreme Brouwer approximations during a material survey. To get a broader insight into the defect situation of a material it is beneficial to vary the dopant concentration. This is emphasised on the right hand side of Fig. 2.4, where it is seen that with increasing acceptor dopant concentration the ratio of protons and acceptors decreases, leading in turn to an increased importance of oxygen vacancies.

In summary, it has been showed how we may calculate equilibrium concentrations of defects as functions of control parameters (partial pressures, temperature and doping concentration) and thermodynamic parameters of the material.

2.2 Transport kinetics: electrical mobility of defects

The previous section described how to calculate equilibrium concentrations of defects. In this section the focus is shifted to how fast the defect concentrations change with time. Traditionally, in solid state chemistry this topic is described within the framework of Fick's

laws and in terms of diffusion coefficients. A full treatment of this topic is, however, outside the scope of this thesis, and we will rather describe transport kinetics in ionic oxides in terms of electrical mobility of defects.

2.2.1 Mobility of ionic defects

Ionic charge carriers migrate by activated diffusion. The diffusivity and the electrical mobility of an ionic charge carrier are linked through the Nernst-Einstein relation,

$$D_{\mathrm{i}} = u_{\mathrm{i}} \frac{RT}{z_{\mathrm{i}} F}. \tag{17}$$

Here, D_{i} and u_{i} denote the random diffusion coefficient and the electrical mobility of the defect i, respectively.

The mobility of an ionic defect is expressed according to an Arrhenius-type expression

$$u_{\mathrm{i}} = u_{0,\mathrm{i}} \frac{1}{T} \exp\left(-\frac{\Delta H_{\mathrm{mob,i}}}{\mathrm{R}T} \right) \tag{18}$$

where $u_{0,\mathrm{i}}$ and $\Delta H_{\mathrm{mob,i}}$ are the pre-exponential term and the activation enthalpy, respectively, of mobility of the defect i. The activation enthalpy of mobility can be interpreted as the energy barrier that the defect has to overcome to migrate from one site to the other. For ionic defects, large variations for ΔH_{mob} are encountered. Typically, ΔH_{mob} varies between 20 and 200 kJ mol^{-1} [16] (Sec. 6.2, p. 285) and selected data for different ionic defects are given in Table 2.1.

Table 2.1. Selected mobility data for different types of diffusion mechanisms. All perovskites are 10 % acceptor doped (per cation), otherwise else is stated.

Type of defect	Oxide	Crystal system	Structure type	Mobility parameters: $\Delta H_{mob,i}$ [kJ mol^{-1}]	Mobility parameters: u_0 [cm^2 K s^{-1} V^{-1}]	Mobility parameters: u_i at 500 °C [cm^2 V^{-1} s^{-1}]	Comments
Oxygen vacancy	δ-Bi_2O_3	Cubic	Fluorite-like	38-40			Refs. 4,21
	ZrO_2	Cubic	Fluorite	81	20	$1 \cdot 10^{-7}$	Ref. 22. Extracted from diffusivity curve
	CeO_2	Cubic	Fluorite	69	150	$4.6 \cdot 10^{-6}$	Ref. 23
	$SrTiO_3$	Cubic	Perovskite	83	10 000	$3.2 \cdot 10^{-5}$	Ref. 24. Less than 10^{20} cm^{-3} Fe^{3+}.
Proton	$BaZrO_3$	Cubic	Perovskite	41-42	28	$6 \cdot 10^{-5}$	Refs. 25,26
	$SrCeO_3$	Ortho-rhombic	Perovskite	61	90	$7 \cdot 10^{-6}$	Refs. 25,27
	$SrTiO_3$	Cubic	Perovskite	40	8	$2 \cdot 10^{-5}$	Ref. 25. 5% Sc-doped
	$LaPO_4$	Monoclinic	Monazite	77-82			Refs. 28,29
Electron or electron hole	Fe_2O_3	Hexagonal	Corundum	44^{**,h} 9.6^{**,h}	91 400^{h} 232^{e}	0.12^{h} 0.067^{e}	Ref. 30 h: $6 \cdot 10^{19}$ cm^{-3} Mg^{2+}. e: 1% Ti^{4+}.
	TiO_2		Rutile	~100^{**,h}		$7 \cdot 10^{-4}$ ^{h} 0.067^{***,e}	Ref. 31. Undoped
	$SrTiO_3$	Cubic	Perovskite			0.1^{*,h} 0.2^{*,e}	Ref. 24. Less than 10^{20} cm^{-3} Fe
	$SrTiO_3$	Cubic	Perovskite	96^{**,e,h}	30 000	$1 \cdot 10^{-5}$	Ref. 32. 20% Fe-doped
	$BaPrO_3$	Ortho-rhombic	Perovskite	30^{**,h}	150	0.0018	Ref. 33. 10% Gd-doped
	CeO_2	Cubic	Fluorite	39^{**,e}	400	0.0013	Ref. 34. Undoped

*Large polaron mechanism. **Small polaron mechanism. ***Band model. ^{e}Electrons. ^{h}Electron holes.

The pre-exponential term u_0 in Eq. 18 can be expanded into

$$u_0 = \Gamma_0 \alpha s^2 \frac{zF}{R} \exp\left(\frac{\Delta S_{mob}}{R}\right), \tag{19}$$

where Γ_0 is the attempt frequency, α is a structure dependent parameter, s is the average jump distance and ΔS_{mob} is the activation entropy of mobility. For ionic defects, Γ_0 is often found to be in the order of 10^{13} Hz, which is in the same order as the Debye frequency. For proton conductors, the O-H stretching frequency (typically ~ 10^{14} Hz) is a reasonable guess for Γ_0. The structure dependent parameter α is related to the number of possible jumps per site; thus it depends on the number of suitable nearest neighbours. This is again related to the type of diffusion mechanism[5]. In total, the variations within the factors in the pre-exponential term are rather small, causing rather small variations for u_0 within one type of diffusion

[5] Diffusion mechanisms are often classified as: the vacancy mechanism; the interstitial mechanism; and the interstitialcy mechanism. In high temperature oxidic proton conductors, protons diffuse via proton-hopping, the Grotthuss-mechanism (see e.g. Ref. 35)

mechanism and especially within a class of materials. Selected pre-exponential terms are given in Table 2.1.

2.2.2 Mobility of electronic defects

While ionic defects always migrate by activated diffusion (see Eq. 18), the picture is more complicated for electronic charge carriers. A full treatment of electrons and electron holes in solids is outside the scope of this thesis, and we will, therefore, treat this topic only superficially.

In pure non-polar semiconductors such as Si and Ge, electrons and electron holes move itinerantly in the conduction and valence band. The interaction with the thermal vibrations of the lattice results in electron and electron hole scattering. Since the thermal vibrations increases with increasing temperature, the mobility of electronic charge carriers decreases with increasing temperatures in pure non-polar semiconductors.

More important for us are the polar compounds. When electronic charge carriers migrate through polar compounds, they polarise their surroundings and thereby cause a local deformation of the crystal structure. The entity comprising both the electron (or electron hole) and the local deformation is termed a polaron. When the polarization effect is rather weak, and the deformation and associated energy are shallow and effectively spread over a considerable volume around the charge carrier, we deal with “large polarons”. For large polarons, the mobility is not greatly reduced as compared to those in non-polar semiconductors, and we may view the electron transport as taking place in bands. For large polarons, the mobility decreases with increasing temperature according to a power-law behaviour, $u \propto T^{-\mathrm{P}}$. For $SrTiO_3$, P is reported to 2.36 and 2.2 for electron holes and electrons, respectively [24].

When the polarization effect is stronger, the effective dimension of the polaron decreases as its associated energy well is deeper. When the polaron is smaller than the lattice parameter, we term it a small polaron and such electronic defects are better viewed as localised electrons (or holes). Now the transport takes place via an activated hopping process similar to that of the ionic defects. According to Maier, activation energies can be as high as 0.5 eV (or more) for small polarons [16] (Sec. 6.2.2, p 293). An interesting example exists in the case of rutile TiO_2. Here, electron holes migrate by an activated process while electrons migrate within the conduction band [31]. Selected mobility parameters for electron and electron holes are given in Table 2.1.

2.3 Effects of concentration and mobility on conductivity

The conductivity of a charge carrier i σ_i is the product of the charge, mobility and concentration of the charge carrier, $\sigma_i = z_i F u_i c_i$, and the total conductivity σ_{tot} is the sum of all partial conductivities. Let us now investigate how variations in both concentrations and mobilities of defects affect the total conductivity.

Let us consider a high temperature proton conductor where both protons and oxygen vacancies contribute to the total conductivity, *i.e.* $\sigma_{tot} = \sigma_H + \sigma_O$. As already shown in Fig. 2.4, the concentrations of protons and oxygen vacancies may change when subjected to a change in pH_2O. In order to reach equilibrium, ambipolar diffusion of oxygen vacancies and protons is required, and the slowest of the two charge carriers to a large extent determines the equilibrium rate [25]. A scenario where the oxide exhibits appreciable proton conductivity and long equilibrium times when subjected to changes in pH_2O (or vice versa) is therefore possible. If an oxide is rapidly cooled, the charge carrier concentrations can be fixed to the levels which were set, according to the thermodynamics, at higher temperatures. If that happens, we say that the concentrations are frozen-in.

In Fig. 2.5, we have plotted the partial and total conductivities at 400 °C under equilibrium conditions (left) and in the case of frozen-in charge carrier concentrations as determined from the given pH_2O at 600 °C (middle) and 900 °C (right). Again, we have used $LaNbO_4$ as our example material, for which mobility parameters for both protons and oxygen vacancies are given in Ref. 19.

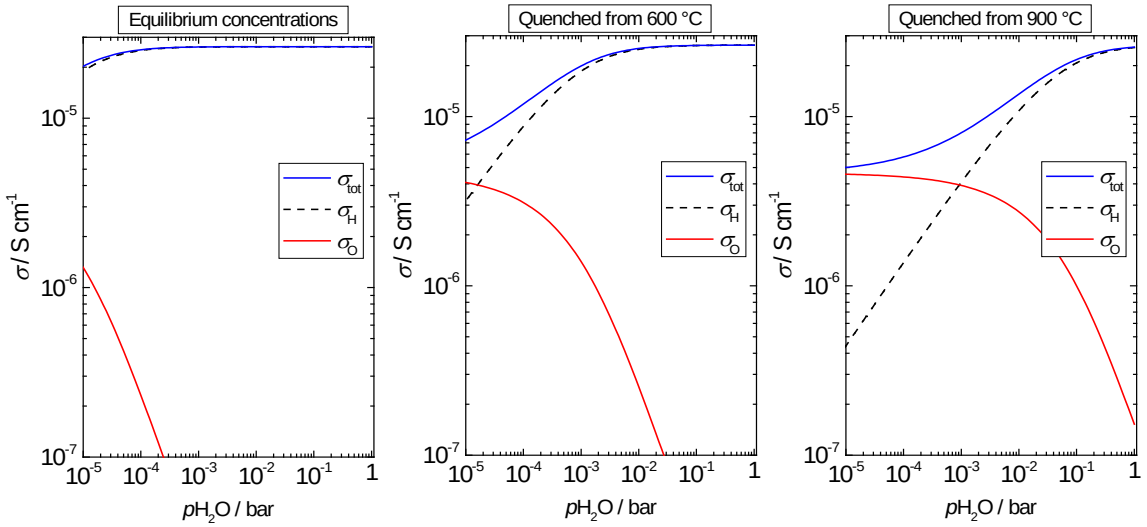

Fig. 2.5. Total and partial conductivities of protons and oxygen vacancies as a function of water vapour pressure at 400 °C. The concentrations of the charge carriers were calculated assuming equilibrium conditions at 400 °C (left), or frozen-in from 600 °C (middle) and 900 °C (right). Enthalpy and entropy of hydration were set to -115 kJ mol^{-1} and -120 J mol^{-1} K^{-1}, respectively and the mole fraction of acceptors was 0.005. For the mobility parameters, $u_{0,\mathrm{H}}$ = 35 cm^2 K V^{-1} s^{-1}, $\Delta H_{\mathrm{mob,H}}$ = 55 kJ mol^{-1}, $u_{0,\mathrm{O}}$ = 15 cm^2 K V^{-1} s^{-1}, and $\Delta H_{\mathrm{mob,O}}$ = 60 kJ mol^{-1} were used.

If equilibrium is reached at 400 °C, we see that σ_{tot} is essentially purely protonic within the displayed $p\mathrm{H_2O}$ range since the concentration of protons is essentially constant (*cf.* Fig. 2.4 (left)). On the other hand, if the oxide is quenched from a set $p\mathrm{H_2O}$ and temperature down to 400 °C, the proton concentration becomes lower than the equilibrium concentration. Correspondingly, the proton conductivity decreases and the oxide ion conductivity at 400 °C increases. The slope of log σ_{tot} vs. log $p\mathrm{H_2O}$ increases with increasing $p\mathrm{H_2O}$ before it levels off at high $p\mathrm{H_2O}$ when the oxide becomes a pure proton conductor. It is interesting to note that with this set of thermodynamic and mobility parameters, the total conductivity never becomes proportional to $p\mathrm{H_2O}^{1/2}$ at 400 °C, even under the Brouwer approximation $\left[\mathrm{Acc}^{/}\right] = 2\left[\mathrm{V_O^{\bullet\bullet}}\right]$ where the proton concentration is proportional to $p\mathrm{H_2O}^{1/2}$ (*cf.* Fig. 2.4). In our case, this is because the difference in the mobility of protons and oxide ions is rather small.

2.4 Defect associates

Until now, we have treated the defect equilibria using ideal mass action laws. This treatment only applies when the defects do not interact with each other, and, hence, are randomly distributed. In general, this is true for "low" defect concentration, but deviations from ideality have been found in numerous oxides. By way of example, the concentration of defects is so high in highly yttria-doped zirconia that oxygen vacancies interact with the acceptor dopants due to electrostatic attraction and elastic attractive forces (see *e.g.* Refs. 36

and 37). Thus, a more rigorous treatment is needed when dealing with higher defect concentrations.

In this section, we will treat the interaction between the defects by introducing a new defect species, a defect associate[6]. Let us consider a hydrated oxide in which the electroneutrality condition can be written as

$$\left[\mathrm{Acc}^{/}\right] = \left[\mathrm{OH}_{\mathrm{O}}^{\bullet}\right] . \tag{20}$$

Due to attractive forces those defects will interact, and the associating reaction can be written

$$\mathrm{Acc}^{/} + \mathrm{OH}_{\mathrm{O}}^{\bullet} = \left(\mathrm{AccOH}_{\mathrm{O}}\right)^{\mathrm{X}}, \tag{21}$$

with corresponding mass action law (assuming that the associate resides on the oxygen site)

$$\mathrm{K}_{\mathrm{as}} = \frac{\dfrac{\left[\left(\mathrm{AccOH}_{\mathrm{O}}\right)^{\mathrm{X}}\right]}{[\mathrm{O}]}}{\dfrac{\left[\mathrm{Acc}^{/}\right]}{[\mathrm{M}]}\dfrac{\left[\mathrm{OH}_{\mathrm{O}}^{\bullet}\right]}{[\mathrm{O}]}} = \exp\left(-\frac{\Delta_{\mathrm{as}}G^{0}}{RT}\right) = \exp\left(-\frac{\Delta_{\mathrm{as}}H^{0}}{RT}\right)\exp\left(\frac{\Delta_{\mathrm{as}}S^{0}}{R}\right). \tag{22}$$

Here M denotes the host metal cation being replaced by the acceptor, so that [M] denotes the concentration of such metal cation sites. We have furthermore expressed the activity of associates by assuming that they can be taken to be distributed over all available oxygen sites. The trapping of the protons according to Reaction 21 reduces the concentrations of free protons according to

$$\left[\mathrm{OH}_{\mathrm{O}}^{\bullet}\right] = \mathrm{C} - \left[\left(\mathrm{AccOH}_{\mathrm{O}}\right)^{\mathrm{X}}\right] \tag{23}$$

where C denotes the nominal dopant concentration. An analytical expression of the concentration of protons can be found by simultaneously solving Eq. 20, 22 and 23. Because association reactions are generally exothermic, the associate will gradually dissociate with increasing temperature. In Fig. 2.6 the concentration of free protons as a function of inverse temperature is shown for a set of thermodynamic parameters.

[6] An alternative approach is to replace the concentration term in the expression for the chemical potential by activity, *i.e.* $\mu_{\mathrm{d}} = \mu_{\mathrm{d}}^{0} + RT\ln a_{\mathrm{d}} = \mu_{\mathrm{d}}^{0} + RT\ln c_{\mathrm{d}} + RT\ln f_{\mathrm{d}}$, and find an expression for f_{d} as a function of c_{d}.

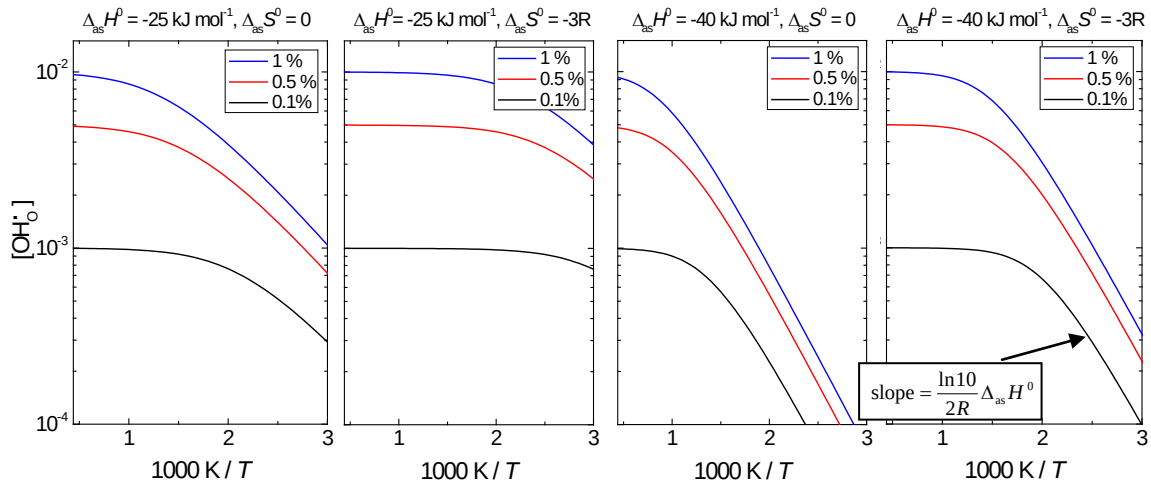

Fig. 2.6. The concentration of protons as a function of inverse temperature for a set of enthalpies and entropies of association. The nominal dopant concentration is also varied, and is given in mole fraction. It is assumed that the number of possible sites of the associate is equal to the number of oxide sites.

From the association reaction a negative $\Delta_{as}S^0$ is expected since the defect associate represents a more ordered state than the acceptor and proton alone. This helps to stabilize the free protons. It is also seen that for low defect concentrations, the concentration of free protons is equal to the nominal dopant concentration down to lower temperatures than compared to high C. When most of the protons are associated (at low T and/or $\Delta_{as}G^0$ highly negative), $C = \left[\left(AccOH_O\right)^X\right]$. From the electroneutrality condition (Eq. 20) and the equilibrium constant (Eq. 22) it follows

$$\left[OH_O^\bullet\right] = \left(\frac{C}{K_{as}}\right)^{1/2} \propto \exp\left(-\frac{\Delta_{as}H^0}{RT}\right)^{-1/2} . \qquad (24)$$

Thus, when the logarithm of the concentration of free protons is plotted as a function of 1/T, the slope is proportional to ½$\Delta_{as}H^0$.

Since the interaction between the dopant and the charge carrier is, in addition to electrostatic forces, a result of elastic forces, we expect $\Delta_{as}H^0$ to vary with the type of dopant. Indeed, this has been found experimentally. For example, in 1 % RE_2O_3-doped CeO_2 $\Delta_{as}H^0$ has been reported between 12 (Gd-doped) and 65 kJ mol^{-1} (Sc-doped) [38]. In YSZ, 25 kJ mol^{-1} have been reported [22].

Fig. 2.7 shows the proton conductivity when protons are trapped due to association for a set of physico-chemical parameters.

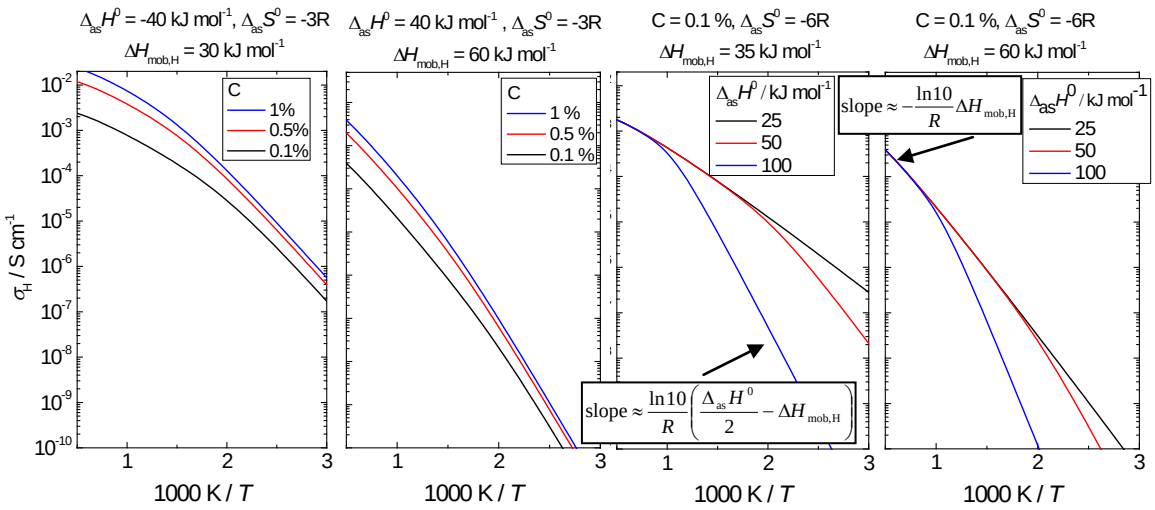

Fig. 2.7. The effect of trapping of protons on the proton conductivity as a function of inverse temperature. Parameters varied according to figure legends. The pre-exponential term of mobility of protons was set to 10 cm^2 K V^{-1} s^{-1} and molar density of the oxide proton conductor to 0.03 mol cm^{-3}. The approximate slopes of the curves in the high and low temperature regions are given.

The figures allow for some comments. Firstly, the effect of the association can be deteriorating on the conductivity; a decrease in conductivity by orders of magnitude is possible. Secondly, the transition from high to low temperature, *i.e.* going from a completely dissociated state to a situation where the concentration of protons is determined by the association thermodynamics (Eq. 24), is rather smooth as it takes place over a rather large temperature range. The larger the difference between $|½\Delta_{as}H^0|$ and $\Delta H_{mob,H}$, the sharper the bend of the transition. Thirdly, when the concentration of protons is determined by the association thermodynamics (Eq. 24), the slope in the conductivity curve is proportional to $|½\Delta_{as}H^0| + \Delta H_{mob,H}$, whereas at high temperatures it is proportional to $\Delta H_{mob,H}$.

For high temperature proton conductors, the concentration of protons decreases with increasing temperature due to the negative hydration enthalpy (Eq. 13). Formation of defect associates at low temperatures may counteract the expected increase in protonic charge carriers at low temperatures, which can complicate the interpretation of proton conductivity data.

3. Interfaces and transport in ionic solids

Moving away from the perfect world represented by single crystals, we can now introduce a new degree of freedom, namely interfaces. Interfaces break the symmetry of the single crystal and this, as we will see in the following sections, may largely impact on the overall transport of charged species.

3.1 Interfaces: definitions and introductory comments

Ceramics contain a wide range of interfaces, which can be classified as internal (*e.g.* domain boundaries, grain boundaries and phase boundaries) or external (*e.g.* solid-gas and solid-liquid).[7] Furthermore, it is useful to classify the effect that an interface exerts on the transport as either extrinsic or intrinsic. By extrinsic we refer to the role that an inert impurity phase (or air gap) plays on the overall transport by reducing the area that the current can pass. This issue is covered in Section 3.2. The intrinsic term covers those effects that inherently are found in the ceramic of interest, *e.g.* the inherently high grain boundary resistivity due to depletion of charge carriers in the vicinity of the grain boundary. Finally, we differentiate between transport across and along interfaces.

At all interfaces there normally exists a charged zone where local electroneutrality is not fulfilled. The charged zone consists of an interfacial core with adjacent space-charge layers that compensate the charge of the core. The interfacial core has a different structure than the bulk crystal, and its spatial extent is typically in the order of a few unit cells. Because of the structural differences, mobilities may be altered in this narrow core. This topic is briefly touched upon in Section 3.4.

In the space-charge layers, which structurally are part of the bulk material, mobilities are generally the same as in bulk. However, the charge carrier concentrations can be very different from bulk. The space-charge concept is introduced in Section 3.3, and in this section we focus on the effect that a decreased charge carrier concentrations in the grain boundaries have on the transport across interfaces. Also increased charge carrier concentrations may be encountered in the space-charge layers, leading to increased transport along interfaces. This topic is briefly covered in Section 3.4. Finally, in a polycrystalline material, different charge carriers may prevail in grain interior and in the grain boundaries. This may give rise to chemical polarization, which is covered in Section 3.5.

---

[7] The interface between a grain and a pore (air gap) *inside* a solid material is in this context considered as an internal interface.

3.2 Transport across grain boundaries: extrinsic effects

In our treatment of the various effects of interfaces on ionic transport, we firstly discuss how an inert secondary phase influence on the transport properties of a ceramic. Since such effects do not originate from the host material itself, we term them as extrinsic effects. Consider an ionically conducting polycrystalline sample with micrometer-sized grains and an appreciable amount of either an insulating phase or air gaps residing in the grain boundaries, as depicted in Fig. 3.1. As is seen from the figure, the ionic current passing the grain boundary has two parallel pathways, one through the insulating phase (or the air gap) (i) and one through the direct grain-to-grain contact (ii). Only when the coverage of the insulating phase at the grain boundaries is very high, the ratio of the current passing through the insulating phase becomes high enough so that the electrical properties of the grain boundaries are influenced by the nature of the insulating phase[8]. For most practical examples, however, the insulating secondary phase simply restricts the current through the grain boundaries by reducing the area of direct grain-to-grain contacts, thereby increasing the grain boundary resistance.

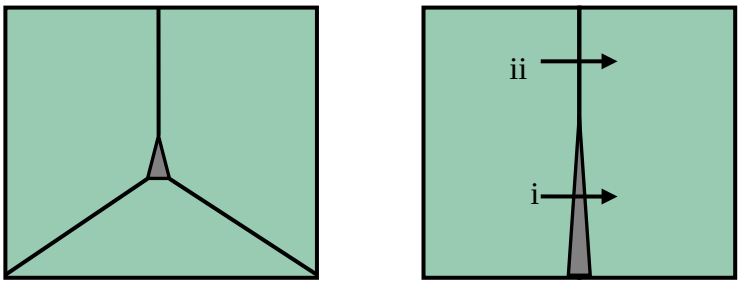

Fig. 3.1. Right: Schematic of a typical morphology of a polycrystalline sample with an insulating intergranular phase, marked as grey, situated at a triple grain junction. An air gap (pore) will act in the same way as an insulating phase. Left: Close-up focusing on one grain boundary next to the triple grain junction. The current has two parallel pathways: i) through the insulating phase or ii) through the direct grain-to-grain contact.

In order to investigate how a reduced direct grain-to-grain contact area influence on the impedance of a polycrystalline sample, Fleig and Maier [39] carried out three-dimensional finite-element calculations on simple model systems with circular grain-to-grain contacts. Fig. 3.2 shows how the resistance resulting from the current constriction caused by the insulating phase, R_{gb}^{cc}, vary with the fraction of contact area for four different numbers of contacts. It is seen that when the fraction of contacted area equals 1% and when the current only can pass one contact point, R_{gb}^{cc} is ~ 8 times higher than the grain interior resistance, R_{gi}. The model predicts a fraction of contacted area less than 0.01% before R_{gb}^{cc} is more than

[8] This also depends on the ratio of the conductivities of the ionic conductor and the “insulating” phase.

100 times larger than R_{gi}. We also note that as the number of contact points increase, R_{gb}^{cc} decreases.

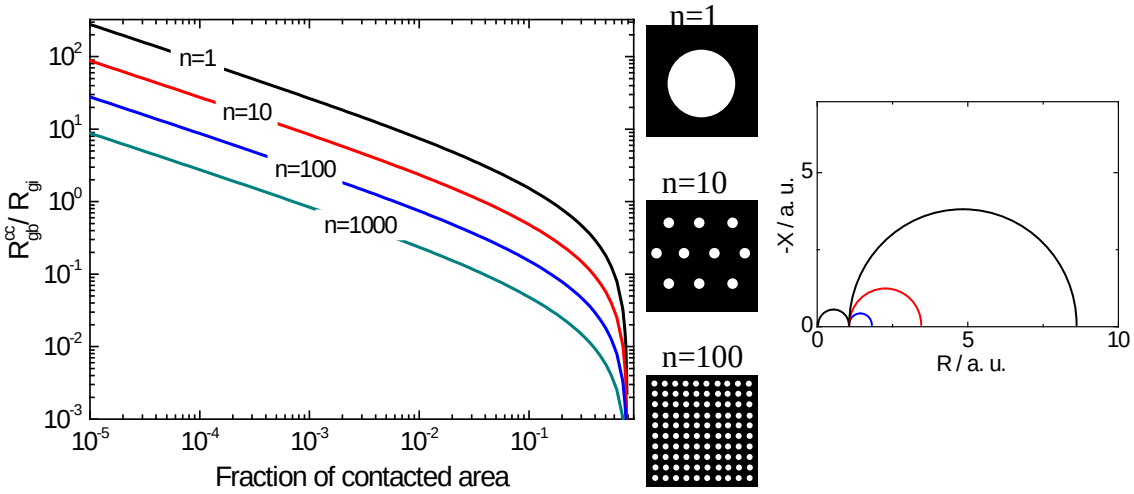

Fig. 3.2 Left: The different lines show the calculations of the ratio of the resistance caused by current constriction and the grain interior resistance as of fraction of contacted area for different numbers of contact points. The geometry of the contact points is indicated. Right: Impedance spectra for a fraction of contacted area = 1%. The colours of the low frequency arcs caused by the constriction of the current lines correspond to the number of contact points given at left.

In a Nyquist plot, R_{gb}^{cc} is seen as an arc at lower frequencies than the grain interior arc. R_{gb}^{cc} does not, however, represent a process with a different relaxation time than the grain interior process, it is rather a result of the constriction of current lines in three dimensions because of the reduced grain-to-grain contact area. R_{gb}^{cc} and R_{gi} will exhibit the same temperature and partial pressures dependencies, given that the interfacial geometry does not change [39]. These characteristics are useful to bear in mind when elucidating possible reasons of an observed "grain boundary resistance".

Insulating phases often exist as pockets at triple grain junctions while the grain boundaries otherwise remain "clean". This morphology is depicted in Fig. 3.1, and has been observed in acceptor doped ZrO_2 and CeO_2 (see *e.g.* Refs. 40 and 41 and references therein). Typically, these phases consist of SiO_2, Al_2O_3 and cations from the ceramic itself, and they therefore exist as a siliceous phase. These intergranular siliceous phases are, in general, "very dynamic in nature" (Ref. 40, page 163), implying that the wetting properties of the siliceous phase change with ceramic, type and amount of impurities and process parameters such as sintering temperature, additional heat treatment and heating/cooling rates. Consequently, the fraction of contacted area is strongly linked to those parameters. For example, by heat treating acceptor doped ZrO_2 containing a significant amount of siliceous phases, Jung and co-workers showed that the grain boundary resistance decreased by a factor of ~7 [42]. This

could be explained by decreased current constriction at the grain boundaries because the intergranular phase dewetted during the heat treatment.

Although the magnitude of the grain boundary resistance in zirconia and ceria is reported to vary as a function of process parameters, the activation energy of the grain boundary conductivity is reported within a fairly shallow window, a strong indication of that the current does not pass through the insulating phase [40].

As pointed out in Section 3.1, a high grain boundary resistance can also be caused by intrinsic effects. In Section 3.3.3 we consider under what conditions we can expect that the intrinsic effects become more important than the extrinsic.

3.3 Transport across grain boundaries: intrinsic effects

It is recognized that ionic and electronic transport across grain boundaries in ceramics can be severely opposed by an intrinsic grain boundary resistance. This inherent low grain boundary conductivity has been studied in various high-purity materials, *e.g.* ZrO_2 [7,8], CeO_2 [9,10], $LaGaO_3$ [11,43] and $SrTiO_3$ [44,45] (all acceptor doped). For these oxides, the inherent low grain boundary conductivity originates from depletion of positive charge carriers in the vicinity of the positively charged grain boundary core.

In the following treatment we will describe the grain boundary core-space-charge layer model in detail. Firstly, we sketch a thermodynamic framework that describes the formation of space-charge layers. Then we examine defect concentration profiles in the space-charge layers using a more phenomenological approach.

3.3.1 The grain boundary core-space-charge layer model

The description of the grain boundary core-space-charge layer model follows the approach recently given by De Souza [46]. In electrical terms, a grain boundary consists of a grain boundary core, which is structurally different from bulk, and two adjacent space-charge layers, *cf.* Fig. 3.3. The intercept between the grain boundary core and the space-charge layer is positioned at $x = 0$ and the extent of one space-charge layer is given by the space-charge layer width, λ^*. The width of the grain boundary core w_c is assumed to be small compared to the width of the space-charge layers, which in turn is small compared to the size of the crystal. The transport and thermodynamic parameters change abruptly, like a step function, when going from the bulk crystal to the core.

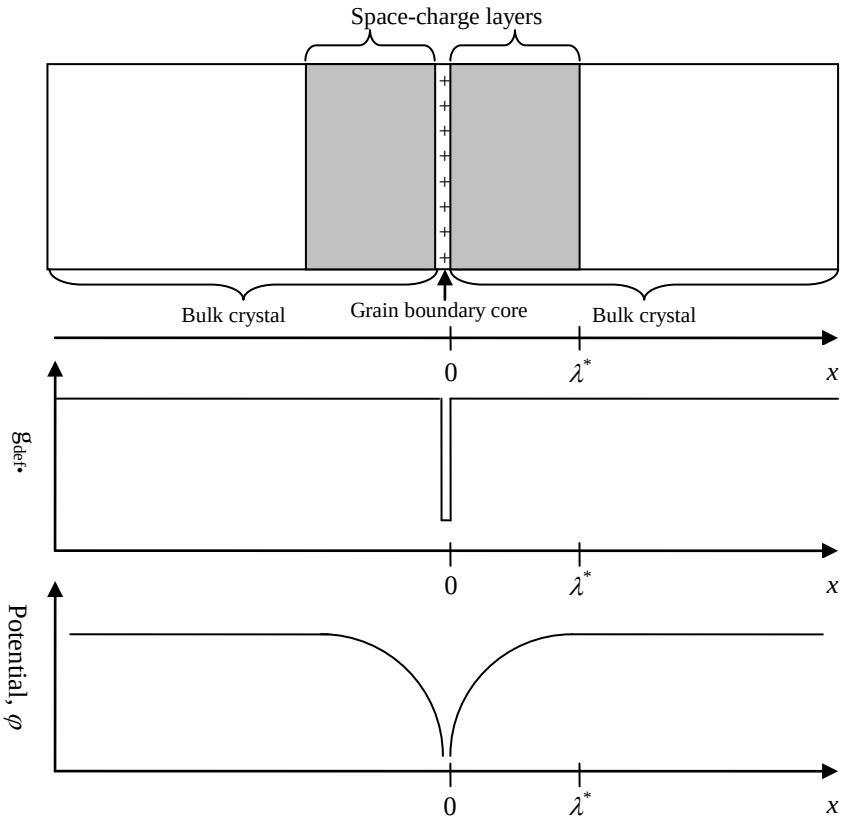

Fig. 3.3. Upper: Schematic grain boundary consisting of a positive core charge compensated by two adjacent space-charge layers. Middle: Step-like variation in the Gibbs formation energy of one positively charged defect being responsible for the positively charged core. Lower: The electrical potential profile.

Outside the space-charge layers, local electroneutrality prevails, and by definition, here $x = \infty$. The two space-charge layers are, in structural terms, part of the bulk crystal and it is therefore reasonable to assume that the mobilities of the charge carriers residing here are equal to what we find outside the space-charge layers[9]. The electroneutral part of the bulk crystal is termed grain interior.

In principle, the core can be positively or negatively charged. We will, however, continue our treatment assuming that the core is positively charged and, furthermore, that oxygen vacancies are solely responsible for this charge. Then, for sake of overall electroneutrality, the positively charged core has to be balanced, and this is accomplished by an opposite charge smeared out in the adjacent space-charge layers. Consequently, a non-uniform electrical potential φ in the space-charge layers develops. The potential at $x = 0$ referenced to the potential in grain interior ($x = \infty$) is termed the space -charge potential $\Delta\varphi(0)$, and increases with the number of oxygen vacancies being transferred to the core. The higher the $\Delta\varphi(0)$, the more severe the depletion of positive charge carriers (*e.g.* oxygen vacancies) in

[9] We neglect possible effects of electrical fields and strains.

the space-charge layers. Thus, $\Delta\varphi(0)$ phenomenologically scales with the grain boundary resistance.

The total Gibbs energy of redistribution of oxygen vacancies from grain interior to the grain boundary core can be expressed in terms of individual contributions as [46]

$$\Delta_{sc}G = \Delta_{dr}G + \Delta_{cfg}G + \Delta_{el}G \,. \tag{25}$$

Here, $\Delta_{dr}G$ is the Gibbs energy change in redistributing oxygen vacancies from grain interior to the core, $\Delta_{cfg}G$ reflects the loss in configurational entropy due to the confinement of oxygen vacancies in the grain boundary core as compared to the spacious environment in grain interior, and $\Delta_{el}G$ is the electrostatic energy expended in the redistribution of the charged oxygen vacancies. An equilibrium space-charge layer has been formed when $\Delta_{sc}G$ is at a minimum as a function of the number of oxygen vacancies that are transferred from grain interior to core.

$\Delta_{sc}G$ is a rather complex function and we will in the following briefly mention some of the important parameters contributing to the three individual contributions of $\Delta_{sc}G$. $\Delta_{dr}G$ is proportional to the Gibbs energy change in redistributing one oxygen vacancy from grain interior to the core, $\Delta g_{V_O^{\bullet\bullet}}$, and the number of oxygen vacancies being transferred from grain interior to core. (This assumes that $\Delta g_{V_O^{\bullet\bullet}}$ is independent of the number of transferred oxygen vacancies.)

$\Delta_{cfg}G$ reflects the loss in configurational entropy of redistributing oxygen vacancies from grain interior to core. Thus, the fewer possible sites for oxygen vacancies in the core, the higher $\Delta_{cfg}G$. The number of possible core sites is in turn related to the density of core sites N_c and the grain boundary core width w_c.

Upon redistributing the oxygen vacancies, the space-charge potential increases. The net charge density in the space-charge layers, therefore, increases and the redistribution becomes progressively more energy-demanding due to the electrostatic interactions. Thus, the slope of $\Delta_{el}G$ as a function of the number of transferred oxygen vacancies increases gradually as the space-charge potential increases.

Consider a grain interior defect scenario where the acceptor is charge compensated by one singly and one doubly charged positive defect with equal concentrations. Possible positive defects are a hydroxide ion residing on an oxygen site and an oxygen vacancy. If Δg for the two positive defects are equal ($\Delta g_{V_O^{\bullet\bullet}} = \Delta g_{OH_O^{\bullet}}$) and they can settle on the same core sites,

the concentration of the singly charged defect in the core will be higher because a defect with double charge will have a higher $\Delta_{el}G$ than a singly charged defect.

The variation in $\Delta_{sc}G$ and its three components are plotted as a function of the number of transferred oxygen vacancies in Fig. 3.4.

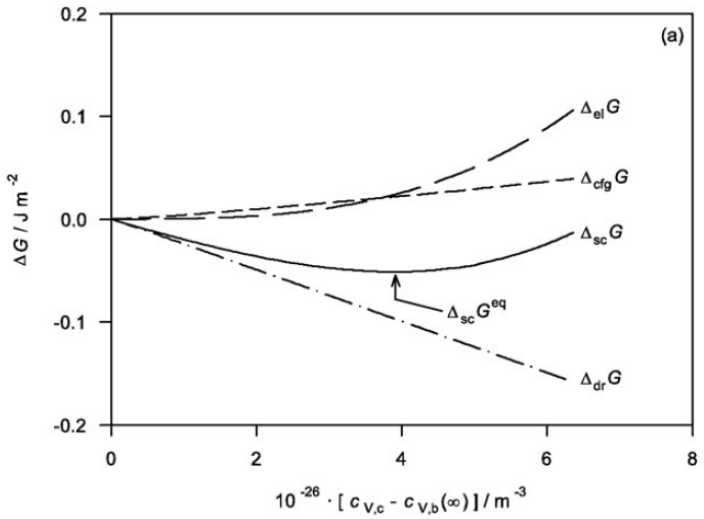

Fig. 3.4. Typical variation in the individual contributions ($\Delta_{dr}G$, $\Delta_{cfg}G$, and $\Delta_{el}G$, dotted lines) to the total Gibbs energy of redistribution of oxygen vacancies from grain interior to the grain boundary core ($\Delta_{sc}G$, unbroken line) as a function of transferred oxygen vacancies, as shown by De Souza in Ref. 46. For details of the calculations, the reader is referred to Ref. 46.

$\Delta\varphi(x)$ is defined as the electric potential at position x in the space-charge layer referenced to the potential in grain interior. From Poisson's equation we have

$$\frac{\mathrm{d}^2\Delta\varphi(x)}{\mathrm{d}x^2} = -\frac{1}{\varepsilon}Q(x), \tag{26}$$

where ε is the dielectric permittivity and $Q(x)$ the net charge density in the space-charge layer at position x. If we assume a defect scenario where oxygen vacancies are charge compensated by acceptors ($Acc^{/}$), we obtain

$$Q(x) = e\left[2c_{V_O^{\bullet\bullet}}(x) - c_{Acc^{/}}(x)\right] \tag{27}$$

where c denotes volume concentration. Assuming that the acceptors are immobile, and hence their concentration is constant, leads to

$$Q(x) = e\left[2c_{V_O^{\bullet\bullet}}(x) - c_{Acc^{/}}(\infty)\right] = e\left[2c_{V_O^{\bullet\bullet}}(x) - 2\,c_{V_O^{\bullet\bullet}}(\infty)\right] \quad . \tag{28}$$

The important factor governing the oxygen vacancy concentration profile in the space-charge layer is the electrochemical potential through the grain boundary and grain interior. The

electrochemical potential of a mobile oxygen vacancy as a function of distance *x*, is ideally (assuming unity activity coefficient) given by

$$\eta_{V_O^{\bullet\bullet}}(x) = \mu^0_{V_O^{\bullet\bullet}} + k_B T \ln \frac{c_{V_O^{\bullet\bullet}}(x)}{N_{V_O^{\bullet\bullet}} - c_{V_O^{\bullet\bullet}}(x)} + 2e\varphi(x) \approx \mu^0_{V_O^{\bullet\bullet}} + k_B T \ln \frac{c_{V_O^{\bullet\bullet}}(x)}{N_{V_O^{\bullet\bullet}}} + 2e\varphi(x) \qquad (29)$$

where $\mu^0_{V_O^{\bullet\bullet}}$ is the standard chemical potential of oxygen vacancies, $N_{V_O^{\bullet\bullet}}$ is the density of oxygen sites, and *e*, k_B and *T* have their usual meanings. The expression on the right hand side is valid for small $c_{V_O^{\bullet\bullet}}(x)$. At equilibrium, where $\eta_{V_O^{\bullet\bullet}}(x) = \eta_{V_O^{\bullet\bullet}}(\infty)$, the electric potential relative to grain interior, $\Delta\varphi(x) = \varphi(x) - \varphi(\infty)$, is then

$$\Delta\varphi(x) = \frac{k_B T}{2e} \ln \frac{c_{V_O^{\bullet\bullet}}(\infty)}{c_{V_O^{\bullet\bullet}}(x)} \qquad (30)$$

and, consequently,

$$c_{V_O^{\bullet\bullet}}(x) = c_{V_O^{\bullet\bullet}}(\infty) \exp\left(-\frac{2e\Delta\varphi(x)}{k_B T}\right). \qquad (31)$$

The charge density $Q(x)$ then reads

$$Q(x) = 2e c_{V_O^{\bullet\bullet}}(\infty) \left[\exp\left(-\frac{2e\Delta\varphi(x)}{k_B T}\right) - 1\right]. \qquad (32)$$

For this charge density, Poisson's equation has to be solved numerically (an analytical solution does not exist). In order to do this, De Souza employed an iterative procedure where the Poisson equation was solved numerically to obtain a value for $\Delta\varphi(0)$. Then, the grain boundary core charge Q_c (per unit area) was calculated by means of two different approaches. Firstly, by applying Gauss' law which relates electric field and electric charge, where the obtained value for $\Delta\varphi(0)$ was used to calculate one value for Q_c. Secondly, with the same value of $\Delta\varphi(0)$, Q_c was calculated through an expression of the core charge in terms of the core width, space charge potential, the Gibbs energy change in redistributing one oxygen vacancy, and densities of sites and defects (Ref. 46, Eq. 21)

$$Q_c = 2e w_c c_{V_O^{\bullet\bullet}}(\infty) \left[\frac{N_c \exp\left(-\frac{\Delta g_{V_O^{\bullet\bullet}} + 2e\Delta\varphi(0)}{k_B T}\right)}{N_{gi} + c_{V_O^{\bullet\bullet}}(\infty) \exp\left(-\frac{\Delta g_{V_O^{\bullet\bullet}} + 2e\Delta\varphi(0)}{k_B T}\right)} - 1\right]. \qquad (33)$$

$\Delta\varphi(0)$ was varied until the difference between the two calculated values of Q_c was within the required accuracy. In Fig. 3.5 the space-charge potential is plotted as a function of $\Delta g_{V_O^{\bullet\bullet}}$. It is seen that $\Delta\varphi(0)$ increases with increasing $|\Delta g_{V_O^{\bullet\bullet}}|$ until a plateau is reached. When $|\Delta g_{V_O^{\bullet\bullet}}|$ is sufficiently large, all available sites in the core are occupied by oxygen vacancies and Q_c reaches its maximum for that particular N_c.

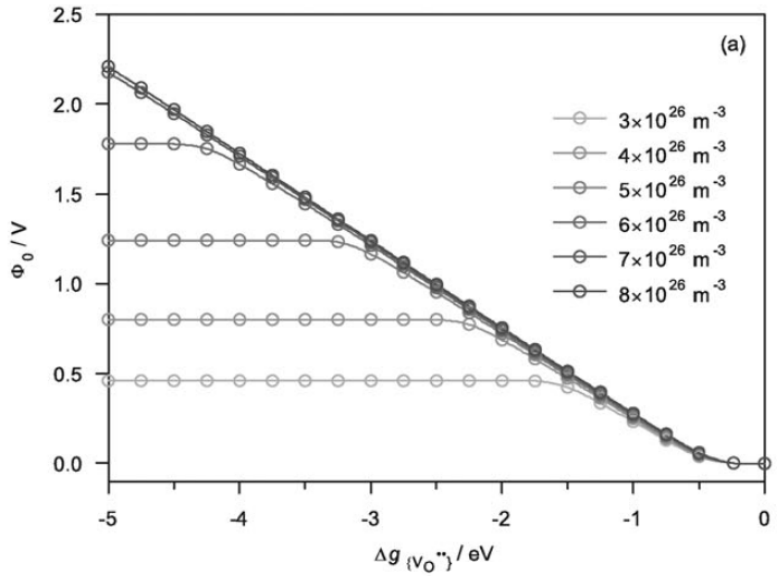

Fig. 3.5. The space-charge potential as a function of the Gibbs energy change in redistributing one oxygen vacancy from grain interior to the core, $\Delta g_{V_O^{\bullet\bullet}}$, for different densities of grain boundary core sites N_c at 600 K for w_c = 7.8 Å with $c_{V_O^{\bullet\bullet}}(\infty) = 3.5 \cdot 10^{24}$ m^{-3} and dielectric constant ε_r = 160, as shown by De Souza in Ref. 46.

An approximate analytical solution to Poisson's equation with the charge density in Eq. 32 exists, and is derived in the following. We assume that the oxygen vacancies are so strongly depleted in the space-charge layers (as a result of the positively charged core) that $Q(x)$ can be considered to be governed only by the acceptor-dopant concentration. This is often referred to as the depletion approximation, and $Q(x)$ then reads

$$Q(x) = e\left[2c_{V_O^{\bullet\bullet}}(x) - c_{Acc'}(x)\right] \approx -e\,c_{Acc'}(x). \tag{34}$$

We now apply the Mott-Schottky approximation, which assumes that the acceptor concentration is constant up to the grain boundary core. The charge density in the space charge layer is then simply given by the concentration of acceptors in the grain interior:

$$Q(x) = ec_{Acc'}(x) = ec_{Acc'}(\infty) \tag{35}$$

The Poisson equation now reads

$$\frac{\mathrm{d}^2\Delta\varphi(x)}{\mathrm{d}x^2} = -\frac{e}{\varepsilon}c_{Acc'}(x). \tag{36}$$

The appropriate boundary conditions for solving Eq. 36 are i) $\Delta\varphi(0)$ = constant and ii) $\Delta\varphi(\lambda^*) = 0$. The analytical solution of Eq. 36 then reads

$$\Delta\varphi(x) = \begin{cases} \dfrac{ec_{\mathrm{Acc}'}(\infty)}{2\varepsilon}\left(x-\lambda^*\right)^2 & : 0 \le x \le \lambda^* \\ 0 & : x > \lambda^* \end{cases} . \tag{37}$$

The space-charge potential, $\Delta\varphi(0)$ is readily obtained from Eq. 37, and equals $\dfrac{ec_{\mathrm{Acc}'}(\infty)}{2\varepsilon}(\lambda^*)^2$.

L_D is the Debye length and is here given by

$$L_\mathrm{D} = \left(\frac{k_\mathrm{B}T\varepsilon}{2e^2c_{\mathrm{Acc}'}(\infty)}\right)^{\frac{1}{2}} . \tag{38}$$

By combining those two expressions, we obtain the following expression for the space charge layer width

$$\lambda^* = 2L_\mathrm{D}\left(\frac{e\Delta\varphi(0)}{k_\mathrm{B}T}\right)^{1/2} . \tag{39}$$

Thus, λ^* scales with ε and $\Delta\varphi(0)$. We also see that λ^* is proportional to $\left(c_{acc'}\right)^{-1/2}$. As a practical implication, the largest effects from space-charge layers are expected for materials with low dopant concentrations and high dielectric permittivities.

An approximate value for the grain boundary charge per unit area, $Q_{\mathrm{c,approx}}$ is obtained by multiplying the grain boundary charge density $Q(x)$ (Eq. 35, which is constant due to the depletion approximation) by two space-charge layer widths (Eq. 39)

$$Q_{\mathrm{c,approx}} = |Q| \times 2\lambda^* = ec_{\mathrm{Acc}'}(\infty) \times 2\left(\frac{2\varepsilon\Delta\varphi(0)}{ec_{\mathrm{Acc}'}(\infty)}\right)^{1/2} = \left(8ec_{\mathrm{Acc}'}(\infty)\varepsilon\Delta\varphi(0)\right)^{1/2} \tag{40}$$

The Mott-Schottky approximation is commonly used in the literature (see *e.g.* Ref. 40). In the following we will briefly address the inaccuracy caused by the depletion approximation. In order to do this, we will take advantage of the equations and pertaining calculations elaborated above for the case of immobile acceptor-dopants and mobile oxygen vacancies. The maximum values for Q_c, *i.e.* when all oxygen core sites are filled with oxygen vacancies, are calculated from Eq. 33 and are given along with the corresponding accurate space-charge potentials, for some values of N_c in Table 3.1. The approximate value for the space-charge potential as calculated through Eq. 40 is also given.

Table 3.1. Calculated maximum values for the grain boundary charge for different densities of grain boundary core sites for oxygen vacancies at T = 600 K for w_c = 7.81 Å, $c_{V_O^{\bullet\bullet}}(\infty) = 3.5 \cdot 10^{24}$ m^{-3}, $N_{gi} = 5.0 \cdot 10^{28}$ m^{-3}. The corresponding accurate space-charge potential is given and compared with the approximate space-charge potential where the maximum grain boundary charge and ε_r = 160 were used as input parameters.

N_c [m^{-3}]	Maximum Q_c [a] [C m^{-2}]	Accurate $\Delta\varphi(0)$ [b] [V]	Approximate $\Delta\varphi(0)$ [c] [V]
$3 \cdot 10^{26}$	0.0742	0.46	0.43
$4 \cdot 10^{26}$	0.0992	0.80	0.77
$5 \cdot 10^{26}$	0.1242	1.24	1.21
$6 \cdot 10^{26}$	0.1493	1.78	1.75

[a]Calculated using Eq. 33. [b]Ref. 46 (Fig. 4a). [c]Calculated using Eq. 40 (depletion approximation).

When all available sites in the grain boundary core are occupied by oxygen vacancies, the depletion approximation leads to a slight underestimation of the space-charge potential, which in this case amounts to ~ 0.03 V. In other words, the depleted oxygen vacancies in the space-charge layers add in this case an additional 0.03 V to the space-charge potential.

3.3.2 Concentration profiles in the space-charge layers

As already indicated, positive charges deplete and negative charges accumulate in the space-charge layers adjacent to a positively charged core. In this section, we will show concentration profiles of the relevant defects in the space-charge layers. General solutions for the concentration profiles have been derived elsewhere [47]. We will only consider the Mott-Schottky approximation.

By inserting Eq. 37 into Eq. 31 and using the definition of the Debye length (Eq. 38) we obtain the relative oxygen vacancy concentration as a function of position x in the space-charge layer:

$$\frac{c_{V_O^{\bullet\bullet}}(x)}{c_{V_O^{\bullet\bullet}}(\infty)} = \exp\left[-\frac{1}{2}\left(\frac{x-\lambda^*}{L_D}\right)^2\right]. \tag{41}$$

We can similarly obtain the concentration profiles for defects with other charges. The concentration of protons[10] and electron holes read

$$\frac{c_{OH_O^{\bullet}}(x)}{c_{OH_O^{\bullet}}(\infty)} = \exp\left[-\frac{1}{4}\left(\frac{x-\lambda^*}{L_D}\right)^2\right] \tag{42}$$

[10] We recall from Section 2.1.2 that the term for the *proton* defect here is used for a hydroxide ion residing on an oxygen site, $OH_O^{\bullet}$.

$$\frac{c_{\mathrm{h}^{\bullet}}(x)}{c_{\mathrm{h}^{\bullet}}(\infty)} = \exp\left[-\frac{1}{4}\left(\frac{x-\lambda^*}{L_\mathrm{D}}\right)^2\right] \tag{43}$$

Thus, electron holes and protons follow the same concentration profile, whereas the oxygen vacancies follow a quadratic depletion as compared to those singly charged defects. Concentration profiles for protons are given in Fig. 3.6 with $c_{\mathrm{Acc}'}(\infty) = 6 \cdot 10^{19}$ cm^{-3}, corresponding to the dopant concentration in 0.5 % Sr-doped $LaNbO_4$. With increasing $\Delta\varphi(0)$, λ^* increases, while L_D remains unchanged. Keeping $\Delta\varphi(0)$ constant and changing the temperature, λ^* is unchanged while L_D increases from 0.61 nm at 200 °C to 0.83 nm at 600 °C. This results in a more severe depletion at the lower temperatures. In the last example, ε_r is varied from 20[11] to 60, and it is seen that λ^* increases with increasing ε_r, while the concentration at $x = 0$ remains unchanged.

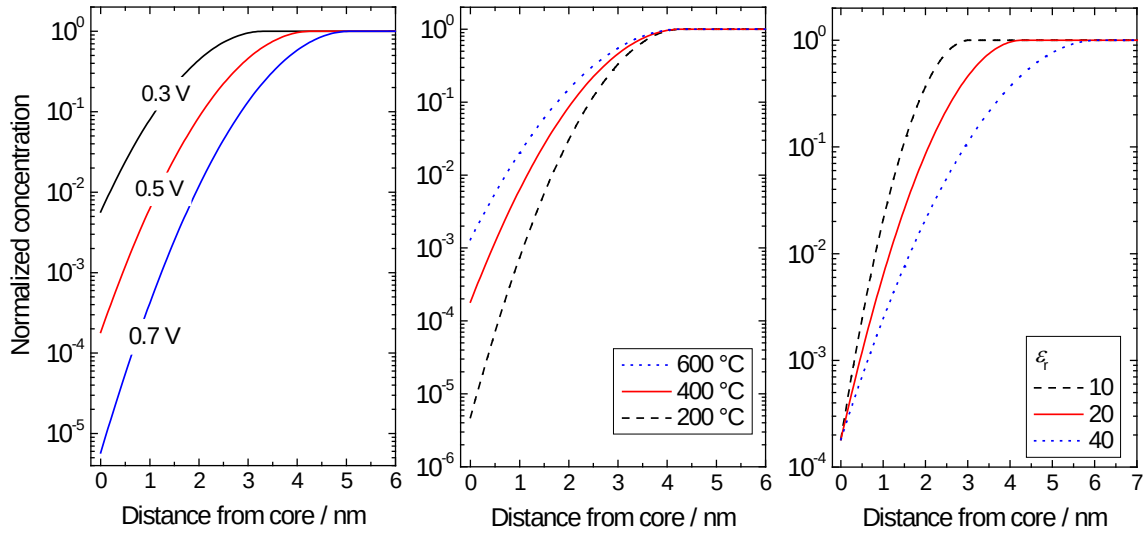

Fig. 3.6. Normalized proton concentration in the space-charge layer assuming the Mott-Schottky approximation with $c_{\mathrm{Acc}'}(\infty) = 6 \cdot 10^{19}$ cm^{-3}. Left: Variable $\Delta\varphi(0)$, $\varepsilon_\mathrm{r} = 20$, temperature = 400 °C. Middle: Variable temperature, $\varepsilon_\mathrm{r} = 20$, $\Delta\varphi(0) = 0.5$ V. Right: Variable ε_r, temperature = 400 °C, $\Delta\varphi(0) = 0.5$ V.

The concentration profiles of protons and oxygen vacancies are plotted in Fig. 3.7. In these figures, only the grain interior concentrations are changed. Due to the quadratic depletion of the oxygen vacancies in the space-charge layer, protons become relatively more dominating than compared to the oxygen vacancies.

[11] For $LaNbO_4$, ε_r has been reported to 19 [48].

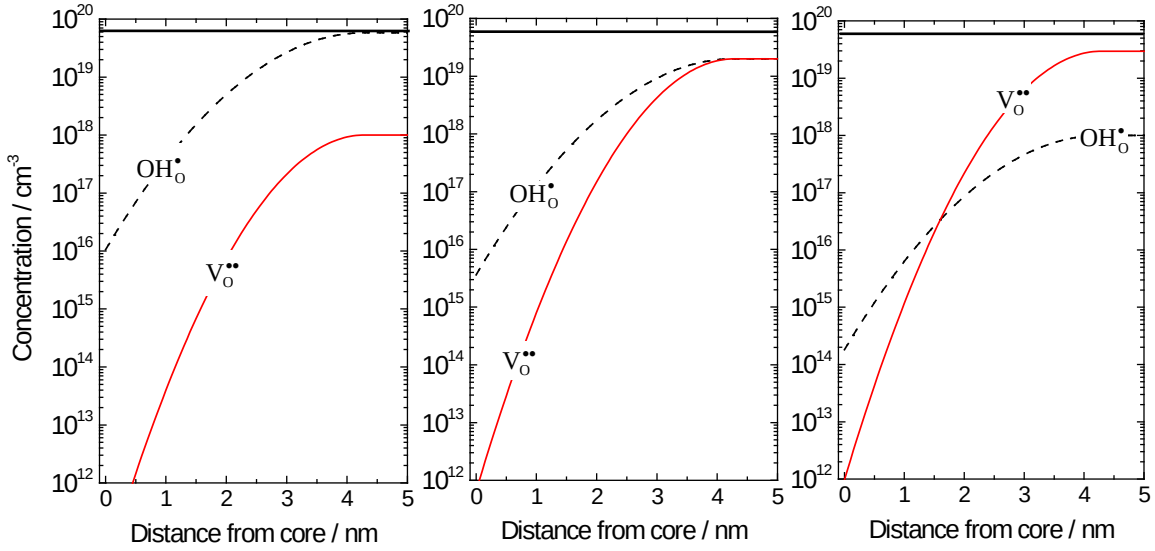

Fig. 3.7. Concentration profiles of protons and oxygen vacancies in the space-charge layers with different grain interior defect concentrations at 400 °C. $\Delta\varphi(0)$ = 0.5V, ε_r = 20 and $c_{Acc'}$ = 6 10 ^{19} cm^{-3}. Left : $c_{OH_O^\bullet}(\infty) = 5.8\cdot10^{19}\,\mathrm{cm}^{-3}, c_{V_O^{\bullet\bullet}}(\infty) = 1\cdot10^{18}\,\mathrm{cm}^{-3}$ · Middle : $c_{OH_O^\bullet}(\infty) = 2\cdot10^{19}\,\mathrm{cm}^{-3}, c_{V_O^{\bullet\bullet}}(\infty) = 2\cdot10^{19}\,\mathrm{cm}^{-3}$ · Right : $c_{OH_O^\bullet}(\infty) = 1\cdot10^{18}\,\mathrm{cm}^{-3}, c_{V_O^{\bullet\bullet}}(\infty) = 2.95\cdot10^{19}\,\mathrm{cm}^{-3}$. Acceptor level is also indicated.

Since electrons are negatively charged, they accumulate in the space-charge layers. As long as the concentration of electrons in the space-charge layer is much less than the acceptor-level, the concentration profile is

$$\frac{c_{e'}(x)}{c_{e'}(\infty)} = \exp\left[\frac{1}{4}\left(\frac{x-\lambda^*}{L_D}\right)^2\right]. \qquad (44)$$

When the concentration approaches that of the acceptor, the degree of accumulation levels off and the electron concentration eventually becomes equal to the acceptor level. This can lead to an increased contribution of n-type electronic conductivity to the grain boundary conductivity.

3.3.3 Intrinsic vs. extrinsic effects

The total grain boundary resistance is the sum of the resistance originating from depletion of charge carriers in the space-charge layers, R_{gb}^{sc}, and the resistance due to current constriction caused by blocking secondary phases, R_{gb}^{cc}. (In this we have assumed the resistance over a grain boundary core is negligible.) Both R_{gb}^{sc} and R_{gb}^{cc} are dependent on how much the secondary phase covers in the grain boundaries, but with different functional dependencies. This is emphasised in Fig. 3.8 where R_{gb}^{cc} and R_{gb}^{sc} are plotted as a function of the fraction of contacted area. For $\Delta\varphi(0)$ > 0.4 V, R_{gb}^{sc} dominates both for pure and impure samples.

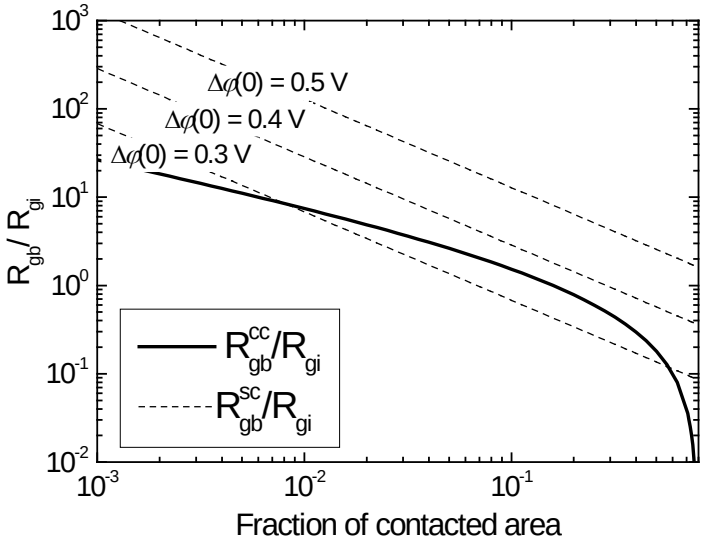

Fig. 3.8. Grain boundary resistance caused by the space-charge effect and by current constriction (for n = 1, *cf.* Fig. 3.2) as a function of the fraction of contacted area at the grain boundary. To calculate R_{gb}^{sc}, temperature = 500 °C, $\lambda^* = 10$ nm, and grain size = 5 μm were used.

3.4 Transport along interfaces

Up till now, we have considered the detrimental roles exhibited by impurity phases and space-charge layers on the transport characteristics across grain boundaries. In that case, we do not need to take into account the transport that occurs along the grain boundaries because – in addition to exhibit a lower specific conductivity than grain interior – the area represented by grain boundaries in parallel to grain interior is small, and the transport will therefore proceed in the grain interiors. Only when the conductivity of the grain boundaries is much higher than in grain interior, this pathway needs to be taken into account on the overall transport in polycrystalline ceramics.

In this section we will, in addition to grain boundaries, consider the interface consisting of an ionic conductor and an insulator, and the interface consisting of two different ionic conductors (but with same charge carrier). We discuss the enhanced conductivity in these interfacial regions, which is either caused by increased mobility or concentration. Increased mobilities could occur in interfacial regions (including the grain boundary core) that greatly differ from what is encountered in the grain interiors. Increased concentrations, on the other hand, are related to space-charge effects.

3.4.1 Mobility effects caused by elastic strain and misfit dislocations

Let us consider an internal interface where two crystal lattices with different symmetry and/or different lattice parameters are joined. An interfacial region where the local structure is different from bulk is then formed. Elastic strain will develop in the interfacial region,

accompanied by a higher density of misfit dislocations. The greater the mismatch between the adjacent phases, the greater the elastic strain and the higher number of misfit dislocations in the interfacial region.

Experimental studies on the interfacial transport properties in thin film systems based on oxide ion conductors have been performed by several research groups; we will, however, in the following restrict ourselves to those reported by Janek and co-workers. Using pulsed laser deposition, they have constructed multilayer systems consisting of cubic stabilised zirconia and different insulating oxides. The systems comprise CSZ/Al_2O_3 (CSZ: calcia-stabilised zirconia) [13], YSZ/Y_2O_3 [49], YSZ/Lu_2O_2 [50,51] and YSZ/Sc_2O_3 [50,51]. For CSZ/Al_2O_3, an incoherent boundary was formed, and a conductivity enhancement of a factor of 60 was reported at 575 °C when decreasing the interlayer distance down to 40 nm [13]. The increased ionic conductivity was interpreted to result from an increased density of dislocations in the interfacial region.

For the other multilayer systems, smaller changes in the conductivity were reported. Here the oxide ion conductor (YSZ) was combined with different rare-earth sesquioxides. These sesquioxides crystallise in a fluorite-related structure with lattice constants comparable to that of YSZ. Thus, due to a smaller crystal mismatch, coherent and semi-coherent boundaries were formed, and the interfacial transport properties were mainly determined by elastic strains. An increased ionic conductivity was encountered for YSZ/Y_2O_3, while YSZ/Lu_2O_3 appeared to be unchanged. For YSZ/Sc_2O_3, a decrease in the conductivity was reported. The authors argued that this could be understood by taking into account a positive, nearly zero and negative mismatch factor for YSZ/Y_2O_3, YSZ/Lu_2O_3, and YSZ/Sc_2O_3, respectively. Positive mismatch factors – causing dilatative strain – enhance the conductivity, whereas negative mismatch factors – causing compressive strain – decrease the conductivity.

For all systems, the change in the ionic conductivity was linked to the activation enthalpy of mobility. That is, a higher ionic conductivity coincided with a lower activation enthalpy of mobility, suggesting that the higher ionic conductivity was a result of increased charge carrier mobility.

We will end this section by mentioning a paper in which the electrical properties of a multilayer structure consisting of YSZ and $SrTiO_3$ were reported [52]. The authors reported an increase in the room temperature ionic conductivity up to eight orders of magnitude. The alleged colossal ionic conductivity enhancement has, however, been met with some scepticism (see *e.g.* Refs. 50, 53 and 54). To the author's best knowledge, an undisputed confirmation of the oxide ion as the charge carrier in this multilayer system has yet not been reported.

3.4.2 Enhanced charge carrier concentrations in space-charge layers

Addition of small particles of insulating oxides to ionic conductors may – under certain conditions – greatly enhance the ionic conductivity. This was probably first recognised for the system LiI/Al_2O_3 [55]. In LiI, which is a Li^+ conductor, the transport occurs via the vacancy mechanism. When Al_2O_3 is added to a matrix of LiI, lithium ions adsorb to the surface of the oxide and thereby create a positively charged oxide surface. Thus, the concentration of the negatively charged defects, and thereby lithium vacancies, will increase in the LiI matrix in the vicinity of the Al_2O_3 particles. If the alumina particles percolate, a high conductivity path is formed.

By means of decreasing the acceptor dopant level in CeO_2, the n-type electronic conductivity contribution to the overall conductivity increases. The space-charge potential in CeO_2 is positive [9], and electrons will therefore accumulate in the space-charge layers. We would therefore expect that nano-grained ceramics of CeO_2 exhibit a higher portion of electronic conductivity than micro-grained ceramics. Indeed, this has been confirmed by several authors (see *e.g.* Refs. 23 and 56), and it was concluded by Kim and Maier [56] that the highly electronically conducting space-charge layers can control the overall conductivity in nano-CeO_2.

As a final example devoted to high conductivity along interfaces, we will consider a multilayer configuration consisting of alternating layers of thin films of BaF_2 and CaF_2, as reported by Sata and co-workers [57]. These fluorides are fluoride ion conductors, and the multilayer systems were grown by molecular beam epitaxy. By decreasing the interlayer distance, the conductivity increased, exceeding the conductivity of pure BaF_2 (which is the best conductor of those fluorides) by more than two orders of magnitude at 250 °C. The increased conductivity is due to the increased concentration of charge carriers in the space-charge layers adjacent to the phase boundaries, and the relative contribution of these layers to the total conductivity increases as the space-charge layers progressively makes up a larger volume fraction of the sample.

3.4.3 On the possibility of ionic transport in the grain boundary core

The low temperature transport properties of dense ceramics (prepared by spark plasma sintering) of acceptor doped ZrO_2 and CeO_2 with nano-sized grains (typically less than 100 nm) have been reported by several research groups. Kim and co-workers [58-60] report that the conductivity of the nanometric ceramics increase with increasing water vapour pressure and decreasing grain size at temperatures less than ~ 150 °C. By means of a dense YSZ ceramic with 15 nm grains in a water concentration cell at room temperature, voltages up to

~ 100 mV were measured [58]. The authors conclude that proton conductivity along the grain boundaries is responsible for these effects. Similar results were obtained by Chiodelli *et al.* [61].

Recently, Perez-Coll and Mather [62] disputed the conclusion of Kim and co-workers on the conductivity mechanism at low temperature. They argue that the low temperature proton transport is essentially attributable to processes on surfaces (externally or internally along pores), where physisorbed water layers play an important role. Apparently, low temperature conductivity measurements in humid atmospheres bring about certain experimentally challenges. Surface conduction can be reduced, as done by the investigators, by coating the lateral surface of the samples with a polymeric paint. It also appears, based on the experimental descriptions given, that some of the conductivity measurements could benefit from better experimental control of the water vapour pressure.

Although under debate, *if* the proton conduction pathway proposed by Kim *et al.* [59] is correct, it is still unclear why the grain boundaries in nano grained YSZ would serve as a fast conduction pathway. One possibility, suggested by Avila-Paredes and co-workers [60], is linked to redistribution of protons from grain interior to the grain boundary core, as discussed in Section 3.3.1. It is possible that the core becomes fully hydrated, even if grain interior contains relatively small amounts of protons. How much the core proton mobility must be increased compared to the grain interior value in order to account for the rather large conductivity effects seems, at present, to be an unanswered question.

3.5 Chemical polarization

When applying a DC voltage on a mixed conductor[12] using electrodes that are selectively blocking for the ionic or the electronic charge carrier, compositional variations in the mixed conductor will occur. Initially, when the voltage is switched on, both ions and electrons migrate. Eventually, when a steady state is reached, only the non-blocked species will diffuse. Thus, a concentration profile of the blocked species through the sample evolves as a function of time. When steady state is reached, the gradient in the chemical potential of the blocked charge carrier compensates the electrical potential gradient. Or, put somewhat differently, the chemical polarization balances the electrical one.

[12] Mixed conductors are materials with considerable ionic and electronic conductivity. Applying a voltage across a mixed conductor with one selectively blocking (blocking either for the ionic or the electronic charge carrier) and one reversible electrode is known as Hebb-Wagner polarization, and is a powerful technique for determination of the electronic (or ionic) contribution to the total conductivity.

The treatment given below is partly adopted from Ref. 16 (Sec. 7.3.4) and from Ref. 63. Our treatment, however, is mainly qualitative and heuristic in nature, and we preferably use simplified mathematical expressions and schematic drawings. For the mathematical deduction of the impedance equations, interested readers are referred to Ref. 63.

Jamnik and Maier [64] and Lai and Haile [63] have described the transport of the charge carriers in a single crystal of a mixed conductor placed between two electrodes using an equivalent circuit as shown in Fig. 3.9.

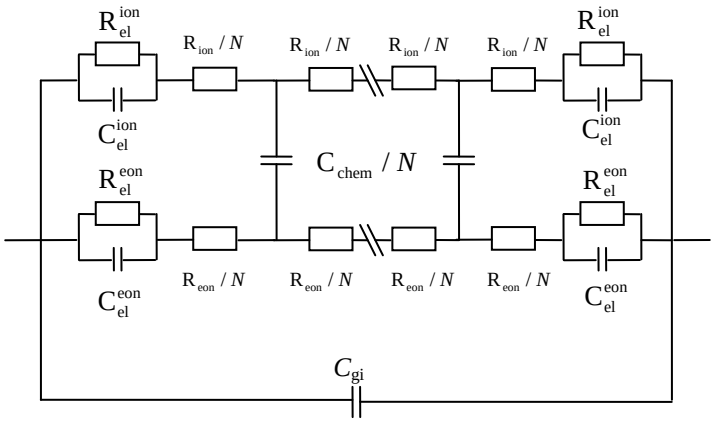

Fig. 3.9. Equivalent circuit of a mixed conductor placed between two electrodes. The ionic and electronic currents flow on separate rails in parallel. The mixed conductor consists of N parts with corresponding total ionic and electronic resistance, R^{ion} and R^{eon}. Transient currents can pass between those rails by charging the chemical capacitor. Simplified electrode equivalent circuits are assumed to consist of parallel connections of pairs of resistors and capacitors (with subscript el). C_{gi} is the grain interior dielectric capacitance.

Central in this model is the chemical capacitance associated to the coupling between the ionic and electronic current rails. According to Lai and Haile, the chemical capacitance is "a measure of the ability of the system to store chemical energy in the form of changes in stoichiometry in response to changes in oxygen partial pressure". The total chemical capacitance, C_{chem}, is the inverse of the sum of the inverse partial chemical capacitances, and in a mixed conductor (assuming dilute charge carriers) C_{chem} is [65]

$$C_{\text{chem}} = \left(\frac{1}{C_{\text{chem,ion}}} + \frac{1}{C_{\text{chem,eon}}} \right)^{-1} = \frac{e^2}{k_B T} AL \left(\frac{1}{z_{\text{ion}}^2 c_{\text{ion}}} + \frac{1}{z_{\text{eon}}^2 c_{\text{eon}}} \right)^{-1} . \qquad (45)$$

We see that C_{chem} is proportional to AL, in contrast to a "normal" dielectric capacitance which is proportional to A/L. From Eq. 45 it follows that C_{chem} increases with increasing charge carrier concentration and that its upper limit is determined by the charge carrier with the lowest concentration. For a mixed conducting sample of size A = 1 cm^2, L = 0.1 cm where $c_{ion} = c_{eon} = 1 \cdot 10^{19}$ cm^{-3}, C_{chem} = 2 F at 500 °C. Values up to 250 F have been reported for Sm-doped CeO_2 [63] and ~ 0.1 F for Fe-doped $SrTiO_3$ [66]. In pure ionic conductors with a "typical" sample size (A = 1 cm^2, L = 0.1 cm), capacitances of the electrode related

processes typically range between 1 µF – 0.1 F. Hence, C_{chem} may be significantly larger than the capacitances associated to electrode processes.

The impedance of the equivalent circuit in Fig. 3.9 is displayed schematically in a Nyquist-plot in Fig. 3.10. In Fig. 3.10 we have assumed ideal selectively blocking electrodes, that is $R_{el}^{ion} = \infty$ and $R_{el}^{eon} = 0$. Firstly, we recognize the grain interior arc at the highest frequencies. At lower frequencies we see a half tear-drop shape. At the onset of that feature, corresponding to the highest frequencies of this contribution, we see a straight line with slope = 1. Depending on the circuit's parameters, as defined in Fig. 3.9, this shape can transform into a symmetrical semicircle, however, it maintains its characteristic tear-drop shape for a rather wide range of parameters in true mixed conductors. In electrochemistry, similar tear-drop shaped contributions are observed in Nyquist-plots for diffusion-controlled processes at the electrodes and are called finite-length Warburg impedances. In our case, we see that there is no need for such diffusion-controlled processes at the electrodes to still observe a tear-drop shape of a contribution related to chemical polarization in a Nyquist-plot.

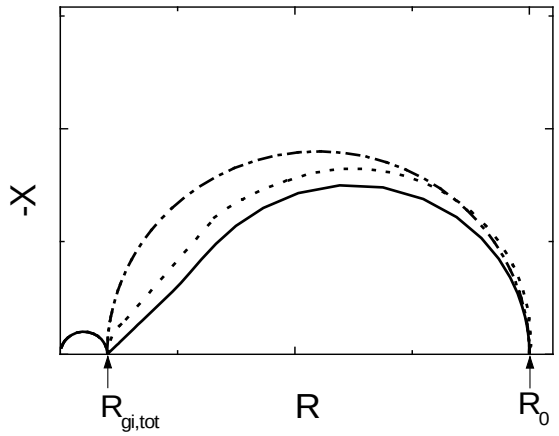

Fig. 3.10. Schematic Nyquist-plots for a mixed conductor with ideal selectively blocking electrodes for the ions based on the equivalent circuit given in Fig. 3.9. The solid line corresponds to a mixed conductor where $R_{ion} \sim R_{eon}$. With increasing ratio of R_{eon} to R_{ion}, as is accomplished by a decrease in c_{eon}, the half tear-drop shape transforms gradually into a semicircle as indicate by the dotted lines. Impedances are normalized for easy comparison.

The high- and low-frequency limits of the circuit in Fig. 3.9[13], referred to as $R_{gi,tot}$ and R_0 in Fig. 3.10, are evaluated in the following. At high frequencies, all capacitors are shorted, leaving us with the equivalent circuit shown at the left hand side in Fig. 3.11. Thus, $(R_{gi,tot})^{-1} = (R_{ion})^{-1} + (R_{eon})^{-1}$. At low frequencies, all capacitors all closed, resulting in the circuit shown in the middle of Fig. 3.11. We then obtain $(R_0)^{-1} = (R_{ion} + 2R_{el}^{ion})^{-1} + (R_{eon} + 2R_{el}^{eon})^{-1}$. In a Hebb-Wagner polarization experiment one uses selectively ion-blocking electrodes, *i.e.*

[13] We now conveniently neglect C_{gi} from the circuit given in Fig. 3.9. This basically removes the bulk semicircle from the impedance spectra, leaving behind a offset along the real axis equal to $R_{gi,tot}$.

$R_{el}^{ion} = \infty$ and $R_{el}^{eon} = 0$. Then, $R_0 = R_{eon}$ and the electronic contribution to the total resistance can be determined. For a pure ionic conductor the difference between R_0 and $R_{gi,tot}$ is equal to the electrode resistance. In contrast, for a mixed conductor the difference is a function of all of the four resistances given in Fig. 3.9.

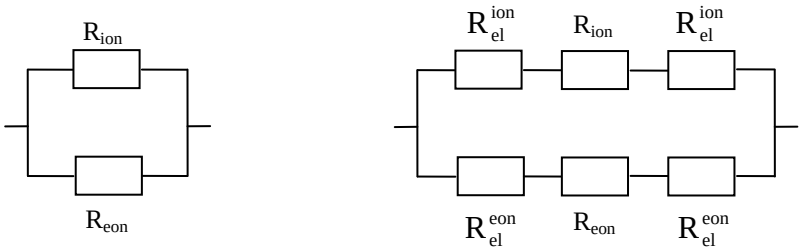

Fig. 3.11. Simplified equivalent circuits for a mixed conductor placed between two electrodes when the ionic charge carrier is blocked at the electrodes. C_{gi} is neglected. Left: High-frequency limit, when all capacitors are shorted. Right: Low-frequency limit, when all capacitors are blocking (open).

Let us continue by discussing how the electrode transfer impedance of the non-blocked species comes into account by allowing non-zero values for R_{el}^{eon}. As suggested by Maier [16] (Sec. 7.3.4), this situation can, when the ionic charge carrier is fully blocked, be approximated by using the equivalent circuit in the inset of Fig. 3.12 as long as C_{chem} is considerably larger than C_{el}^{eon}. Using this circuit as a starting point, we can further simplify and reason out circuits (also shown in Fig. 3.12) that hold as good approximations in their corresponding frequency ranges. We see, by comparison between Fig. 3.10 and Fig. 3.12, that the introduction of real electrodes exhibiting transfer resistance towards the non-blocked species has added an additional semicircle to the impedance spectrum. The beginning of the tear-drop shape is simplified using a Warburg element with impedance equal to $\frac{1}{\sqrt{i\omega\tau_{chem}/2}}$ where τ_{chem} is the relaxation time of the last semicircle. If, on the other hand, C_{chem} is comparable or even lower than C_{el}^{eon}, the contribution of the transfer resistance of the electrons merges with the tear-drop shape, resulting in a somewhat distorted semicircle where the radius increases with increasing R_{el}^{eon}.

Finally, we should also consider the effect of having imperfect blocking of ions at the electrodes, *i.e.* $R_{el}^{ion} \neq \infty$ while maintaining perfect reversibility of the electrons. Provided that C_{chem} is larger than C_{el}^{ion}, the leakage of ionic current results in a depressed low frequency Warburg response. The magnitude of this contribution is reduced with increasing leakage of ionic current. These conditions, *i.e.* $R_{el}^{ion} \neq \infty, R_{el}^{eon} = 0, C_{chem} > C_{el}^{ion}$, are precisely encountered while using noble metals as electrodes on Sm-doped CeO_2 [63]. Based on AC impedance spectroscopy in a wide experimental window and an appropriate methodology of data

analysis, Chueh and co-workers could extract the essential electrical and electrochemical parameters of the systems Sm-doped CeO_2 with Au- and Pt-electrodes [67].

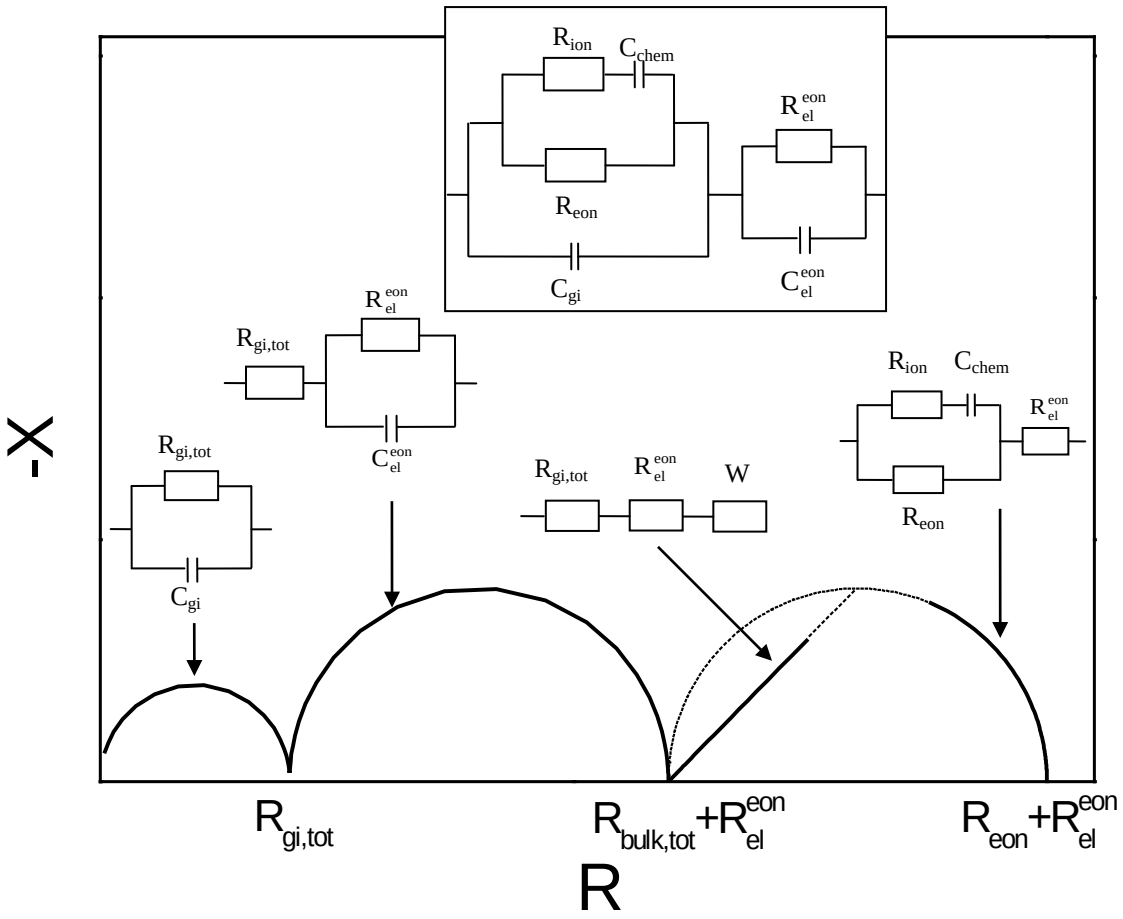

Fig. 3.12. Impedance spectrum for a mixed conductor placed between two ionically blocking electrodes, and with a non-zero electrode resistance for the electronic charge carrier. The impedance of the sample can be approximated by different equivalent circuit in different frequency ranges as indicated in the figure. The approximations fail in the region of the broken line where the circuit given in Fig. 3.9 should be used. In this range, *i.e.* between the Warburg straight line and somewhat to the right of the summit of the last semicircle, the impedance swells out as indicated in Fig. 3.10. The impedance spectrum was simulated using the following values: R_{ion} = 3 Ω; R_{eon} = 6 Ω; R_{el}^{eon} = 4 Ω; C_{gi} = 5 nF; C_{el}^{eon} = 10 μF; and C_{chem} = 0.1 F. The figure is adopted from Ref. 16 (Fig. 7.45).

We have seen that compositional changes in a mixed conductor are induced when we apply selectively blocking electrodes. Compositional variations in the grains can also occur if different charge carriers dominate in grain interior and in the grain boundaries. This concept has been experimentally confirmed on a bicrystal of acceptor-doped $SrTiO_3$ [66], in which both oxygen vacancies and electron holes contribute to the bulk conductivity. Oxygen vacancies, having a double charge, become more depleted in the space charge layers adjacent to the grain boundary core compared to the singly charged electron holes. Hence, the grain boundary conductivity is essentially electronic. Impedance measurements were carried out on samples with electrodes that are reversible for both ions and electrons, *i.e.* $R_{el}^{ion} = 0, R_{el}^{eon} = 0$. For the single crystal only the bulk semicircle was observed in the Nyquist plots. For the

bicrystal two contributions were additionally observed; at medium frequencies a grain boundary semicircle, and at the lowest frequencies a tear-drop shape. Consequently, selectively blocking grain boundaries can, in the same way as electrodes, cause chemical polarization.

The above example considered a bicrystal. According to Jamnik and co-workers [66], chemical polarization should also take place in polycrystalline samples. A key point in this context is the volume in which the chemical polarization is confined. Thus, when grain boundaries in a polycrystalline ceramic sample induce chemical polarization, it is the size of the grains and not of the entire sample that determines C_{chem}.[14] Chemical polarization in a polycrystal will, as a result of the smaller dimensions of the grains in a polycrystalline sample (*cf.* Eq. 45) appear in a much higher frequency range than that of a single crystal [68].

An even more complex scenario may arise in the case of a polycrystalline sample of which both the electrodes *and* grain boundaries are selectively blocking. Assuming that the electrodes and the grain boundaries block and conduct the same charge carriers, we have to take into account the different volumes the electrodes and grain boundaries work on. If, on the other hand, the transport characteristics of the electrodes and grain boundaries are very different, a more complex case is expected, and this will not be further elaborated on here.

We have so far only considered a mixed conductor where one charge carrier is ionic and the other electronic. Let us now widen our perspectives by discussing a scenario in which two different *ionic* charge carriers dominate the conductivity. This is for example encountered in high temperature proton conductors in which protons and oxygen vacancies under certain conditions simultaneously contribute to the conductivity. As discussed in Section 2.2, there is no principal difference between an electron hole (or an electron) that migrates by the small polaron mechanism and other, ionic charge carriers. Induced chemical polarization in a mixed oxide ion and protonic conductor should therefore be regarded as an option if the electrodes or grain boundaries are selectively blocking. This scenario will be dealt with in MANUSCRIPT A.

[14] The *total* chemical capacitance of a polycrystalline sample will also be dependent on the sample size, but the sample dimensions enter as A/L. The total chemical capacitance is proportional to (assuming cubic grains of grain size G) G^2A/L. This is elaborated on in MANUSCRIPT A.

4. Experimental methods, equipment and interpretation of data

This chapter gives more details on experimental details than there has been found room for in the subsequent papers. In particular, this concerns the description of the employed $LaNbO_4$-based samples. Regarding impedance spectroscopy, this chapter also provides a supplementary description and discussion for fitting of impedance spectra into equivalent circuits.

4.1 Sample preparation and characterization

In order to study electrical properties of grain boundaries in ceramics, microstructural and chemical information about the investigated sample is crucial. This section therefore provides experimental details and results in addition to what is found in the subsequent papers.

4.1.1 $LaNbO_4$

Powders of nominal composition $La_{0.995}Sr_{0.005}NbO_{4-\delta}$ (LNS0.5) were provided by Cerpotech (Trondheim, Norway) by means of a spray pyrolysis method using aqueous solutions [69]. According to the supplier, most of the SiO_2 impurities in the provided powders of LNS0.5 probably originate from the precursors used in the spray pyrolysis. From a quoted SiO_2 content of less than 50 ppm (by mass) in La_2O_3 (for the niobium source it was quoted less than 1 ppm), the SiO_2 content was calculated to less than 30 ppm (by mass) in LNS0.5, corresponding to a molar ratio of Si to the cations of less than 70 ppm.

Polycrystalline samples were made by uniaxially cold-pressing the powder at ~ 100–110 MPa into cylindrical pellets of diameter of 25 mm, followed by sintering on a Pt-foil. Sintering temperatures and times were varied between 1200–1400 °C and 5–50 h, respectively. Fig. 4.1 displays an x-ray diffractogram of a sintered sample.

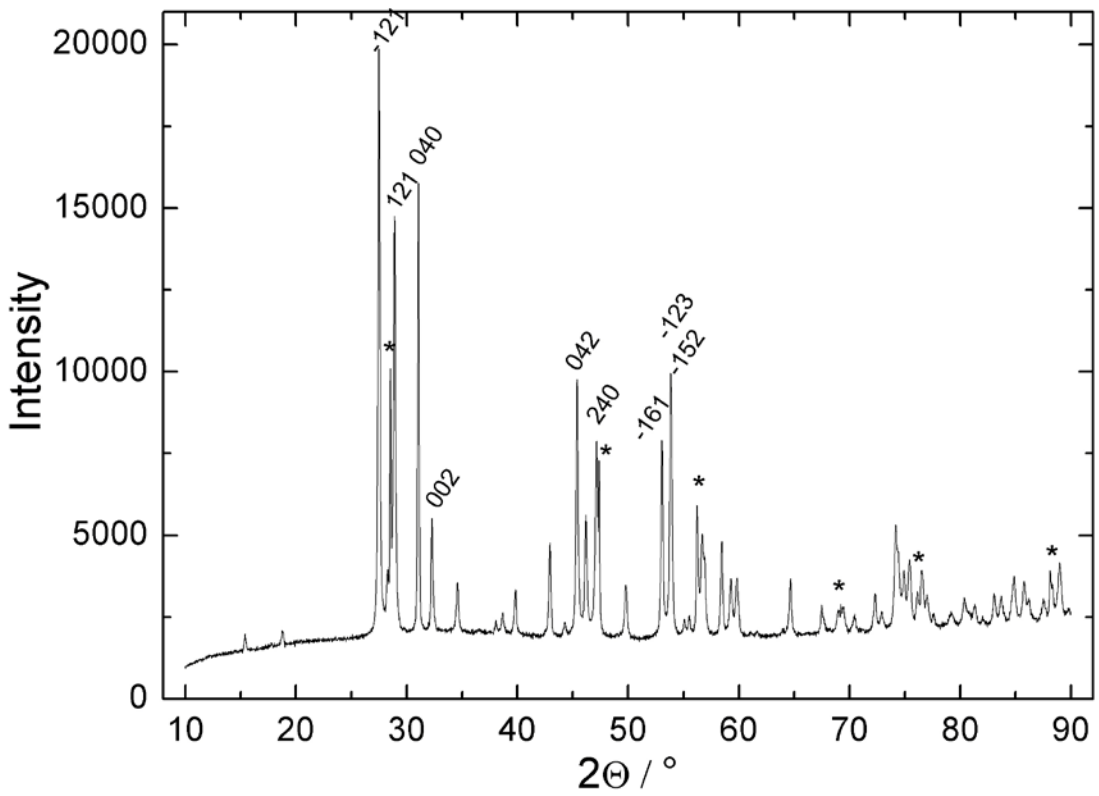

Fig. 4.1. X-ray diffraction pattern of LNS0.5 (and Si as internal standard, labelled with *). Some crystallographic planes are indicated.

All reflections of the x-ray pattern could be indexed according to a monoclinic Fergusonite-type unit cell.

Fig. 4.2 shows SEM micrographs of the surfaces of the as-sintered samples. All of the samples exhibited a dense microstructure with average grain size of ~ 5 µm. This was supported by measurement of the relative density, yielding values > 90 %, slightly decreasing with increasing sintering temperature. Furthermore, the microstructure underneath the surface was investigated by polishing the sintered samples and subsequent thermal etching. Representative SEM micrographs are shown in Fig. 4.3. Probably as a result of the polishing, it was encountered that some grains were removed from the surface of the samples ("grain pullout"), but otherwise appeared as dense with some closed porosity.

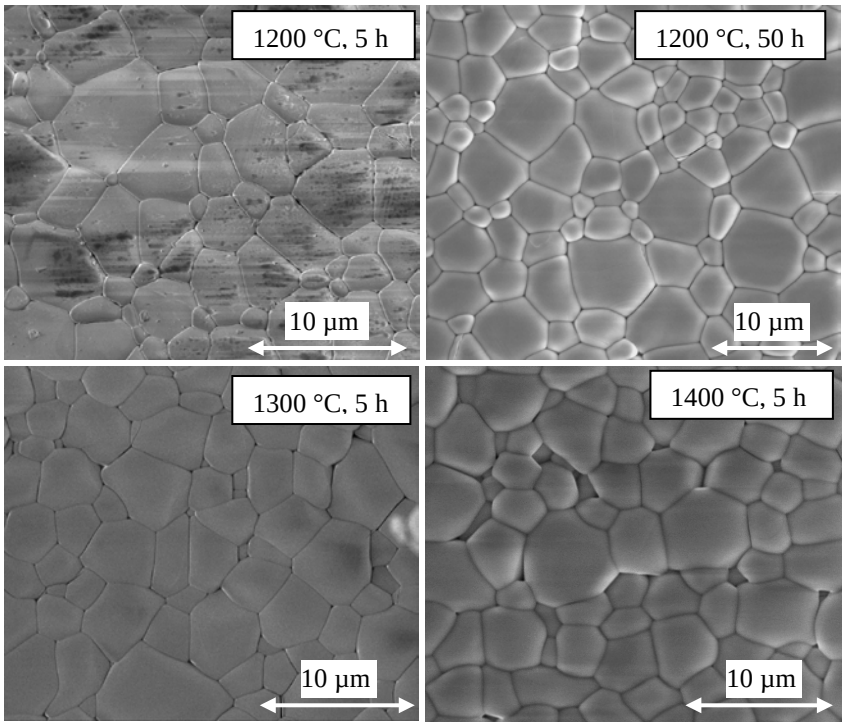

Fig. 4.2. SEM micrographs of surfaces of as-sintered samples of LNS0.5. Sintering temperatures and times are given in the figures.

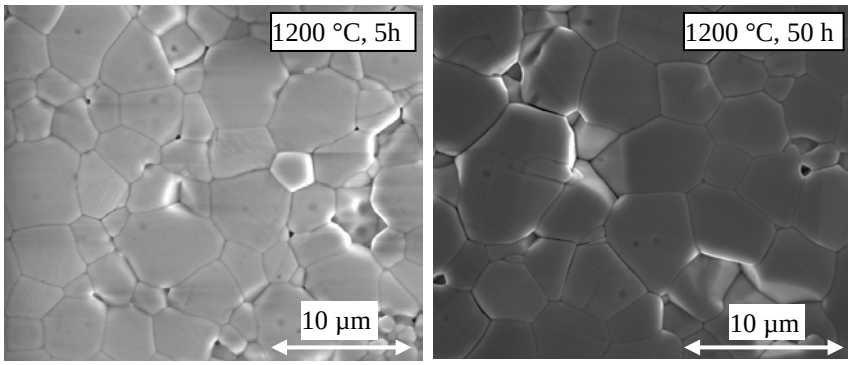

Fig. 4.3. SEM micrographs of polished samples of LNS0.5.

The microstructure and chemical composition of the grain boundaries and triple grain junctions of LNS0.5 sintered at 1200 °C for 50 h were investigated by means of transmission electron microscopy (TEM). A JEOL 2010F transmission electron microscope, equipped with a NORAN X-ray energy dispersive spectrometer (EDS) was used for observation and microanalysis; SPOT size 4, *i.e.* probe diameter ~3 nm, was used. Samples for TEM-investigations were prepared from both the as-sintered sample as well as from the sample which was subjected to the electrical characterization. Bright field TEM micrographs of the electrically characterized sample are shown in Fig. 4.4.

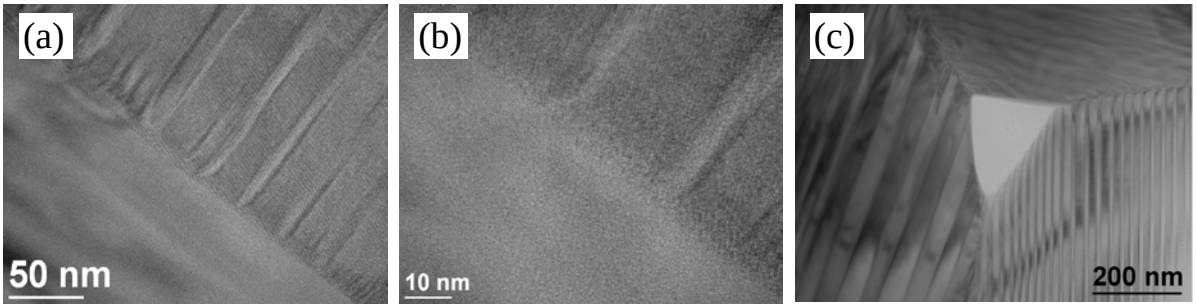

Fig. 4.4. Bright field TEM micrographs of LNS0.5 showing (a) and (b) clear grain boundaries, and (c) an amorphous phase at a triple grain junction.

In both investigated samples no impurities were detected along the grain boundaries. In some triple grain junctions, however, an amorphous impurity phase was detected. Details on the chemical composition of such an impurity phase and its surrounding are given in Fig. 4.5.

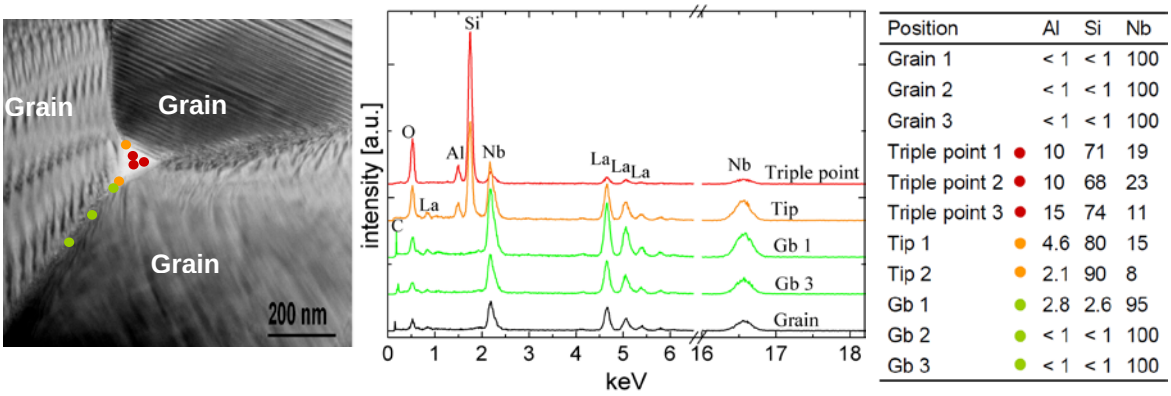

Position	Al	Si	Nb
Grain 1	< 1	< 1	100
Grain 2	< 1	< 1	100
Grain 3	< 1	< 1	100
Triple point 1	10	71	19
Triple point 2	10	68	23
Triple point 3	15	74	11
Tip 1	4.6	80	15
Tip 2	2.1	90	8
Gb 1	2.8	2.6	95
Gb 2	< 1	< 1	100
Gb 3	< 1	< 1	100

Fig. 4.5. Left: TEM micrograph of an amorphous phase at a triple grain junction in LNS0.5. Points in which spot analyses of the chemistry were done are indicated, and corresponding energy dispersive spectra are given in the middle. Right: Calculated atomic percents of Al, Si and Nb as a function of the indicated position. Al + Si + Nb = 100%.

The impurity phase was rich in Si and Al. It is furthermore seen that the concentration of Al and Si drastically drops below the detection limit of the EDS outside the amorphous impurity phase. The presence of an amorphous impurity phase rich in Si at triple grain junctions is often encountered in ceramics, as elaborated in Section 3.2. In our case, the impurities can probably be tracked to the precursors used in the spray pyrolysis. Since the impurities seem to be mainly residing at triple grain junctions, the overall fraction of clean grain boundaries should therefore we fairly high.

Section conclusion: The polycrystalline samples of LNS0.5 were dense. An impurity phase rich in Si was found at some triple grain junctions, while the grain boundaries appeared as clean.

4.1.2 $Er_2Ti_2O_7$ and $BaZrO_3$

For the $Er_2Ti_2O_7$- and $BaZrO_3$-based samples, we consider the description of the sample preparation and the chemical and microstructural characterisation in the following manuscripts as sufficient. The reader is therefore referred to the thesis manuscripts.

4.2 Apparatus for electrical measurement

4.2.1 Measurement cell

Samples were mounted in a measurement cell (Probostat, NorECs, Norway) as described in Fig. 4.6. This setup allows for electrical measurements in controlled atmospheres at elevated temperatures. The cell was put into a vertically positioned tubular furnace. The thyristor controlled furnace was controlled by a PID regulator (Eurotherm 2216) using a thermocouple placed next to the sample as temperature sensor. On basis of occasional tests of the furnace used for most of the electrical measurements, it is assumed that for the measurements presented in this thesis, thermal fluctuation are less than 0.2 °C.

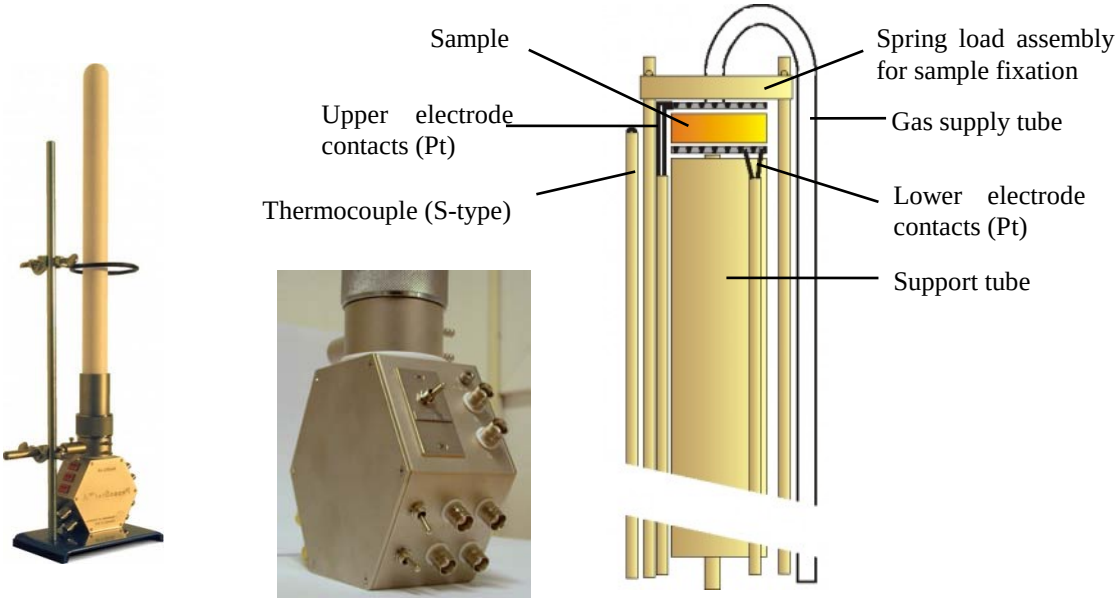

Fig. 4.6. Setup used for electrical measurements. Left: Appearance of whole measurement cell. Middle: Connection to electrodes with BNC connectors. Right: Schematic details from the upper part of the cell where the sample is placed. All pictures/figures: NorECs, Norway (www.norecs.com).

The electrical properties of the samples were investigated by connecting four Pt wires in pairs to the two porous Pt electrodes that were attached on the samples. 4 BNC cables were used to connect the measurement cell to the impedance spectrometer in such a way that

electrical signals from the lower part of the measurement cell to the impedance spectrometer were shielded, resulting in reduced noise.

4.2.2 Gas mixer

For controlling the gas atmosphere in the measurement cell, an in-house-built gas mixer was used, as described in Fig. 4.7. The gas mixer is based on several rotameters (Sho-Rate 1355, Brooks Instrument). pO_2 is set by repeatedly diluting GAS1 (GAS1 = O_2 or 5% H_2 in Ar) in the three first mixing stages (MIX1 – MIX3) with GAS2 (GAS2 = Ar). Then, pH_2O (or pD_2O) is set by splitting MIX3 and passing one fraction through saturated KBr (aq) and the other fraction through a column of P_2O_5 (for removal of water).

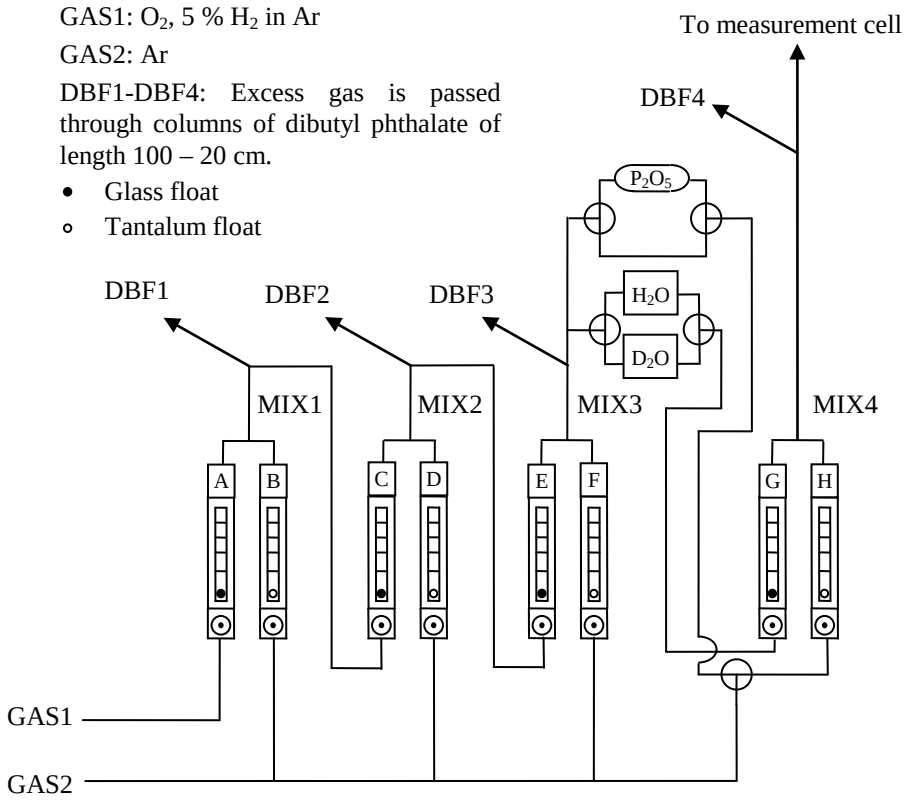

Fig. 4.7. Schematic drawing of the gas mixer used for the electrical measurements. Flowmeters A-H are variable-area rotameters with ball floats of glass or tantalum and precision 15-turn needle valves.

Under oxidising conditions, pO_2 is simply determined by the dilution with Ar, and the lower limit of pO_2 is in this case determined by O_2 residuals in Ar and the amount of leakage of air into the system, resulting typically in $pO_2 \sim 1 \cdot 10^{-5}$ atm. On the other hand, under reducing conditions, pO_2 is determined by the chemical equilibrium between hydrogen, oxygen and water according to

$$H_2(g) + ½\ O_2(g) = H_2O(g) \qquad (46)$$

$$K_W = \frac{pH_2O}{pH_2 pO_2^{1/2}} \quad (47)$$

Since the equilibrium constant varies with temperature, different pO_2 are obtained at different temperatures.

When passing the gas mixture through a saturated solution of KBr, pH_2O becomes 80% of relative humidity. At 25 °C, this results in pH_2O = 0.025 atm. Under oxidising conditions, wet O_2 is mixed with O_2 passing through the column of P_2O_5, enabling $5 \cdot 10^{-5}$ atm < pH_2O < 0.025 atm while keeping pO_2 nearly constant. Under reducing conditions, wet 5 % in Ar is mixed with Ar. This procedure ensures that pO_2 is constant (because the ratio pH_2/pH_2O is kept constant) while obtaining pH_2O in the range ~ 10^{-3} atm to 0.025 atm.

When passing a gas through D_2O instead of H_2O, the partial pressure of water becomes lower. According to Miles and Menzies [70], at 25 °C, the difference in the vapour pressures of D_2O and H_2O is 0.004 atm. Assuming that the partial pressure of D_2O becomes 80% of the vapour pressure when a gas mixture is passed through a solution of saturated KBr, pD_2O is 13% lower than that of pH_2O. In this thesis, isotope exchanges are mainly being used to probe qualitative differences, and the difference in the magnitude of the partial pressures of H_2O and D_2O can be safely ignored.

4.3 Impedance spectroscopy

Impedance spectroscopy is a powerful technique as it allows for differentiating of transport properties with different time constants. This is fulfilled by measuring the complex impedance over a broad frequency range, typically from a couple of MHz to tens of mHz. Depending on the sample characteristics and the operator's requirements, this range can be changed with experimental conditions. The AC signal applied to the sample is a sine wave characterized by its oscillation voltage (or current)[15], and is usually in the range 10 mV to 1 V. Additionally, a DC bias may be superimposed on the AC signal. One great advantage of the technique is that it eliminates the need for reversible electrodes.

The obtained impedance spectra for the investigated samples in this thesis are shown and discussed in the subsequent manuscripts. In this section, some space will be spend on introducing some general concepts that should be kept in mind when fitting impedance spectra recorded from ionically conducting ceramics. What we present here, therefore, serves

[15] Oscillation voltage is either specified with its peak amplitude or its root mean square (RMS) amplitude, which for a sine wave are related according to: peak amplitude = RMS amplitude · √2

as a common background for the treatment of the recorded impedance spectra in the subsequent manuscripts.

The grain interior behaviour of an ionic conductor can be represented by a parallel circuit consisting of a resistor (R) and a capacitor (C). This parallel circuit is known as the Voigt-element and is denoted (RC). The complex impedance is often represented in a Nyquist plot where the negative imaginary part, the negative reactance, -X, is plotted against the real part, the resistance R. The (RC) circuit takes a semicircular shape in the Nyquist plot, as seen in Fig. 4.8. For real polycrystalline samples, a slight depression of the grain interior semicircle is often encountered. This is commonly attributed to a distribution of the time constants of the individual grains, and in order to model this deviation from ideality, the constant phase element (CPE) is often used instead of the capacitor. The circuit is then denoted as (RQ). In general, the use of a CPE to replace a capacitor may not be unproblematic as it assumes a normal distribution of the logarithm of the time constants [71] (Section 13.1.1), which may or may not apply to the system of interest. Also, a CPE can not be applied for all frequencies [72] (see Section 2.2.2.2). A thorough discussion of this topic is outside the scope of this thesis, and the interested reader is referred to Ref. 71 (see Chapter 13.1) and Ref. 72 (see Section 2.2.2.2).

The parameters Y and n define the CPE, and the admittance of the CPE is expressed according to

$$Y_{CPE} = Y(j\omega)^n = Y\omega^n \cos\left(\frac{n\pi}{2}\right) + jY\omega^n \sin\left(\frac{n\pi}{2}\right) \qquad (48)$$

where $j = \sqrt{-1}$ and ω = angular frequency. According to this definition, Y takes S s^n as unit. The CPE has a very general dispersion formula. In fact, for the special cases where n = 1, 0.5, 0, and -1, the CPE represents a capacitor, a Warburg element, a resistor and an inductor, respectively. We will, however, only use the CPE for the purpose of describing the impedance of non-ideal capacitors. In Fig. 4.8, we have plotted the calculated complex impedance of a parallel circuit of a resistor and a CPE for three values of n.

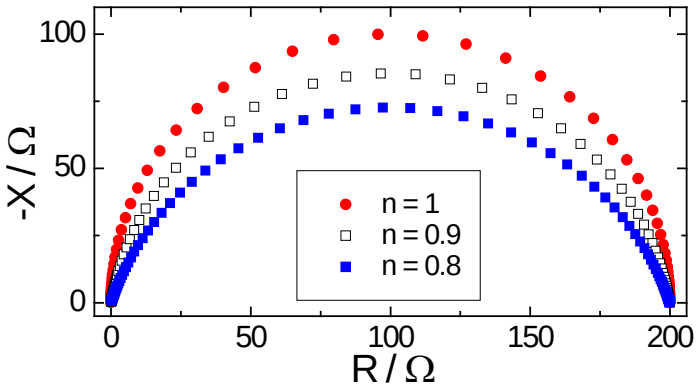

Fig. 4.8. The calculated complex impedance of a parallel circuit of a resistor and a constant phase element (CPE). When n = 1, the CPE represents an ideal capacitor.

The frequency at the apex corresponds to the characteristic frequency ω_0 of the circuit, and is given by $(1/YR)^{1/n}$. In the case of an ideal capacitor, $\omega_0 = (1/RC)$, and the quasi-equivalent capacitance of a parallel circuit consisting of a resistor and CPE is therefore given as

$$C = Y^{1/n}R^{(1-n)/n}. \tag{49}$$

In this thesis, we deal with ceramics that possess resistive grain boundaries. A further (RQ) circuit has then to be added in series, resulting in $(R_1Q_1)(R_2Q_2)$. If the characteristic frequencies of the grain interior and grain boundary contribution are sufficiently different, we obtain two semicircles in the Nyquist plot. The *n* value of the CPE associated to the grain boundaries is usually lower than that of grain interior. A possible interpretation of this commonly encountered experimental observation is that the grain boundaries exhibit a wider distribution in terms of time constants than grain interior. This can be rationalised when, for example, taking into account that different mismatch angles give rise to different space charges which in turn results in different electrical properties. Other reasons for a rather wide distribution of time constants may apply.

In order to obtain the specific local conductivities for grain interior (σ_{gi}) and grain boundaries (σ_{gb}), we assume that the sample microstructure can be described by the brick layer model (see *e.g.* Ref. 12). A uniform distribution of cubic grains (the bricks) with the grain boundaries in between (the cement) is assumed. By letting G and g denote the grain size (*i.e.* the length of the edge of the cube) and the grain boundary width, we readily obtain

$$\sigma_{gi} = \frac{1}{R_1}, \text{and } \sigma_{gb} = \frac{1}{R_2}\frac{g}{G}. \tag{50}$$

Here R_1 and R_2 denote the resistances associated to the first and second semicircle, respectively. Consequently, the diameter of the second semicircle is a function of microstructure (g/G) and the specific grain boundary conductivity. In order to calculate σ_{gb},

an assumption of equal permittivities in the grain interior and grain boundaries is made ($\varepsilon_{gi} = \varepsilon_{gb}$). A relation for g/G is then derived as C_1/C_2, and

$$\sigma_{gb} = \frac{1}{R_2}\frac{C_1}{C_2}. \qquad (51)$$

R is proportional to L/A, while C is proportional to A/L (A: area and L: length). Since $\omega_0 = (1/RC)$, it therefore follows that $\omega_0 = \sigma/\varepsilon$, implying that the characteristic frequencies of both the grain interior and the grain boundary semicircle are independent of sample size and microstructure. The exponential increase in conductivity with temperature, as compared to usually temperature independent permittivity, results in a rapid increase of ω_0 with temperature. At higher temperatures, the grain interior contribution is therefore seen as an offset along the real axis in the Nyquist plot.

As already stated, one advantage of impedance spectroscopy is the elimination of the need of reversible electrodes. The response from the electrodes to the sample's impedance is in many cases complex, and constitutes an important part of solid state electrochemistry as such. Here, we will limit ourselves to three comments. Firstly, the electrode impedance may consist of numerous individual contributions. Secondly, the characteristic frequencies of these contributions are usually much lower (and therefore the capacitances much higher) than that of the grain boundaries. Thirdly, fitting the electrode response to a simple (RQ) circuit will usually be sufficient when the goal is to extract parameters for grain interior and grain boundaries from the impedance spectra.

The experimentally obtained impedance spectra were fitted using the "Equivalent circuit for Windows" software [73]. Before fitting the data, the obtained data was validated by means of a Kramers-Kronig transformation test, as included in the software. This test returns a "quality of data" value (given in terms of χ^2). Typically, this value was in the order of 10^{-7}, reaching 10^{-6} for spectra recorded under more "difficult" conditions. According to the manual of the software, values below 10^{-6} indicate "quite good data". This test also helps in discarding unreasonable data points. The software uses a complex nonlinear least-squares regression technique when fitting the data, and outputs a value for the goodness of the fit (again in terms of χ^2). In Table 4.1, χ^2 from both the Kramers-Kronig transformation test and the fit of the data is given for a number of LNS0.5 samples under different conditions.

Table 4.1. χ^2 from the Kramers-Kronig (KK) transformation test compared with χ^2 from the fit of the data for four different samples with composition $La_{0.995}Sr_{0.005}NbO_4$. At 400 and 220 °C, data were fitted with an equivalent circuit consisting of four and three (RQ) sub-circuits, respectively. χ^2 is averaged from different measurements.

	400 °C		220 °C	
	KK	Fit	KK	Fit
Sample 1	$3.0 \cdot 10^{-7}$	$3.8 \cdot 10^{-6}$	$3.0 \cdot 10^{-6}$	$4.8 \cdot 10^{-5}$
Sample 2	$5.1 \cdot 10^{-7}$	$2.7 \cdot 10^{-6}$	$1.2 \cdot 10^{-5}$	$7.9 \cdot 10^{-5}$
Sample 3	$3.6 \cdot 10^{-7}$	$4.2 \cdot 10^{-6}$	$1.2 \cdot 10^{-5}$	$5.0 \cdot 10^{-5}$
Sample 4	$5.8 \cdot 10^{-7}$	$6.5 \cdot 10^{-6}$	$9.7 \cdot 10^{-6}$	$6.2 \cdot 10^{-5}$

At 220 °C, the rather large total sample impedance causes the data points from the recorded spectra to scatter more than those recorded at 400 °C. Typically, χ^2 from the fit of the data was an order of magnitude higher than that from KK.

References

[1] T. Takahashi, Journal of Applied Electrochemistry 3 (1973) 79.
[2] W. Hayes, Contemporary Physics 19 (1978) 469.
[3] N.M. Sammes, G.A. Tompsett, H. Näfe, F. Aldinger, Journal of the European Ceramic Society 19 (1999) 1801.
[4] V.V. Kharton, E.N. Naumovich, A.A. Yaremchenko, F.M.B. Marques, Journal of Solid State Electrochemistry 5 (2001) 160.
[5] A.I. Baranov, L.A. Shuvalov, N.M. Shchagina, JETP Letters 36 (1982) 459.
[6] T. Norby, M. Friesel, B.E. Mellander, Solid State Ionics 77 (1995) 105.
[7] X. Guo, J. Maier, Journal of the Electrochemical Society 148 (2001) E121.
[8] X. Guo, W. Sigle, J. Fleig, J. Maier, Solid State Ionics 154-155 (2002) 555.
[9] X. Guo, W. Sigle, J. Maier, Journal of the American Ceramic Society 86 (2003) 77.
[10] H.J. Avila-Paredes, K. Choi, C.-T. Chen, S. Kim, Journal of Materials Chemistry 19 (2009) 4837.
[11] H.J. Park, S. Kim, Journal of Physical Chemistry C 111 (2007) 14903.
[12] S.M. Haile, D.L. West, J. Campbell, Journal of Materials Research 13 (1998) 1576.
[13] A. Peters, C. Korte, D. Hesse, N. Zakharov, J. Janek, Solid State Ionics 178 (2007) 67.
[14] H.L. Tuller, Journal of Physics and Chemistry of Solids 55 (1994) 1393.
[15] L. Minervini, R.W. Grimes, K.E. Sickafus, Journal of the American Ceramic Society 83 (2000) 1873.
[16] J. Maier, *Physical Chemistry of Ionic Materials: Ions and Electrons in Solids*, Wiley, Chichester, 2004.
[17] T. Norby, M. Widerøe, R. Glöckner, Y. Larring, Dalton Transactions (2004) 3012.
[18] R. Haugsrud, T. Norby, Nature Materials 5 (2006) 193.
[19] R. Haugsrud, T. Norby, Solid State Ionics 177 (2006) 1129.
[20] T. Mokkelbost, I. Kaus, R. Haugsrud, T. Norby, T. Grande, M.A. Einarsrud, Journal of the American Ceramic Society 91 (2008) 879.
[21] H.A. Harwig, A.G. Gerards, Journal of Solid State Chemistry 26 (1978) 265.
[22] P.S. Manning, J.D. Sirman, R.A. De Souza, J.A. Kilner, Solid State Ionics 100 (1997) 1.
[23] A. Tschöpe, E. Sommer, R. Birringer, Solid State Ionics 139 (2001) 255.
[24] I. Denk, W. Münch, J. Maier, Journal of the American Ceramic Society 78 (1995) 3265.
[25] K.D. Kreuer, Solid State Ionics 125 (1999) 285.
[26] H.G. Bohn, T. Schober, Journal of the American Ceramic Society 83 (2000) 768.
[27] W. Münch, K.D. Kreuer, S. Adams, G. Seifert, J. Maier, Phase Transitions 68 (1999) 567.
[28] K. Amezawa, H. Maekawa, Y. Tomii, N. Yamamoto, Solid State Ionics 145 (2001) 233.
[29] T. Norby, N. Christiansen, Solid State Ionics 77 (1995) 240.
[30] R.F.G. Gardner, F. Sweett, D.W. Tanner, Journal of Physics and Chemistry of Solids 24 (1963) 1175.
[31] M.K. Nowotny, L.R. Sheppard, T. Bak, J. Nowotny, Journal of Physical Chemistry C 112 (2008) 5275.
[32] S. Steinsvik, *Electrical conductivity and defect structure in* $SrTi_{1-x}Fe_xO_{3-y}$, PhD thesis, University of Oslo, 1999.
[33] A. Magraso, R. Haugsrud, M. Segarra, T. Norby, Journal of Electroceramics 23 (2009) 80.
[34] H.L. Tuller, A.S. Nowick, Journal of Physics and Chemistry of Solids 38 (1977) 859.
[35] K.D. Kreuer, Chemistry of Materials 8 (1996) 610.
[36] J.E. Bauerle, J. Hrizo, Journal of Physics and Chemistry of Solids 30 (1969) 565.
[37] J.A. Kilner, C.D. Waters, Solid State Ionics (1982) 253.
[38] R. Gerhardt-Anderson, A.S. Nowick, Solid State Ionics 5 (1981) 547.
[39] J. Fleig, J. Maier, Journal of the American Ceramic Society 82 (1999) 3485.
[40] X. Guo, R. Waser, Progress in Materials Science 51 (2006) 151.
[41] J.-H. Lee, Monatshefte für Chemie 140 (2009) 1081.
[42] Y.-S. Jung, J.-H. Lee, J.-H. Lee, D.-Y. Kim, Journal of the Electrochemical Society 150 (2003) J49.
[43] H.J. Park, S. Kim, Solid State Ionics 179 (2008) 1329.
[44] X. Guo, J. Fleig, J. Maier, Solid State Ionics 154-155 (2002) 563.
[45] Z.L. Zhang, W. Sigle, R.A. De Souza, W. Kurtz, J. Maier, M. Ruhle, Acta Materialia 53 (2005) 5007.
[46] R.A. De Souza, Physical Chemistry Chemical Physics 11 (2009) 9939.
[47] S. Kim, J. Fleig, J. Maier, Physical Chemistry Chemical Physics 5 (2003) 2268.

[48] D.-W. Kim, D.-K. Kwon, S.H. Yoon, K.S. Hong, Journal of the American Ceramic Society 89 (2006) 3861.
[49] C. Korte, A. Peters, J. Janek, D. Hesse, N. Zakharov, Physical Chemistry Chemical Physics 10 (2008) 4623.
[50] N. Schichtel, C. Korte, D. Hesse, J. Janek, Physical Chemistry Chemical Physics 11 (2009) 3043.
[51] C. Korte, N. Schichtel, D. Hesse, J. Janek, Monatshefte für Chemie 140 (2009) 1069.
[52] J. Garcia-Barriocanal, A. Rivera-Calzada, M. Varela, Z. Sefrioui, E. Iborra, C. Leon, S.J. Pennycook, J. Santamaria, Science 321 (2008) 676.
[53] X. Guo, Science 324 (2009) 465.
[54] X.X. Guo, J. Maier, Advanced Materials 21 (2009) 2619.
[55] C.C. Liang, Journal of the Electrochemical Society 120 (1973) 1289.
[56] S. Kim, J. Maier, Journal of the Electrochemical Society 149 (2002) J73.
[57] N. Sata, K. Eberman, K. Eberl, J. Maier, Nature 408 (2000) 946.
[58] S. Kim, U. Anselmi-Tamburini, H.J. Park, M. Martin, Z.A. Munir, Advanced Materials 20 (2008) 556.
[59] S. Kim, H.J. Avila-Paredes, S.Z. Wang, C.T. Chen, R.A. De Souza, M. Martin, Z.A. Munir, Physical Chemistry Chemical Physics 11 (2009) 3035.
[60] H.J. Avila-Paredes, J.F. Zhao, S.Z. Wang, M. Pietrowski, R.A. De Souza, A. Reinholdt, Z.A. Munir, M. Martin, S. Kim, Journal of Materials Chemistry 20 (2010) 990.
[61] G. Chiodelli, F. Maglia, U. Anselmi-Tamburini, Z.A. Munir, Solid State Ionics 180 (2009) 297.
[62] D. Perez-Coll, G.C. Mather, Solid State Ionics 181 (2010) 20.
[63] W. Lai, S.M. Haile, Journal of the American Ceramic Society 88 (2005) 2979.
[64] J. Jamnik, J. Maier, Journal of the Electrochemical Society 146 (1999) 4183.
[65] J. Jamnik, J. Maier, Physical Chemistry Chemical Physics 3 (2001) 1668.
[66] J. Jamnik, X. Guo, J. Maier, Applied Physics Letters 82 (2003) 2820.
[67] W.C. Chueh, W. Lai, S.M. Haile, Solid State Ionics 179 (2008) 1036.
[68] J. Jamnik, Solid State Ionics 157 (2003) 19.
[69] T. Mokkelbost, Ø. Andersen, R.A. Strøm, K. Wiik, T. Grande, M.-A. Einarsrud, Journal of the American Ceramic Society 90 (2007) 3395.
[70] F.T. Miles, A.W.C. Menzies, Journal of the American Chemical Society 58 (1936) 1067.
[71] M.E. Orazem, B. Tribollet, *Electrochemical Impedance Spectroscopy*, Wiley, Hoboken, 2008.
[72] I.D. Raistrick, D.R. Franceschetti, J.R. Macdonald, in: *Impedance Spectroscopy: Theory, Experiment, and Applications*, Second Edition, E. Barsoukov, J.R. Macdonald (eds.), Wiley, Hoboken, 2005.
[73] B.A. Boukamp, Equivalent circuit for Windows Ver. 1.2, 2008.

PAPER I

Title: Proton mobility through a second order phase transition: theoretical and experimental study of $LaNbO_4$

Status: Published in Physical Chemistry Chemical Physics 12, 10313-10319 (2010)

Authors: Harald Fjeld, Kazuaki Toyoura, Reidar Haugsrud, and Truls Norby

Proton mobility through a second order phase transition: theoretical and experimental study of $LaNbO_4$

Harald Fjeld,* Kazuaki Toyoura,* Reidar Haugsrud and Truls Norby

Received 10th February 2010, Accepted 22nd May 2010
DOI: 10.1039/c002851g

The gradual change in the crystal structure of the high temperature proton conductor $LaNbO_4$ through a second order phase transition and its relation to the activation enthalpy of mobility of protons have been studied by means of first principles calculations and conductivity measurements. The computations have revealed that protons diffuse by an inter-tetrahedral mechanism where the activation enthalpies of mobility are 39 and 60 kJ mol^{-1} in tetragonal and monoclinic $LaNbO_4$, respectively. The activation enthalpy of mobility of protons for tetragonal $LaNbO_4$, determined from the conductivity curve, is 35 kJ mol^{-1}. Below the transition temperature the conductivity curve bends; initially dropping off steeply, followed by a less steep decrease towards lower temperatures. The bend in the conductivity curve at the onset of the phase transition in $LaNbO_4$ should not be given the traditional interpretation as an abrupt change in the activation enthalpy of mobility. After application of the proper analysis of the conductivity data, which takes the second order transition into account, the activation enthalpy of mobility of protons is found to continuously increase with increasing monoclinic angle at decreasing temperature, reaching $\sim$57 kJ mol^{-1} at 205 °C for the end monoclinic phase.

1. Introduction

Proton conducting oxides represent a class of functional materials with characteristics suitable for electrochemical energy converters, such as fuel cells.[1,2] To achieve high proton conductivity, which is the key factor for high performance of such devices, the material should exhibit both high concentration and mobility of protons. In proton conducting oxides, the protonic defects reside on oxygen sites as hydroxide ions and are formed when oxygen vacancies react with water, according to eqn (1):

$$H_2O(g) + V_O^{\bullet\bullet} + O_O^x = 2OH_O^{\bullet} \quad (1)$$

The concentration of protons is given by the thermodynamics of the reaction in eqn (1) and increases with increasing water vapour partial pressure, pH_2O. For oxides that contain any significant amount of protons the reaction is exothermic such that the concentration increases with decreasing temperature, T.

Protons migrate by activated diffusion, and the mobility, u_H, can be expressed according to an Arrhenius-type expression

$$u_H = u_{0,H}\frac{1}{T}\exp\left(-\frac{\Delta H_{mob,H}}{RT}\right) \quad (2)$$

where $u_{0,H}$ and $\Delta H_{mob,H}$ are, respectively, the pre-exponential term and the activation enthalpy of mobility of protons. According to previous papers on proton conducting oxides, $\Delta H_{mob,H}$ has a tendency to increase with decreasing crystal symmetry within perovskites.[1,3]

Recently, the rare earth ortho-niobates and ortho-tantalates were reported as a class of proton conductors.[4] $LaNbO_4$ has the highest proton conductivity in the class, and the conductivity of acceptor doped $LaNbO_4$ is predominantly protonic in wet reducing atmospheres up to $\sim$1100 °C.[5] This compound has two polymorphs, the low temperature monoclinic (m-$LaNbO_4$) and the high temperature tetragonal (t-$LaNbO_4$). The phase transition between these two modifications is of second order, and the transition temperature, T_{trs}, was reported to be in the range of 495–520 °C.[6–8] The monoclinic angle changes gradually from 90° to $\sim$94.1° as the temperature decreases from T_{trs} to room temperature.[9–11]

In the present study, the influence of the second order phase transition from tetragonal to monoclinic $LaNbO_4$ on the mobility of protons has been investigated using both theoretical and experimental approaches. First, the computational results on proton migration in the two extreme structures, *i.e.* the tetragonal phase and the monoclinic phase at 0 K, are shown. Next, the bulk proton conductivity in acceptor-doped $LaNbO_4$ as a function of temperature is shown as complementary data between the two extreme structures. We then present a proper procedure to analyze the conductivity behaviour through second order phase transitions, which is supported by the theoretical and experimental data. The procedure differs from commonly encountered approaches involving abrupt changes in activation energy, which in this case represent an unphysical model. Finally, the results are compared and discussed in light of recent findings on the proton conductivity mechanism in oxides with related structures.

Department of Chemistry, University of Oslo, FERMiO, Gaustadalléen 21, NO-0349 Oslo, Norway.
E-mail: haraldfj@kjemi.uio.no, k.toyoura0315@gmail.com

2. Computational procedures

First of all, it is necessary to determine stable proton sites in both tetragonal and monoclinic phases prior to finding proton migration paths. Initially, potential energy surfaces (PESs) of a proton were calculated with the host atomic positions fixed. Then, all the atomic positions were fully optimized for proton positions with low energies in the PESs. Finally, proton migration paths and their energy profiles were evaluated using the nudged elastic band (NEB) method.[12]

All the computational studies were based on first principles calculations, which were performed using the projector augmented wave (PAW) method implemented in the VASP code.[13] The local density approximation (LDA) parameterized by Perdew and Zunger[14] was used for the exchange–correlation term. The plane wave cutoff energy was 400 eV. The 5s, 5p, 6s, and 5d orbitals for lanthanum, 5s and 4d for niobium, 2s and 2p for oxygen, and 1s for hydrogen were treated as valence states. Two kinds of supercells consisting of $2 \times 2 \times 1$ tetragonal and monoclinic unit cells were used with a k-point grid of $2 \times 2 \times 2$. Grids for the potential energy surfaces of a proton include $20 \times 20 \times 40 = 16\,000$ points per unit cell. Atomic positions were optimized until the residual forces became less than 0.02 eV Å^{-1}. In studying proton mobility, 12 paths in t-$LaNbO_4$ and 10 paths in m-$LaNbO_4$ were considered.

3. Experimental methods

The reported results correspond to conductivity characterization of a sample of commercially provided $La_{0.995}Sr_{0.005}NbO_{4-\delta}$ powder (CerPoTech, Trondheim, Norway) conventionally sintered at 1200 °C, yielding a dense ceramic with average grain size of ~5 μm. Electrodes were painted onto polished surfaces of the sintered disk sample using Pt-paint (Metalor A3788A) and a Pt-mesh. The sample is identical to the one used for an earlier report,[15] in which more details can be found.

Impedance spectra were recorded in the frequency range 2 MHz – 4 mHz with a Novocontrol Alpha-A with ZG4 interface, using an oscillation voltage of 0.5 V (RMS). The sample was mounted in a measurement cell (ProboStat, NorECs, Norway) in which four Pt-wires were connected in pairs to the electrodes. For all measurements, gas was provided according to $pH_2O = 0.025$ atm, $pH_2 = 0.05$ atm, with Ar as balance. In this atmosphere and at the temperatures investigated here, the conductivity of acceptor-doped lanthanum niobate is essentially protonic as the contribution of oxide ions only amounts to ~2% of the total conductivity and electronic conductivity is negligible at 600 °C.[5]

As the aim of this study was to investigate the temperature dependency of the mobility of protons, a temperature range in which hydration of oxygen vacancies is relatively slow (frozen-in conditions) was chosen. It was observed that about one week was needed to obtain equilibrium upon hydration at 760 °C. Thus, during the rapid cooling of the sample in the interval 630–205 °C, the concentration of protons was assumed not to increase significantly. This assumption was supported by repeating the first measurement at 630 °C immediately after the cooling cycle. The increase in the bulk conductivity was ~2%, indicating that the proton concentration had increased ~2% during the cooling cycle. The conductivity data presented in this study therefore essentially reflect changes in the proton mobility only.

The impedance spectra were fitted, using the "Equivalent circuit for Windows" software,[16] to equivalent circuits consisting of sub-circuits of resistors (R_i) and constant phase elements (Q_i) in parallel, denoted as (R_iQ_i). Explicitly, the circuits used were $R_1(R_2Q_2)(R_3Q_3)(R_4Q_4)$, $(R_1Q_1)(R_2Q_2)(R_3Q_3)(R_4Q_4)$ and $(R_1Q_1)(R_2Q_2)(R_3Q_3)$ for temperatures in the ranges 630–540 °C, 530–350 °C, and 340–205 °C, respectively. For $T \leq 530$ °C, the geometrical capacitance of the (R_1Q_1) sub-circuit was calculated to 2–3 pF cm^{-1}, which reflects values typical for bulk. Hence, the bulk conductivity, σ_{bulk}, could be calculated by inversion of R_1. Additionally, R_2 and R_3 were assigned to grain boundary related processes and R_4 to electrode related processes. For more details concerning the fitting of the impedance spectra of acceptor doped $LaNbO_4$, consult ref. 14.

4. Results and discussion

4.1 Crystal structures of tetragonal and monoclinic $LaNbO_4$

Fig. 1 shows the calculated crystal structures of tetragonal and monoclinic $LaNbO_4$. For easy structural comparison between the two polymorphs, space group $I4_1/a$ was employed for t-$LaNbO_4$ and $I2/c$ for m-$LaNbO_4$. The direction along the c axis is called "out-of-plane direction", and regions within a plane perpendicular to the c axis are called "in-plane" hereafter. The calculated and experimental lattice parameters are shown in Table 1. The differences between the calculated and experimental lattice parameters are within 3%. Note that our calculated lattice parameters cannot be directly compared with the reported room temperature values of m-$LaNbO_4$, as the computational results correspond to parameters at 0 K. The key symmetry difference between the two phases is the out-of-plane 4-fold screw axis in t-$LaNbO_4$ as compared to the corresponding 2-fold axis in m-$LaNbO_4$. As a result, all the cation layers are equivalent with equal interlayer distances in t-$LaNbO_4$, whereas they are divided into two kinds of cation layers in m-$LaNbO_4$. Especially, niobium ions are considerably displaced in m-$LaNbO_4$, which leads to alternating interlayer distances of niobium as shown in the figure. In addition, oxygen sites are divided into O1 and O2 sites. In the following, we will see that the differences of the stable proton sites and migration behaviour between the two phases are strongly related to this structural difference.

4.2 Stable sites of protons

Generally, protons in oxides reside around oxide ions to form an O–H bond, and $LaNbO_4$ is no exception. In t-$LaNbO_4$, there is just one crystallographic oxygen site, and two stable proton sites were found per oxygen site. These sites are shown in Fig. 2, where all the other atomic positions are shown using those before the structural optimization. The most stable proton site is called an a site, which is near the neighbouring tetrahedron. The other, on the opposite side, is called a b site, and is found between two lanthanum ions. The energy of the b site is 0.13 eV (13 kJ mol^{-1}) higher than that of the a site.

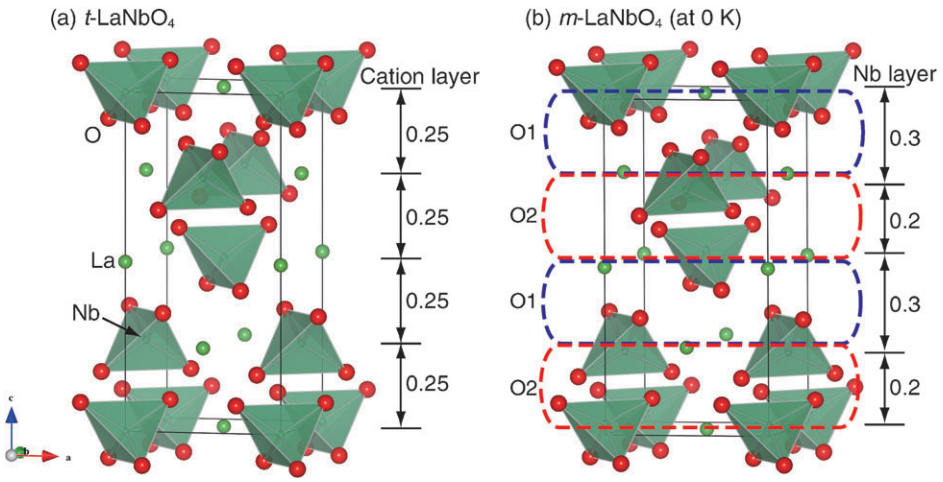

Fig. 1 Calculated crystal structures of (a) tetragonal and (b) monoclinic (at 0 K) $LaNbO_4$. The tetrahedra consist of niobium ions coordinated by four oxide ions. Red and green balls denote oxide and lanthanum ions, respectively.

Table 1 Calculated lattice parameters of tetragonal and monoclinic $LaNbO_4$. Values in parentheses denote the experimental values reported in ref. 11

		a	*b*	*c*	*β*
t-$LaNbO_4$	Compt. (this work)	5.35		11.32	
	Exp.[a] (at 600 °C)	(5.40)		(11.69)	
m-$LaNbO_4$	Compt. (this work)	5.54	5.13	11.29	95.5°
	Exp.[a] (at 20 °C)	(5.57)	(5.20)	(11.53)	(94.1°)

[a] Ref. 11

Both O–H bond lengths are 1.0 Å, which is approximately equal to that in water. Each O–H bond is directed towards another oxide ion, and has a first-nearest-neighbour equivalent stable site in that direction. The lengths between the proton and the other oxide ion are 1.5 Å for the *a* site and 1.7 Å for the *b* site.

By contrast to t-$LaNbO_4$, m-$LaNbO_4$ has two types of oxygen sites. There are two stable proton sites around the O1 ions, which are similar to those in t-$LaNbO_4$. The most stable proton site, a', is close to the neighbouring tetrahedron, whereas the b' site on the opposite side has an energy 0.41 eV (40 kJ mol^{-1}) higher than the a' site. The third most stable proton site, c', is found around O2 ions. The energy of the c' site is 0.77 eV (74 kJ mol^{-1}) higher than that of the a' site. The lengths of these three O–H bonds are again 1.0 Å. Note that protons prefer the region around the O1 ions and that there are no stable proton sites between the two adjacent O2 layers. This suggests that out-of-plane migration of protons is difficult in m-$LaNbO_4$.

4.3 Proton migration paths and energy profiles

It is now possible to search for proton migration paths in $LaNbO_4$ by connecting the identified stable sites. In t-$LaNbO_4$, 12 paths were evaluated, including several inter- and intra-tetrahedron paths. The four paths with the lowest potential barriers are shown schematically in Fig. 3(a). The path having the lowest potential barrier is between two adjacent *a* sites (path 1). A proton goes through an inversion centre between the initial and final *a* sites. The potential barrier is 0.04 eV (4 kJ mol^{-1}). The path with the next lowest barrier is between two adjacent *b* sites (path 2) with a potential barrier of 0.06 eV (6 kJ mol^{-1}). The potential barriers of paths 1 and 2 are comparable to the thermal energy (0.04–0.08 eV in our experimental temperature range), so that protons rapidly shift positions between adjacent *a*–*a* and *b*–*b* sites, so-called "oscillatory proton transfer".[17]

An additional migration path connecting *a* and *b* sites is necessary for long-distance proton migration. Path 3, which

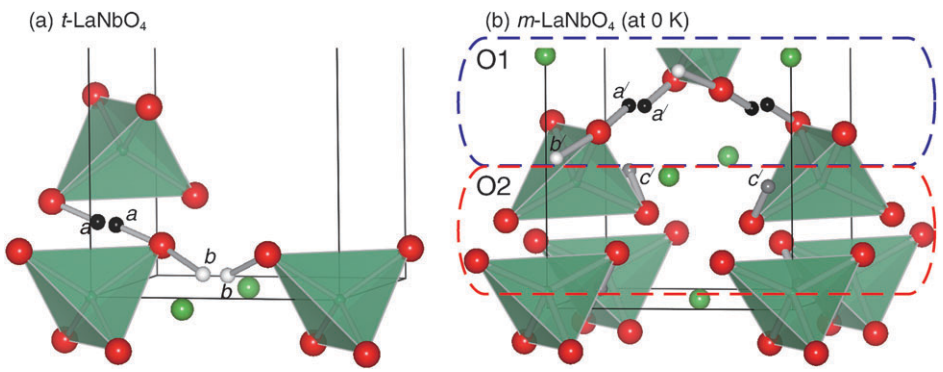

Fig. 2 Calculated stable sites of a proton in (a) tetragonal and (b) monoclinic (at 0 K) $LaNbO_4$. Black, white, and gray balls denote *a* and a', *b* and b', and c' sites, respectively.

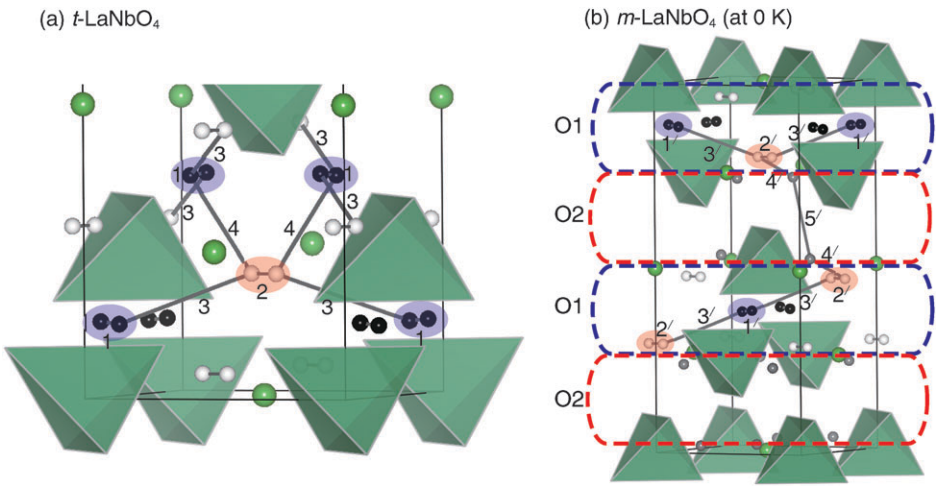

Fig. 3 Proton migration paths with low potential barriers in (a) tetragonal and (b) monoclinic (at 0 K) $LaNbO_4$. Paths 1–4 are in the tetragonal phase, while paths 1′–5′ are in the monoclinic. Paths with same numbers in the different phases are similar to each other.

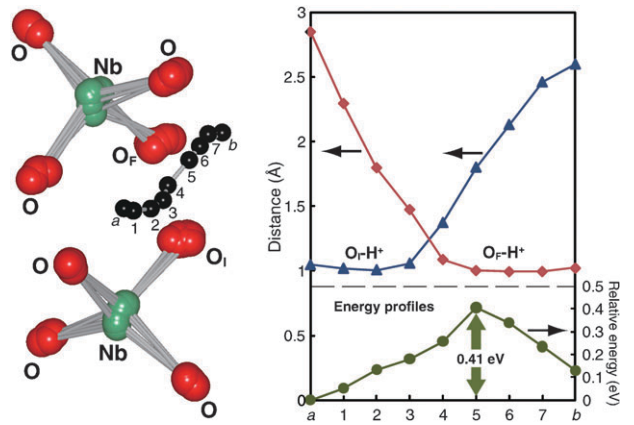

Fig. 4 The images and the energy profile of path 3 from *a* site to *b* site with structural relaxation around the migrating proton. The distances between the migrating proton and the two oxide ions close to the initial and final proton sites (O_I and O_F) are also shown in the figure.

has the third lowest potential barrier, 0.41 eV (39 kJ mol^{-1}), enables such *a* to *b* migration within the plane and is shown in Fig. 4 with the corresponding energy profile. The distances between the migrating proton and the two oxide ions close to the initial and final proton sites (O_I and O_F ions, respectively) are also shown. The distance between the proton and O_I ion is around 1 Å for the first 4 positions, similar to the distance from the O_F ion to the proton of the final 4 positions. This means that the proton rotates around the oxide ions before and after it jumps between the two tetrahedrons. This kind of migration, *i.e.* rotation and hopping, has been found computationally in other proton conducting oxides, such as $BaCeO_3$ and $BaZrO_3$.[18,19] Since path 3 is sufficient for long-range proton transport, this path is the rate-determining process for in-plane proton migration. For the out-of-plane proton migration, path 4 is required to connect two layers. The potential barrier of path 4 is 0.74 eV (72 kJ mol^{-1}), which is almost twice that of path 3. This means that t-$LaNbO_4$ has a large anisotropy of proton conduction.

In m-$LaNbO_4$, the region around the O1 ions is similar to that in t-$LaNbO_4$. Paths 1′, 2′, and 3′ were found in the O1 region, and they are similar to paths 1, 2, and 3, respectively, in t-$LaNbO_4$ (refer to Fig. 3(b)). The corresponding potential barriers are 0.04 eV (4 kJ mol^{-1}), 0.17 eV (16 kJ mol^{-1}), and 0.62 eV (60 kJ mol^{-1}). Path 3′ is the rate-determining step of the in-plane migration in m-$LaNbO_4$, and the potential barrier is 0.21 eV (21 kJ mol^{-1}) higher than for t-$LaNbO_4$. For the out-of-plane long-range migration, several paths through *c* sites should be considered additionally. Paths 4′ and 5′ were found as reasonable paths connecting two adjacent layers. These potential barriers are quite high, 0.94 eV (91 kJ mol^{-1}) and 1.55 eV (150 kJ mol^{-1}), respectively, with reference to the energy at the *a*′ site. The anisotropy in proton conduction in m-$LaNbO_4$ is therefore much higher than in t-$LaNbO_4$.

4.4 Mobility of protons in $LaNbO_4$

In the previous sections, the two extreme cases corresponding to t-$LaNbO_4$ and m-$LaNbO_4$ at 0 K have been focused on. Now, we will provide complementary proton transport data covering the temperature range in which the structure of m-$LaNbO_4$ is gradually changing and eventually results in t-$LaNbO_4$. Fig. 5 shows the temperature dependence of the bulk conductivity of protons, σ_{bulk}. Above ~520 °C, corresponding to T_{trs}, $LaNbO_4$ is tetragonal and the slope of a $\log(\sigma_{bulk}T)$ *vs.* $1/T$ plot is constant (Arrhenius-type behaviour), as emphasised in the inset of Fig. 5. Below T_{trs} the monoclinic phase region is entered; the conductivity curve bends, initially drops off more steeply and then decreases less steeply towards lower temperatures. The curve is however all the way continuous, consistent with the displacive nature of the phase transition that results in a gradual change in the lattice parameters of m-$LaNbO_4$ with temperature.

It is illustrative to contrast the case of $LaNbO_4$ with a phase transition of first order. For a first order phase transition, a discontinuous change in the crystal structure at T_{trs} would be expected, resulting in a change of stable proton sites and migration paths. This, in turn, would be observed as a

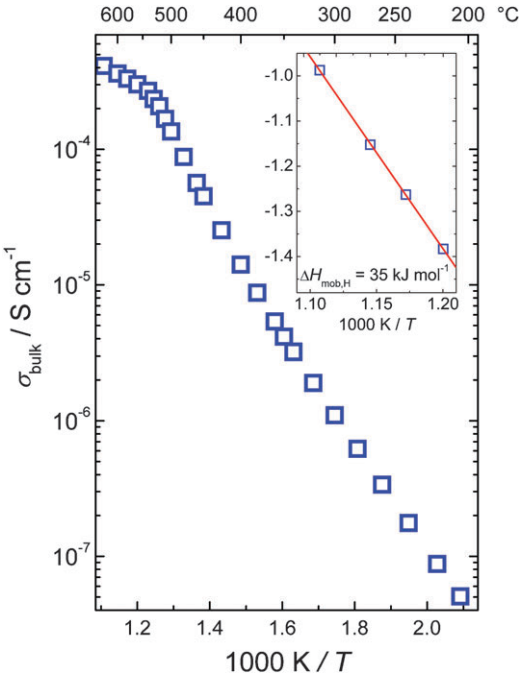

Fig. 5 σ_{bulk} of 0.5% Sr-doped $LaNbO_4$ *vs.* inverse temperature. The inset shows the Arrhenius plot of the conductivity at temperatures where $LaNbO_4$ is tetragonal. The conductivity data are obtained under conditions where the concentration of protons is constant.

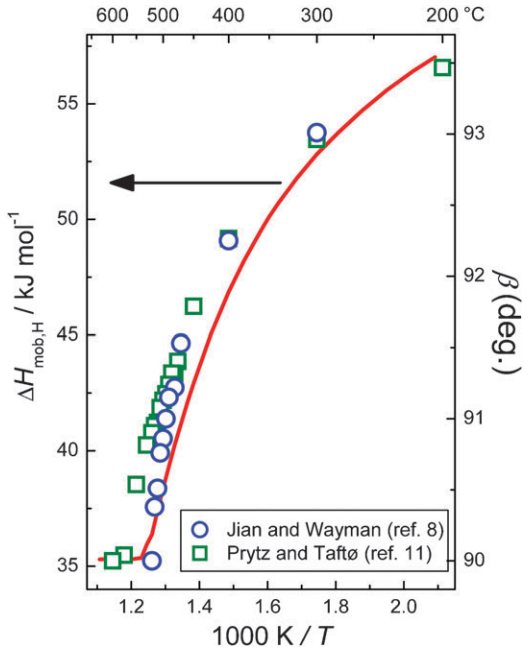

Fig. 6 The activation enthalpy of mobility of protons (line, left) and reported values of β (squares, circles, right) *vs.* inverse temperature.

discontinuity in the Arrhenius plot with linear behaviour on each side of T_{trs}, in stark contrast to Fig. 5.

From the inset in Fig. 5, $\Delta H_{mob,H}$ and $u_{0,H}$ of t-$LaNbO_4$ were estimated to 35 kJ mol^{-1} and 5 cm^2 K V^{-1} s^{-1}, respectively, the latter by assuming that $[OH_O^{\bullet}] = 0.93[Sr'_{La}]$, which was calculated from reported thermodynamic parameters at 630 °C.[5] The experimental value for $\Delta H_{mob,H}$ is in good agreement with the computational in-plane value of 39 kJ mol^{-1}. While the pre-exponential $u_{0,H}$ may vary through the phase transition, the variation is expectedly minor, and will have a minor effect on the conductivity compared to a change in the activation enthalpy of mobility. As a first approximation for modelling the data we thus assume that $u_{0,H}$ remains constant and the same in both t- and m-$LaNbO_4$. (This assumption is indeed supported by the computational findings, in that the proton conductivity is predominated by the similar in-plane migration mechanism in both polymorphs.) $\Delta H_{mob,H}$ was subsequently calculated as a function of temperature according to $\Delta H_{mob,H} = RT(\ln \sigma_0 - \ln \sigma_{bulk}T)$ where σ_0 is the pre-exponential term of the conductivity which was determined from the inset of Fig. 5. $\Delta H_{mob,H}$ is presented as a function of temperature in Fig. 6 together with reported values for the monoclinic angle.[8,11] It is seen that $\Delta H_{mob,H}$ increases steadily with decreasing temperature as the crystal structure of $LaNbO_4$ becomes more distorted from the relatively symmetrical tetragonal one. Also for m-$LaNbO_4$ the agreement between the computational and experimental techniques is satisfactory; we see that $\Delta H_{mob,H}$ approaches 57 kJ mol^{-1}, in good agreement with the value of 60 kJ mol^{-1} calculated at 0 K. The similar temperature dependencies of $\Delta H_{mob,H}$ and β suggest a correlation between $\Delta H_{mob,H}$ and the degree of distortion of the crystal structure.

The experimentally obtained values for $\Delta H_{mob,H}$ agree well with the computational in-plane values. In a polycrystalline sample, the experimentally determined conductivity is averaged by random grain orientation. The conductivity along the c axis is in our case expected to be much smaller than the in-plane conductivity due to the much larger $\Delta H_{mob,H}$ for the out-of-plane migration. This means that the effective $\Delta H_{mob,H}$ will be essentially equal to the in-plane value of $\Delta H_{mob,H}$.

One commonly meets the view that the steep slope of the Arrhenius plot just below the phase transition directly reflects a high activation energy of the monoclinic phase. From that view it follows that temperature dependent values of $\Delta H_{mob,H}$ can be directly calculated from the slope of the Arrhenius plot, *i.e.* $\Delta H_{mob,H}$ is equal to the apparent activation energy. However, such an approach is not correct because the slope does not correspond to $\Delta H_{mob,H}$ when $\Delta H_{mob,H}$ itself is a function of temperature. By differentiating the Arrhenius expression one readily obtains eqn (3):

$$\frac{\mathrm{d}(\ln \sigma T)}{\mathrm{d}\left(\frac{1}{T}\right)} = -\frac{1}{R}\left(\Delta H_{mob,H}(T) + \frac{\mathrm{d}(\Delta H_{mob,H}(T))}{\mathrm{d}\left(\frac{1}{T}\right)}\frac{1}{T}\right)$$
$$= -\frac{1}{R}\left(\Delta H_{mob,H}(T) - \frac{\mathrm{d}(\Delta H_{mob,H}(T))}{\mathrm{d}T}T\right) \quad (3)$$

In addition to $\Delta H_{mob,H}$ itself, an additional term, $\mathrm{d}(\Delta H_{mob,H}(T))/\mathrm{d}(1/T)(1/T)$, appears in the expression of the slope. In our case this term is positive, and it, therefore, follows that the slope is greater than $\Delta H_{mob,H}$. Furthermore, since the change in β and thus $\mathrm{d}(\Delta H_{mob,H}(T))/\mathrm{d}(1/T)$ are largest when the monoclinic phase region is entered, the slope in the Arrhenius plot is also largest here. By way of example, the erroneous approach would in our case have resulted

in an abrupt increase of $\Delta H_{mob,H}$ with decreasing temperature when the monoclinic phase region is entered, yielding $\Delta H_{mob,H} \approx 120$ kJ mol^{-1} around T_{trs}. Such high values for $\Delta H_{mob,H}$ also lead to erroneously high values for $u_{0,H}$. (Calculations just below T_{trs} would have given values of $u_{0,H}$ up to $\sim 10^6$ cm^2 K V^{-1} s^{-1}.)

It should also be emphasised that a model where the charge carrying protons are gradually trapped by the acceptors (here Sr'_{La}) fails to explain the main features of the conductivity curve seen in Fig. 5. If such a model would have applied, the apparent activation energy should smoothly increase with decreasing temperature, because association reactions are necessarily exothermic. However, the slope in Fig. 5 drastically changes around 520 °C and, moreover, the plot curves upwards with decreasing temperature. Both tendencies are in disagreement of the association model.

From the discussion above, only a gradual change in $\Delta H_{mob,H}$ with temperature, and thereby structure, satisfactorily explains the conductivity data in Fig. 5. As a measure of the degree of distortion in the structure, the monoclinic angle can be employed. Since the phase transition from t-$LaNbO_4$ to m-$LaNbO_4$ is a second order phase transition, we can use the order parameter, $\Gamma = \left(\frac{T_{trs}-T}{T_{trs}}\right)^{1/2}$, on the basis of Landau theory, and the reported values of β[8] are fitted to obtain the following equation for β as a function of temperature:

$$\beta = \beta_0 + k\Gamma = 90^\circ + 5.41^\circ\left(\frac{520 - T/^\circ\mathrm{C}}{520}\right)^{1/2} \qquad (4)$$

With this analytical expression for β as a function of temperature, $\Delta H_{mob,H}$ is plotted as a function of β in Fig. 7. We observe that the change in $\Delta H_{mob,H}$ increases with increasing β until a seemingly steady change is reached at higher angles. Although the change in β is rather small, the impact on $\Delta H_{mob,H}$ is considerable. As our computational results show, the cation layers in m-$LaNbO_4$ have different interlayer distances and there are two different oxygen sites. It is therefore not surprising that such a change in the crystal structure with changing temperature significantly influences the proton mobility.

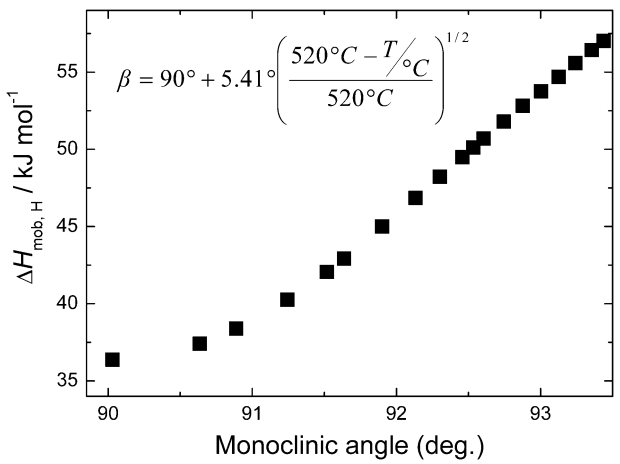

Fig. 7 The activation enthalpy of mobility of protons plotted as a function of the monoclinic angle of $LaNbO_4$. By using data for 21–520 °C reported by Jian and Wayman[8] and T_{trs} = 520 °C, an analytical equation (inset in figure) for β as a function of temperature was obtained with a correlation of 0.996.

For various monazite-type structured rare earth and other orthophosphates the monoclinic angle has been reported to be almost constant as a function of temperature.[20] It is therefore interesting to note that no bend in the proton conductivity curve similar to that of $LaNbO_4$ (Fig. 5) is reported for the chemical analogues $LaPO_4$,[21,22] $LaAsO_4$[23] or $LaVO_4$[24] (all monazite-type structured), or for orthorhombic $LaTaO_4$ ($BaMnF_4$-type structure).[25] Oppositely, for fergusonite-type structured $NdNbO_4$, $GdNbO_4$ and $TbNbO_4$, where the monoclinic angle changes with temperature, a similar bend is indeed observed in the conductivity curves.[4]

According to our calculations, the rate-determining process for migration of protons in $LaNbO_4$ is the rotation and hopping between two adjacent tetrahedra, so-called inter-tetrahedral proton transfer. This is similar to what Yu and De Jonghe[17] reported for monazite-type structured $LaPO_4$, which has a similar, but not identical, crystal structure compared to $LaNbO_4$. $LaBaGaO_4$ is another proton conducting oxide where oxide ions are tetrahedrally coordinated to cations (in this case Ga^{3+}). Using the DFT NEB method, Kendrick *et al.*[26] reported that for $LaBaGaO_4$ the activation energies for inter-tetrahedral proton migration were much smaller than that of the intra-tetrahedral. Furthermore, the authors suggested that the rate-determining step for the long-range proton diffusion was related to the intra-tetrahedron process. On this basis, the rate-determining step in $LaBaGaO_4$ is different to what is suggested for $LaNbO_4$ and $LaPO_4$. Consequently, this indicates that in

Table 2 Some crystallographic and transport properties (both experimentally and computationally determined values) of some proton conducting oxides. All perovskites are 10% Y-doped

				$\Delta H_{mob,H}$ / kJ mol^{-1}	
Oxygen Coordination	Compound	Crystal system	Structure type	Experimental	Computational
Tetrahedral	$LaNbO_4$	Tetragonal	Scheelite	35 (this work), 55[aj]	39 (this work)
	$LaNbO_4$	Monoclinic	Fergusonite	35–57 (this work)	60 (this work)
	$LaVO_4$	Monoclinic	Monazite	75[bj]	
	$LaPO_4$	Monoclinic	Monazite	77–82[ck]	77[d]
Octahedral	$BaZrO_3$	Cubic	Perovskite	41–42[e]	20[f], 80[g]
	$BaCeO_3$	Orthorhombic	Perovskite	48–52[h]	47[g]
	$SrCeO_3$	Orthorhombic	Perovskite	61[i]	

[a] Ref. 4 [b] Ref. 24 [c] Ref. 21 and 22 [d] Ref. 17 [e] Ref. 3 and 27 [f] Ref. 28 [g] Ref. 29 [h] Ref. 30–32 [i] Ref. 30 [j] 1% Ca-doped [k] 5% Ca- or Sr-doped

$LaNbO_4$ and $LaPO_4$, protons may diffuse solely through an inter-tetrahedral process, while for $LaBaGaO_4$, the intra-tetrahedral step is necessary to have long-range proton transport.

Finally, it is useful to compare trends for reported values of $\Delta H_{mob,H}$ within tetrahedrally and octahedrally coordinated high temperature proton conductors with emphasis on crystal structure. Table 2 summarizes selected literature data for structurally and chemically comparable proton conductors and it is seen that $\Delta H_{mob,H}$ seems to increase (and the proton mobility thus decrease) with decreasing degree of symmetry also within the tetrahedrally coordinated proton conductors.

5. Conclusions

Using the DFT NEB method, we identified similar in-plane migration paths for long-range proton transport in the two polymorphs of $LaNbO_4$. Protons diffuse by an inter-tetrahedral mechanism within the cation layers. The activation enthalpy of mobility of protons was computationally determined to 39 and 60 kJ mol^{-1} in tetragonal and monoclinic $LaNbO_4$, respectively. For out-of-plane migration of protons, the potential barriers are high, 72 kJ mol^{-1} in the tetragonal and 150 kJ mol^{-1} in the monoclinic polymorph. Proton transfer has large anisotropy in both polymorphs of $LaNbO_4$.

The temperature dependence of the bulk proton conductivity rendered two clearly distinguishable regimes; the slope of $\log(\sigma_{bulk}T)$ *vs.* $1/T$ was constant in the tetragonal region, whereas the conductivity deviated from Arrhenius-type behaviour in the monoclinic. After application of the proper analysis of the conductivity data, which take the second order phase transition into account, it was found that the activation enthalpy of mobility of protons increases with decreasing temperature from $\sim$35 kJ mol^{-1} for the tetragonal polymorph to $\sim$57 kJ mol^{-1} for the monoclinic polymorph at 205 °C; thus in agreement with the computational findings.

Second order phase transitions are rather common in materials science. We therefore point out the importance of the proper approach when extracting transport parameters from conductivity data. In the opposite case, conductivity data similar to what have been shown here are easily misinterpreted.

Acknowledgements

One of the authors (K.T.) wishes to thank "Canon foundation in Europe" for financial support during the stay in Oslo.

References

1 K. D. Kreuer, *Annu. Rev. Mater. Res.*, 2003, **33**, 333–359.
2 R. Haugsrud, in *Handbook of Fuel Cells*, ed. W. Vielstich, H. Yokokawa and H. A. Gasteiger, Wiley, Chichester, 2009, vol. 5, part 3, pp. 505–516.
3 K. D. Kreuer, *Solid State Ionics*, 1999, **125**, 285–302.
4 R. Haugsrud and T. Norby, *Nat. Mater.*, 2006, **5**, 193–196.
5 R. Haugsrud and T. Norby, *Solid State Ionics*, 2006, **177**, 1129–1135.
6 V. S. Stubican, *J. Am. Ceram. Soc.*, 1964, **47**, 55–58.
7 W. I. F. David, *Mater. Res. Bull.*, 1983, **18**, 749–756.
8 L. Jian and C. M. Wayman, *J. Am. Ceram. Soc.*, 1997, **80**, 803–806.
9 L. N. Kinzhibalo, V. K. Trunov and V. G. Krongauz, *Kristallografiya*, 1982, **27**, 43–48.
10 S. Tsunekawa, T. Kamiyama, K. Sasaki, H. Asano and T. Fukuda, *Acta Crystallogr., Sect. A: Found. Crystallogr.*, 1993, **49**, 595–600.
11 Ø. Prytz and J. Taftø, *Acta Mater.*, 2004, **53**, 297–302.
12 G. Henkelman, B. P. Uberuaga and H. Jónsson, *J. Chem. Phys.*, 2000, **113**, 9901–9904.
13 P. E. Blöchl, *Phys. Rev. B: Condens. Matter*, 1994, **50**, 17953–17979.
14 J. P. Perdew and A. Zunger, *Phys. Rev. B: Condens. Matter*, 1981, **23**, 5048–5079.
15 H. Fjeld, D. M. Kepaptsoglou, R. Haugsrud and T. Norby, *Solid State Ionics*, 2010, **181**, 104–109.
16 B. A. Boukamp, *Equivalent circuit for Windows Ver. 1.2*, University of Twente/WisseQ, 2008.
17 R. Yu and L. C. De Jonghe, *J. Phys. Chem. C*, 2007, **111**, 11003–11007.
18 W. Münch, G. Seifert, K. D. Kreuer and J. Maier, *Solid State Ionics*, 1996, **86–88**, 647–652.
19 W. Münch, G. Seifert, K. D. Kreuer and J. Maier, *Solid State Ionics*, 1997, **97**, 39–44.
20 $CePO_4$, $NdPO_4$, $PuPO_4$, $CaTh(PO_4)_2$: R. Jardin, C. C. Pavel, P. E. Raison, D. Bouëxière, H. Santa-Cruz, R. J. M. Konings and K. Popa, *J. Nucl. Mater.*, 2008, **378**, 167–171; $LaPO_4$: B. C. Chakoumakos, personal communication.
21 K. Amezawa, H. Maekawa, Y. Tomii and N. Yamamoto, *Solid State Ionics*, 2001, **145**, 233–240.
22 T. Norby and N. Christiansen, *Solid State Ionics*, 1995, **77**, 240–243.
23 T. Bjørheim, unpublished work.
24 M. Huse, R. Haugsrud and T. Norby, unpublished work.
25 R. Haugsrud and T. Norby, *J. Am. Ceram. Soc.*, 2007, **90**, 1116–1121.
26 E. Kendrick, J. Kendrick, K. S. Knight, M. S. Islam and P. R. Slater, *Nat. Mater.*, 2007, **6**, 871–875.
27 H. G. Bohn and T. Schober, *J. Am. Ceram. Soc.*, 2000, **83**, 768–772.
28 P. G. Sundell, M. E. Björketun and G. Wahnström, *Phys. Rev. B: Condens. Matter Mater. Phys.*, 2007, **76**, 094301-1–094301-7.
29 W. Münch, K. D. Kreuer, G. Seifert and J. Maier, *Solid State Ionics*, 2000, **136–137**, 183–189.
30 W. Münch, K. D. Kreuer, S. Adams, G. Seifert and J. Maier, *Phase Transitions*, 1999, **68**, 567–586.
31 N. Bonanos, B. Ellis, K. S. Knight and M. N. Mahmood, *Solid State Ionics*, 1989, **35**, 179–188.
32 K. D. Kreuer, W. Münch, M. Ise, T. He, A. Fuchs, U. Traub and J. Maier, *Ber. Bunsen-Ges. Phys. Chem.*, 1997, **101**, 1344–1350.

PAPER II

Title: Space-charge theory applied to the grain boundary impedance of proton conducting $BaZr_{0.9}Y_{0.1}O_{3-\delta}$

Status: Published in Solid State Ionics, 181, 268-275 (2010)

Authors: Christian Kjølseth, Harald Fjeld, Øystein Prytz, Paul Inge Dahl, Claude Estournès, Reidar Haugsrud, Truls Norby

This article is removed from the thesis.

PAPER III

Title: Charge carriers in grain boundaries of 0.5% Sr-doped $LaNbO_4$

Status: Published in Solid State Ionics, 181, 104-109 (2010).

Authors: Harald Fjeld, Despoina Maria Kepaptsoglou, Reidar Haugsrud and Truls Norby

This article is removed from the thesis.

PAPER IV

Title: Proton and oxide ion conductivity in grain boundaries and grain interior of Ca-doped $Er_2Ti_2O_7$ with Si-impurities

Status: Published in Solid State Ionics, 179, 1849-1853 (2008).

Authors: Harald Fjeld, Reidar Haugsrud, Anette Eleonora Gunnæs and Truls Norby

This article is removed from the thesis.

MANUSCRIPT A

Title: Chemical polarization induced by grain boundaries in a mixed oxide ion and proton conductor: A study of Ca-doped $Er_2Ti_2O_7$

Chemical polarization induced by grain boundaries in a mixed oxide ion and proton conductor: A study of Ca-doped $Er_2Ti_2O_7$

Harald Fjeld

Department of Chemistry, University of Oslo, FERMiO, Gaustadalléen 21, NO-0349 Oslo, Norway

The electrical properties of ceramics of $(Er_{1-x}Ca_x)_2Ti_2O_{7-x}$ (x = 0.02 and 0.005) with low and high contents of Si impurities at the grain boundaries were investigated by impedance spectroscopy as a function of pO_2, pH_2O and pD_2O in the temperature range 300–800 °C. For the grain interior, oxygen vacancies are the major charge carrier, with protons as a minor contributor at the lower temperatures. In the grain boundaries – as compared to grain interior – the singly charged protons were relatively more predominating than the doubly charged oxygen vacancies, suggesting that negatively charged space-charge layers govern the electrical properties. In support of this, the samples with a lower content of Si in the grain boundaries exhibited an electrical response essentially similar to those containing more Si and even a secondary Si-rich phase. An additional impedance – the third in the Nyquist plots – was suggested to be caused by chemical polarization of the mixed oxide ion and proton conducting grain interiors induced by blocking of oxygen vacancies at the grain boundaries. The discussion of chemical polarization induced by grain boundaries constitutes the major part of this contribution.

1. Introduction

Solid metal oxides can transport both ionic and electronic charge carriers. In a polycrystalline sample, both grain interior and grain boundaries must be taken into account, as the transport characteristics of the relevant charge carriers can be strongly dependent on location. By way of example, oxide ions and electron holes both contribute to the grain interior conductivity in weakly acceptor doped $SrTiO_3$, while the grain boundary conductivity is dominated by electron holes [1,2].

In a previous contribution we reported the electrical properties of $Er_{1.96}Ca_{0.04}Ti_2O_{6.98}$ [3]. Oxide ions were identified as the major charge carrier in the grain interiors. In the grain boundaries, it was concluded that protons were important charge carriers. This was concluded from impedance spectroscopy as a function of temperature, pO_2, pH_2O, and pD_2O. The samples in that investigation contained an amorphous Si and Ca enriched phase at triple grain junctions and along grain boundaries. Based on the microstructural and electrical investigations we proposed three hypotheses to account for the unusual transport properties:

1) The amorphous siliceous phase present at the grain boundaries was a proton conductor. This was supported by reports of proton conductivity at high temperatures in silicates such as $Ca(SiO_4)O$ [4] and $La_2Si_2O_7$ [5].

2) If grain interior contained both protons and oxygen vacancies, negatively charged space-charge layers adjacent to a positively charged grain boundary core (see *e.g.* Ref. 6) would lead to a quadratic depletion of doubly charged oxygen vacancies as compared to singly charged protons. Consequently, the ratio of the concentration of protons and oxygen vacancies was higher in the grain boundaries than in the grain interior. A relatively higher concentration of protons in the grain boundaries than in grain interior therefore enabled a change from oxygen vacancies to protons as the major charge carrier.

3) A combination of 1 and 2.

We briefly discussed the appearance of two arcs in the impedance spectra with capacitances in the "grain boundary range", and speculated that the second grain boundary arc could be related to the chemical capacitance associated to the coupling between the current flow rails for oxygen vacancies and protons. The concept of chemical capacitance has previously been applied on mixed ionic and electronic conductors, such as $SrTiO_3$ [7,8] and CeO_2 [9,10]. A DC voltage applied on a mixed ionic and electronic conductor using electrodes that are blocking for either the ionic or electronic charge carrier will induce compositional variations within the mixed conductor, which we in the following term as chemical polarization. In AC impedance spectroscopy, the feature related to chemical polarization will manifest itself as a half tear-drop shape when the concentration and the mobility of the charge carriers are comparable. This half tear-drop shape is similar to the finite length Warburg element. However, when the difference in the concentrations of the charge carriers becomes larger, the tear-drop shape will transform into a semicircular shape [11,12].

The chemical capacitance of a material can be interpreted as the material's ability to store chemical energy in terms of changes in composition. Taking a mixed ionic and electronic conductor as an example, during polarization the concentration of oxygen as a function of position in the sample becomes non-uniform and changes with time. The change in the oxygen content here requires ambipolar diffusion of oxide ions (*e.g.* by oxygen vacancies) and electrons, emphasising that the ability to store chemical energy is strongly linked to the ambipolar diffusion. The polarization can be accomplished by means of selectively blocking electrodes, or by grain boundaries that exhibit different transport numbers than the grain interior [7].

In this study we aim to analyse in more detail the unusual electrical behaviour of the $Er_2Ti_2O_7$-based samples by applying theory of chemical polarization induced by grain boundaries. This will then as we see it provide a first application of this theory to a mixed proton and oxide ion conductor. We have prepared a matrix of samples where the acceptor dopant concentration and the content of Si vary. Impedance spectroscopy as a function of DC bias has been included to provide further insight into the various processes that are taking place in these ceramics.

2. Experimental

2.1 Sample preparation

Powders of nominal composition $(Er_{1-x}Ca_x)_2Ti_2O_{7-x}$ (ETC, x = 2% and 0.5%) were prepared using Er_2O_3 (either Molycorp, 98% (Ho main impurity) or Alfa Aesar, 99.95%), $CaCO_3$ (Sigma-Aldrich, 99.95%) and TiO_2 (Alfa Aesar, 99.5%) as precursors. In order to elucidate the role of Si on the electrical properties, we wanted to compare samples with a "low" and "high" content of Si. Thus, a matrix of four samples, abbreviated as ETC2 and ETC0.5 (with low Si-contents) and ETC2Si[1] and ETC0.5Si (with high Si-contents) was synthesized, as explained below.

In light of our previous investigation [3], the presence of rather large amounts of Si at the grain boundaries may be a result of the powder preparation where a strong acidic solution was used to dissolve the alkaline cations. The samples with high contents of Si were therefore synthesized by firstly dissolving Er_2O_3 and $CaCO_3$ in hot dilute nitric acid in a borosilicate beaker. Citric acid was then added as complexing agent, and after decomposition the viscous solution was heated to 700–750 °C to remove the organic compounds. TiO_2 was then added. Wet ball milling and over night calcination were repeated twice with a final calcination at $T \leq 1000$ °C. Dense samples (more than 90% of theoretical density) were obtained by uniaxially pressing green disks of 25 mm diameter followed by sintering at 1500 °C.

Samples with a low Si-content were synthesised by wet-milling the precursors in isopropanol. The ball milling was followed by calcination over night and the cycle was repeated twice up to 1000 °C. Then the green disks were sintered at 1500 °C, resulting in too porous samples. Consequently, the

[1] ETC2Si is identical to the sample reported in Ref. 3.

samples were crushed and the resulting powder was ball milled before sintering at 1620 °C, yielding dense samples (more than 90% of theoretical density).

2.2 Characterisation of crystal structure and microstructure

The crystal structure of the samples was investigated at room temperature in air by X-ray powder diffraction using a Siemens D5000 diffractometer with $CuK\alpha_1$ radiation. The microstructure was examined by scanning electron microscopy (Quanta 200F, FEI), and the samples ETC2, ETC2Si and ETC0.5 were additionally investigated by transmission electron microscopy (JEOL2010F). Chemical composition was determined with the energy dispersive x-rays spectroscopy (EDS) unit of each electron microscope.

2.3 Electrical measurements

Prior to the electrical measurements, the surfaces of the sintered samples were ground using SiC paper followed by painting of circular Pt-electrodes (Metalor A3788A paint + Pt-mesh) on each side of the pellet. Then the samples were mounted in a measurement cell (Probostat, NorECs) in which Pt-wires were connected to the two electrodes. The measurement cell was inserted into a vertical tube furnace, and the electrical properties were investigated in the temperature range 300 – 800 °C. The gas atmosphere in the measurement cell was controlled by using an in-house-built gas mixer as described elsewhere [13]. To obtain different oxygen partial pressures, O_2 (or 5% H_2 in Ar) were diluted with Ar. pH_2O (and pD_2O) were controlled by passing the gas through H_2O (and D_2O) saturated with KBr.

The impedance measurements were performed under equilibrium conditions using a Solartron 1260 FRA or a Novocontrol alpha-A impedance analyzer in the frequency range 2 MHz–50 μHz. An oscillation voltage of 0.5 V (RMS) was normally used, but other oscillation voltages were occasionally applied for probing possible effects on the recorded spectra. For one sample (ETC2), impedance spectra were recorded as a function of applied DC bias up to 3.5 V. These measurements were performed with the Novocontrol alpha A analyzer in a V1 DC coupling mode. The impedance spectra were fitted into equivalent circuits consisting of resistors and constant phase elements using the “Equivalent circuit for Windows” software [14].

3. Results and Discussion

3.1 Crystal structure and microstructure

The XRD patterns of ETC2, ETC2Si and ETC0.5 after sintering could be indexed according to the cubic pyrochlore structure of $Er_2Ti_2O_7$. For ETC0.5Si, however, some additional reflexes were observed. After subsequent grinding of this sample, these reflexes could no longer be observed in the diffractogram, suggesting that a secondary phase was enriched at the surface of the sample.

Fig. 1 shows scanning electron microscopy (SEM) micrographs of ETC0.5Si as-sintered and after the surface was ground.

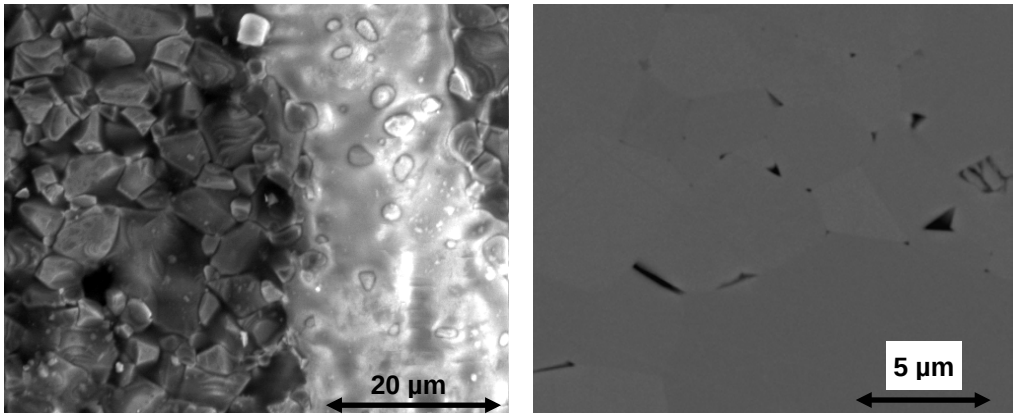

Fig. 1. SEM micrographs of ETC0.5Si. Left: As-sintered, secondary electron detector. Right: Ground and polished surface, back-scattered electron detector. Darker regions correspond to a secondary phase rich in Si.

Relatively large amounts of a glassy-like secondary phase rich in Si (from SEM-EDS) were observed on the as-sintered surface. Also in the SEM micrographs of the polished sample a Si containing secondary phase was detected, here mostly located at triple grain junctions.

Fig. 2 shows transmission electron microscopy (TEM) micrographs of ETC2.

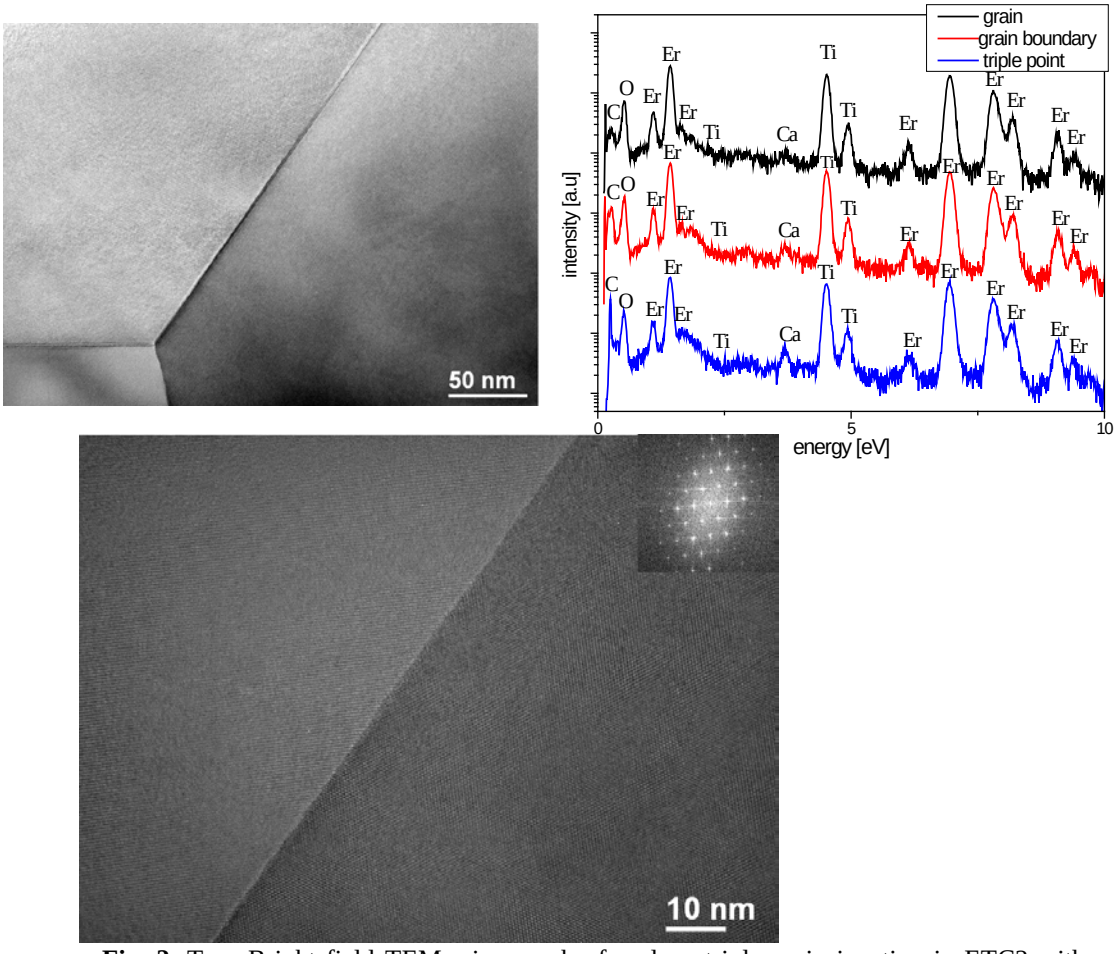

Fig. 2. Top: Bright field TEM micrograph of a clean triple grain junction in ETC2 with corresponding EDS spectra. Bottom: High resolution TEM image of a grain boundary in ETC2; the right grain is oriented close to the [110] zone axis (see inset fast Fourier transform).

The investigated grain boundaries appeared to be sharp and with no secondary phases, consistent with the EDS analyses (also shown in Fig. 2). This is in contrast with what we observed for ETC2Si where an amorphous Si and Ca rich phase was present at many of the triple grain junctions and along the grain boundaries [3].

A preliminary TEM investigation on ETC0.5 indicated mainly clean grain boundaries. A crystalline secondary phase, enriched in Er and Si, was, however, observed in one triple grain junction. Based on the different synthesis route of this sample and on the results of the TEM investigation we believe that this sample has a lower Si-content than ETC0.5Si.

3.2 Electrical measurements

In general, the AC electrical response of all samples contained four contributions with different relaxation times, seen as four arcs in a Nyquist plot (Fig. 3A). In a Bode plot (Fig. 3B) transition regions between two contributions appear as plateaus; thus three plateaus are observed in our case.

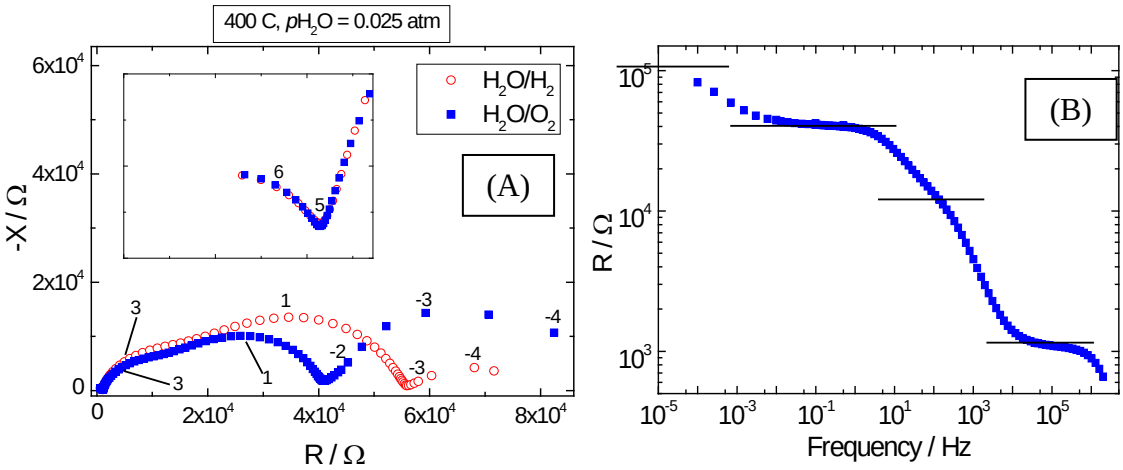

Fig. 3. A: Impedance spectra of ETC2 plotted in a Nyquist plot. Numbers indicate log frequency. The inset shows the high-frequency arc, arc 1. B: Impedance spectrum of ETC2 at 400 °C in H_2O/O_2. Lines indicate the plateaus which represent the transition between two processes with different relaxation times.

The arcs are numbered from 1 to 4, starting with number 1 at the highest frequencies (seen in the inset of Fig. 3A). Each arc was fitted to an equivalent circuit consisting of a resistor and a constant phase element (CPE) in parallel. When the relaxation time of an arc was within or close to the experimentally recorded frequency range, the corresponding geometrical capacitance (in which sample thickness and electrode area is taken into account) was calculated from $C = Y^{1/n}R^{(1-n)/n}$. Here, R is the resistance of the resistor and Y and n define the admittance of the CPE according to $Y_{CPE} = Y(j\omega)^n$ where $j = \sqrt{-1}$ and ω = angular frequency. The geometrical capacitances of the four contributions are shown in Fig. 4 as a function of temperature for all samples.

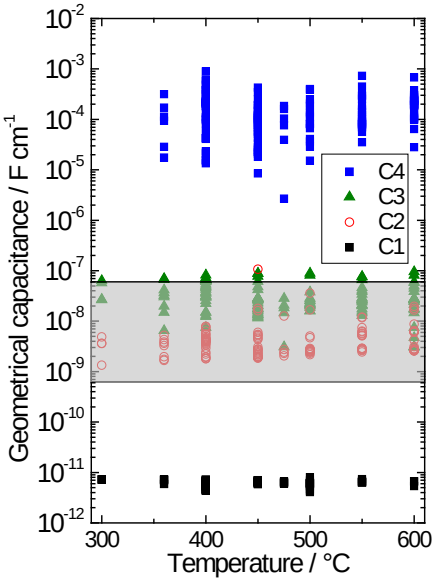

Fig. 4. Calculated geometrical capacitance of the different contributions from the impedance spectra as a function of temperature. The figure includes data from all samples. Shaded area indicates the expected geometrical grain boundary capacitance varying the grain size to grain boundary thickness ratio from (10 µm/1 nm) to (1 µm/10 nm) under the assumption of equal dielectric permittivity in grain interior and grain boundaries.

The average of C_1 was calculated to ~ 6 pF cm^{-1} corresponding to a dielectric constant of ~ 70, in agreement with a reported value of 61 [15]. We therefore conclude that the high frequency contribution refers to dielectric relaxation of grain interior. Furthermore, it is seen that C_2 and C_3 both fall within a capacitance region (shaded area of Fig. 4) characteristic of transport across grain boundaries. Such an interpretation is sound on basis of geometrical considerations (see figure caption) and provided that the dielectric constant of the grain boundary region is equal to that of grain interior. We will at a later stage in this paper discuss whether C_2 and/or C_3 really are related to transport across grain boundaries. Finally, it is plausible to assume that C_4 refers to electrode related processes as $C_4 > 10^{-5}$ F cm^{-1}.

For all investigated samples it was found that the resistance associated with the second and third relaxation time constants were dependent on pH_2O and the hydrogen isotope in a similar manner as shown earlier, in Ref. 3. It is interesting to note that the samples which have a lower content of Si in the grain boundaries (ETC2 and ETC0.5) exhibit an electrical response essentially similar to those containing a secondary phase (ETC0.5Si and ETC2Si). This indicates that the electrical response does not originate from the presence of an additional phase in the grain boundaries, but rather is an inherent property of Ca-doped $Er_2Ti_2O_7$. This strengthens hypothesis 2; negatively charged space-charge layers deplete the doubly charged oxygen vacancies more than the singly charged protons, resulting in effectively proton conducting grain boundaries.

We will in the following discuss the possibility of chemical polarization induced by the grain boundaries and its influence on the electrical response for Ca-doped $Er_2Ti_2O_7$. First of all, in order to observe a contribution related to chemical polarization, the material must be able to change its composition inside the grains. In the case of Ca-doped $Er_2Ti_2O_7$, we are dealing with mixed oxide ion and protonic conduction, and the oxide must therefore be able to change its content of H_2O. In

other words, grain interior should exhibit some protonic conductivity, in addition to that of the oxide ions. Hydration of oxygen vacancies is usually an exothermic process, and the concentration of grain interior protons will then increase with decreasing temperature. It is therefore expected that possible grain interior proton conductivity will appear at lower temperatures. The effects of $p\mathrm{H_2O}$ and hydrogen isotope on the grain interior conductivity σ_{gi} are shown in Fig. 5.

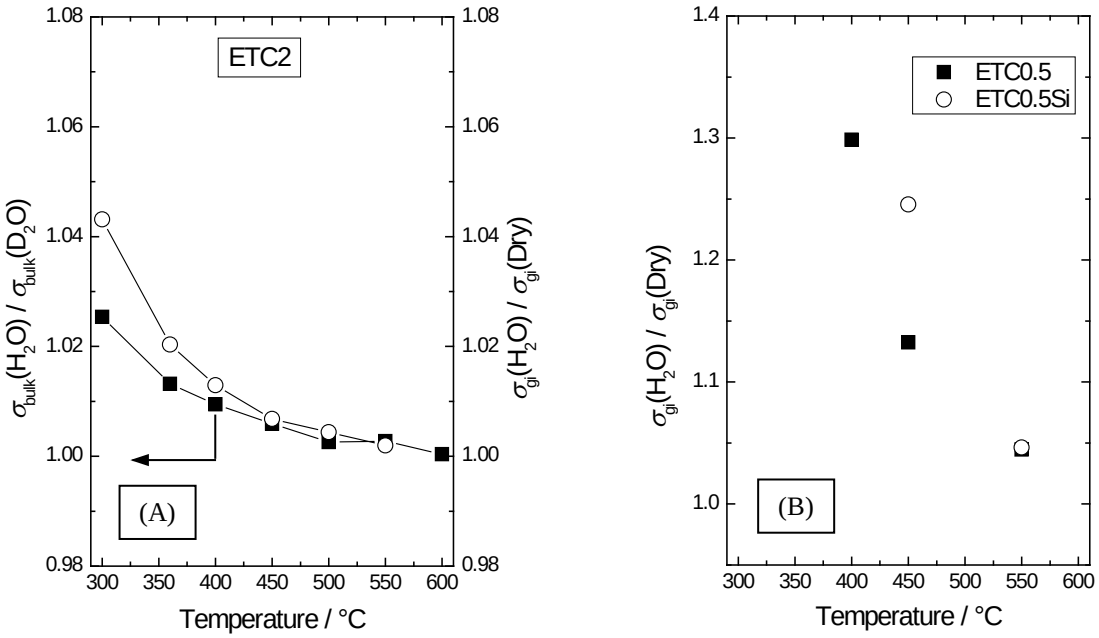

Fig. 5. A: Ratio of grain interior conductivity recorded in $\mathrm{H_2O/O_2}$ to grain interior conductivity in $\mathrm{D_2O/O_2}$ (l. h. s., closed squares) and to dry $\mathrm{O_2}$ (r. h. s., open circles) for ETC2. B: Ratio of grain interior conductivity recorded in $\mathrm{H_2O/O_2}$ to grain interior conductivity in dry $\mathrm{O_2}$ for ETC0.5 and ETC0.5Si.

For ETC2 (Fig. 5A) and ETC2Si (not shown here), a moderate isotope effect ($\sigma_{\mathrm{gi}}(\mathrm{H_2O})/\ \sigma_{\mathrm{gi}}(\mathrm{D_2O})$) as well as a slight increase in grain interior conductivity with increasing $p\mathrm{H_2O}$ were encountered, and both effects increased with decreasing temperature. For ETC0.5 and ETC0.5Si, the increase in the grain interior conductivity upon increasing $p\mathrm{H_2O}$ was larger (Fig. 5B). Hence, the results suggest that protons are present in grain interior at the lower temperatures, and that their concentration and conductivity both are low, but significant.

The total capacitance of a parallel connection is the inverse of the sum of the inverse partial capacitances. Assuming that the flow rails for the oxygen vacancies and the protons are in parallel, the total chemical capacitance, C_{chem}, is thus [16]

$$C_{\mathrm{chem}} = \frac{e^2}{k_{\mathrm{B}}T} AL\left(\frac{1}{z_{\mathrm{O}}^2 c_{\mathrm{O}}} + \frac{1}{z_{\mathrm{H}}^2 c_{\mathrm{H}}}\right)^{-1}. \qquad (1)$$

Here, z and c denote the charge number and the concentration of the oxygen vacancies and protons (subscript O and H, respectively). It is evident that C_{chem} is determined by the charge carrier with the lowest concentration. In our case, this is expectedly the protons and an increase in the proton concentration, *e.g.* by an increase in $p\mathrm{H_2O}$, should therefore give a higher C_{chem}. Plots of $\mathrm{C_2}$ and $\mathrm{C_3}$

as a function of pH_2O are shown in Fig. 6, and it is seen that C_2 decreases slightly with pH_2O whereas C_3 increases with increasing pH_2O.

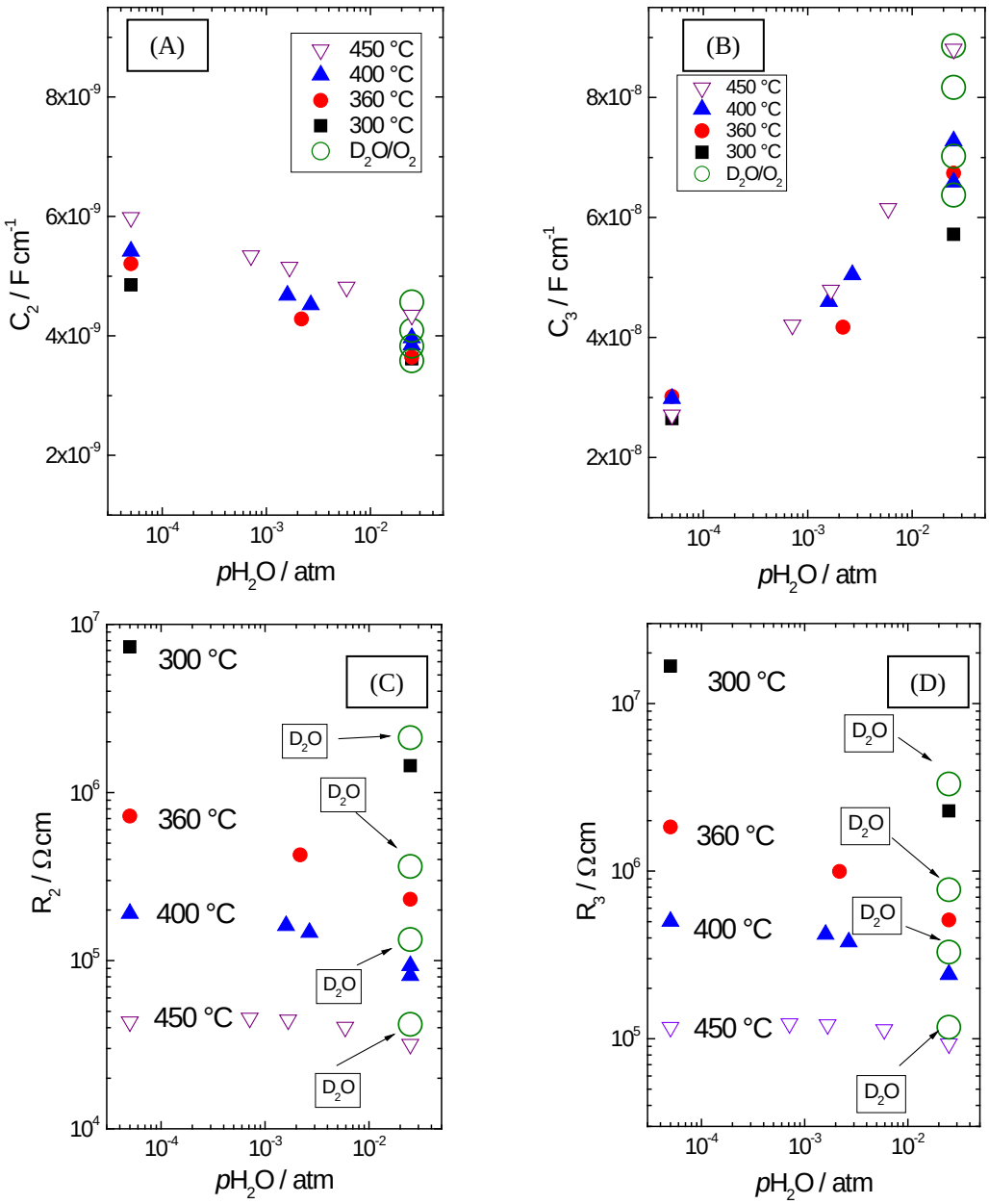

Fig. 6. Capacitance of arc 2 and 3 (C_2 and C_3) and resistance of arc 2 and 3 (R_2 and R_3) as a function of water vapour pressure in oxidising atmosphere (pO_2 ~ 1 atm) extracted from impedance spectra recorded from 300 to 450 °C. Measurements in D_2O/O_2 (pD_2O = 0.025 atm) are also included.

A temperature independent slope of log C_2 vs. log pH_2O was evaluated from Fig. 6A to approximately -0.05(1), while the slope of log C_3 vs. log pH_2O (Fig. 6B) increased with temperature, from 0.12 at 300 °C to 0.19 at 450 °C. Hence, the positive water vapour dependence of C_3 is in agreement with what we qualitatively expect of C_{chem}.

The above analysis was based on the capacitances which were extracted from the fitting of the impedance spectra in which parallel circuits of resistors and constant phase elements were used. If

chemical polarization really takes place, C_{chem} can not, however, be directly extracted from the impedance data on basis of such an approach because the contribution related to this is described with different mathematics. Indeed, a mediocre fit of the impedance data was encountered when using (RQ) circuits, especially in the frequency range covered by arcs 2 and 3. This is emphasised in Fig. 7, where the real and imaginary residuals of a spectrum fitted into four (RQ) sub-circuits are shown and compared with the errors obtained when only fitting the high frequency part.

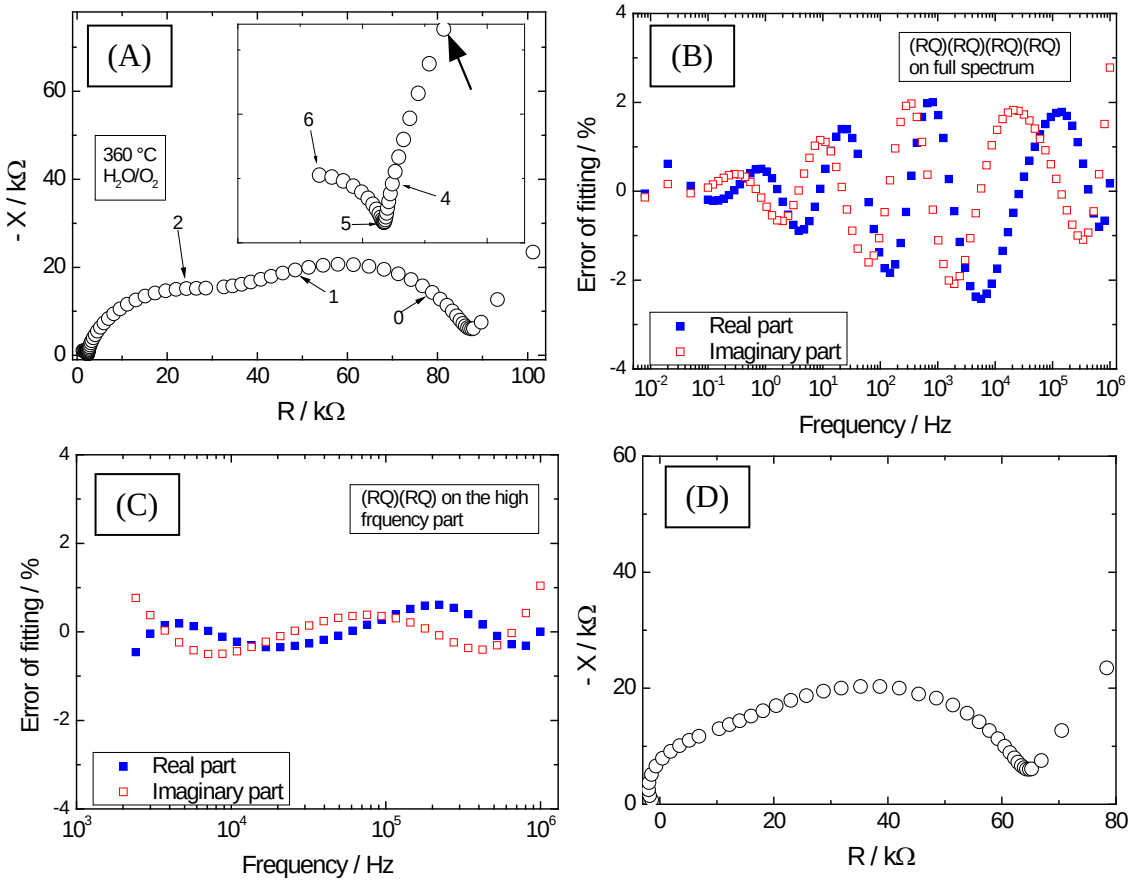

Fig. 7. A: Impedance spectrum of ETC2 in H_2O/O_2 (pH_2O = 0.025 atm) at 360 °C. Inset shows the high frequency part. Numbers indicate log frequency. B: Residual errors of the real and imaginary part of the spectrum shown in A when fitted into an equivalent circuit consisting of four (RQ) sub-circuits plotted as a function of log frequency. The rather large errors indicate a systematically error in the fitting of the impedance data. C: Residual errors when fitting only the high frequency part (the lower frequency is given in inset of A with a large arrow) into two (RQ) sub-circuits. D: The remaining impedance spectrum after subtraction of the fitted data in C, resembling a tear-drop shape.

We clearly see that the errors are smaller when we only fit the high frequency part. This indicates that arc 3 is not correctly accounted for by a simple (RQ) circuit. Moreover, after subtracting the fitted high frequency part from the spectrum displayed in Fig. 7A, the remaining spectrum (Fig. 7D) displays a tear-drop shape, similar to what is expected of a chemical polarization feature.

In general, tear drop shapes were observed in the residual spectra after subtraction of $(R_1Q_1)(R_2Q_2)$ from impedance spectra recorded at low temperatures and/or at high pH_2O. However, with increasing temperature or decreasing pH_2O, the remaining spectrum gradually transformed into a

semicircular shape. This is consistent with the concurrent decreasing concentration of protons which transforms $Er_2Ti_2O_7$ into essentially a pure oxide ion conductor.

According to Jamnik [17], a simplified expression for the relaxation time τ_0 ($\tau_0 = 1/\omega_0$, where ω_0 is the characteristic frequency, *i.e.* the frequency at the apex) of the chemical polarization feature evolves if the grain boundaries are completely blocking for one of the charge carriers. In our case, dealing with mixed oxide ion and proton conductivity, the relaxation time then reads [17]

$$\tau_0 = \left(R_{gi}^{O} + R_{gi}^{H}\right) C_{chem} . \qquad (2)$$

If we decrease pH_2O, the grain interior proton resistivity R_{gi}^{H} should increase on the account of a decrease in the proton concentration while C_{chem} should decrease (cf. Eq. 1), in total resulting in an expected small change in the relaxation time. If we instead change the atmosphere from H_2O/O_2 to D_2O/O_2, R_{gi}^{H} should increase, while C_{chem} should remain constant as the concentrations of the charge carriers are unchanged. Hence, the relaxation time should increase when shifting from H to D, *i.e.* the characteristic frequency should decrease – at least to a larger extent than when changing pH_2O. Impedance spectra in H_2O/O_2 (pH_2O = 0.025 and 0.0016 atm) and D_2O/O_2 (pD_2O = 0.025 atm) recorded at 400 °C are compared in Fig. 8.

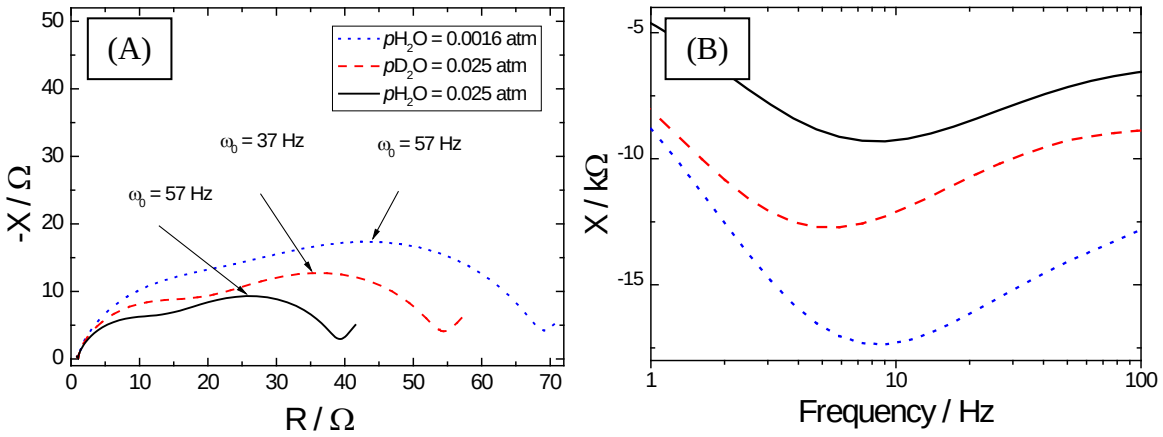

Fig. 8. A: Impedance spectra of ETC2 under oxidising conditions at 400 °C. pH_2O (or pD_2O) is given in legend. Please note that the spectra are chosen to be similar in total resistance. Characteristic frequencies ($\omega_0 = 2\pi f_0$, where f_0 is the peak frequency) of arc 3 are indicated. B: The imaginary part as a function of frequency, emphasising that the characteristic frequencies of arc 3 coincide at pH_2O = 0.025 and 0.0016 atm, in contrast to in D_2O/O_2.

It is seen that ω_0 of arc 3 remains essentially constant when pH_2O is decreased and that ω_0 shifts towards lower frequencies upon exchanging the hydrogen isotope from H to D. Both observations are in agreement with the expected trends of the relaxation time for a chemical polarization feature, strengthening our assumption that arc 3 is related to chemical polarization.

As discussed above, when only fitting the high frequency part of the impedance spectra into two (RQ) circuits, the residual errors decreased (Fig. 7). From this approach, the pH_2O dependency of C_2 was calculated to ~ -0.01 in a log-log plot, less steep than the slope of ~ -0.05 obtained upon fitting

the full spectra into four (RQ) circuits. We therefore believe that the capacitance of arc 2 inherently displays a rather low pH_2O dependency – consistent with relaxation of grain boundaries – and that the slope of ~ -0.05 observed in Fig. 9A is a result of fitting the spectra into an incorrect model.

The pH_2O dependency of R_2 extracted from the fitting of the impedance spectra by the high frequency approach is plotted in Fig. 9, and it is seen that R_2 increases with decreasing pH_2O.

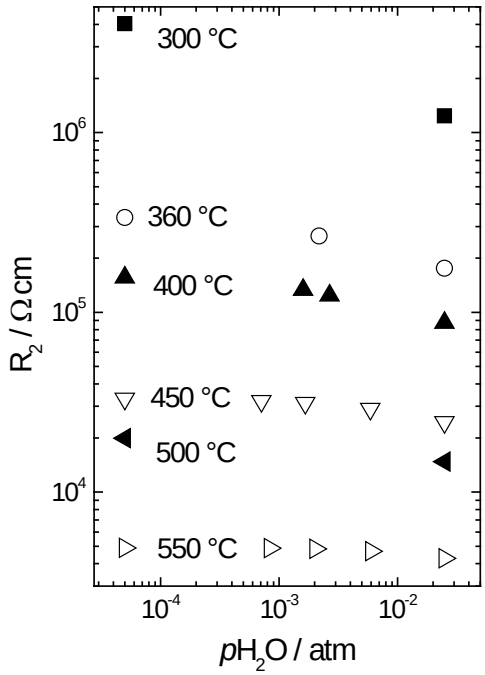

Fig. 9. The resistance of arc 2 as a function of water vapour pressure under oxidising conditions for ETC2. R_2 was extracted from the impedance spectra from a fitting approach in which only the high frequency part of the spectra were fitted into $(R_1Q_1)(R_2Q_2)$ or $R_1(R_2Q_2)$.

The water vapour dependency decreases with increasing temperature, consistent with the dehydration of the grain boundaries with increasing temperature. The higher functional pH_2O dependency of R_2 compared to R_1 can be explained if we assign R_2 to the resistance of the space-charge layers adjacent to the grain boundary core. Since the oxygen vacancies are doubly charged their depletion will be quadratic compared to the singly charged protons in the space-charge layers adjacent to a positively charged grain boundary core. This makes the role of the protons as charge carriers in the space-charge layers more prominent and R_2 more dependent on pH_2O. This behaviour is similar to what is encountered for acceptor doped $LaNbO_4$ [18].

As indicated in Eq. 2, the chemical capacitance can be experimentally determined from the impedance spectra provided that the grain boundaries are fully blocking towards oxygen vacancies. In order to get estimates for R_{gi}^{O} and R_{gi}^{H}, we assumed that the ratio of proton to deuteron conductivity is equal to $\sqrt{2}$, and used the grain interior parameters extracted from the spectra recorded in H_2O/O_2 and D_2O/O_2. The characteristic frequencies for arc 3 were read from the impedance spectra recorded in H_2O/O_2 after subtracting $(R_1Q_1)(R_2Q_2)$, as discussed above. Finally, $C_{chem,exp}$ was determined from Eq. 2 and values from 300 to 400 °C are given in Table 1.

It is now interesting to compare the experimentally determined values ($C_{\mathrm{chem,exp}}$) with calculations through Eq. 1. In order to address this, we need estimates for the concentration of protons c_{H}. To extract c_{H} from the available conductivity data is not straightforward since σ_{gi} is rather insensitive towards changes in $p\mathrm{H_2O}$ (cf. Fig. 5). Thus, another indirect approach was chosen. We assumed that the pre-exponential terms of mobility of protons and oxygen vacancies are equal ($u_{0,\mathrm{H}} = u_{0,\mathrm{O}}$) and that the activation enthalpy of mobility of protons is equal to 2/3 of the activation enthalpy of mobility of oxygen vacancies ($\Delta H_{\mathrm{mob,H}} = 2/3\ \Delta H_{\mathrm{mob,O}}$). Furthermore, $\Delta H_{\mathrm{mob,O}}$ was calculated to be 79 kJ mol^{-1} from the temperature dependency of σ_{gi} in dry $\mathrm{O_2}$. Using this, the ratios of proton mobility to oxygen vacancy mobility, $u_{\mathrm{H}}/u_{\mathrm{O}}$, could be calculated and are given in Table 2. Finally, by means of $\sigma_{\mathrm{gi,H}}$ and $\sigma_{\mathrm{gi,O}}$, the ratios of oxygen vacancy concentration to proton concentration were determined from the relation

$$\frac{c_{\mathrm{O}}}{c_{\mathrm{H}}} = \frac{\sigma_{\mathrm{gi,O}}}{\sigma_{\mathrm{gi,H}}} \frac{u_{\mathrm{H}}}{u_{\mathrm{O}}} \frac{1}{2}. \tag{3}$$

When selectively blocking electrodes induce compositional changes of the sample as a whole, the electrode area (A) and the sample thickness (L) represent the relevant geometrical parameters. In our case, we suspect that the grain boundaries induce changes in the composition within the grains. Using the experimentally determined average grain size G, the chemical capacitance of an average cubic grain is equal to (*cf.* Eq. 1)

$$\bar{C}^{\ \mathrm{grain}}_{\mathrm{chem}} = \frac{e^2}{k_{\mathrm{B}}T} G^3 \left(\frac{1}{z_{\mathrm{O}}^2 c_{\mathrm{O}}} + \frac{1}{z_{\mathrm{H}}^2 c_{\mathrm{H}}} \right)^{-1}. \tag{4}$$

Taking into account that the sample contains grains parallel to and in series with the direction of the current, the total chemical capacitance is

$$C_{\mathrm{chem,cal}} = \frac{e^2}{k_{\mathrm{B}}T} \frac{A}{L} G^2 \left(\frac{1}{z_{\mathrm{O}}^2 c_{\mathrm{O}}} + \frac{1}{z_{\mathrm{H}}^2 c_{\mathrm{H}}} \right)^{-1}. \tag{5}$$

The calculated values of the chemical capacitance through Eq. 5 are compared to $C_{\mathrm{chem,exp}}$ in Table 1.

Table 1. Experimentally determined chemical capacitance (using Eq. 2) compared to that calculated through Eq. 5. The characteristic frequency ω_0 used in Eq. 2 is given. The ratio of oxygen vacancy to proton conductivity was determined from conductivity data in $\mathrm{H_2O/O_2}$ and $\mathrm{D_2O/O_2}$. The ratio of proton to oxygen vacancy mobility was estimated by assuming $\Delta H_{\mathrm{mob,H}} = 2/3\ \Delta H_{\mathrm{mob,O}}$. The ratio of oxygen vacancy to proton concentration was calculated from Eq. 3.

	ω_0 [Hz]	$C_{\mathrm{chem,exp}}$ [F]	$\frac{\sigma_{\mathrm{gi,O}}}{\sigma_{\mathrm{gi,H}}}$	$\frac{u_{\mathrm{H}}}{u_{\mathrm{O}}}$	$\frac{c_{\mathrm{O}}}{c_{\mathrm{H}}}$	$C_{\mathrm{chem,cal}}$ [F]
300 °C	~ 7	1.1 µ	10.6	231	$1.21 \cdot 10^3$	0.57 µ
360 °C	~ 25	0.72 µ	21.5	138	$1.48 \cdot 10^3$	0.43 µ
400 °C	~ 50	0.61 µ	30.2	103	$1.55 \cdot 10^3$	0.38 µ

The agreement between $C_{chem,exp}$ and $C_{chem,cal}$ is reasonable in view of the many assumptions used to calculate $C_{chem,cal}$. We also note that $C_{chem,exp}$ and $C_{chem,cal}$ both decrease with increasing temperature, in agreement with what we expect.

We have so far neglected the role that the electrodes might play on the overall electrical behaviour. If the grain boundaries in Ca-doped $Er_2Ti_2O_7$ can polarize the grains, it is also possible that the electrodes can do the same. Obviously, the electrodes are in our case not fully reversible (*cf.* Fig. 3A), enabling a possibility that the electrodes in our case are selectively blocking towards one of the charge carriers. We will in the following discuss the role of the electrodes on the overall electrical response in our system.

Fig. 10 compares impedance spectra recorded at 400 and 450 °C as a function of water vapour pressure under oxidising and reducing conditions.

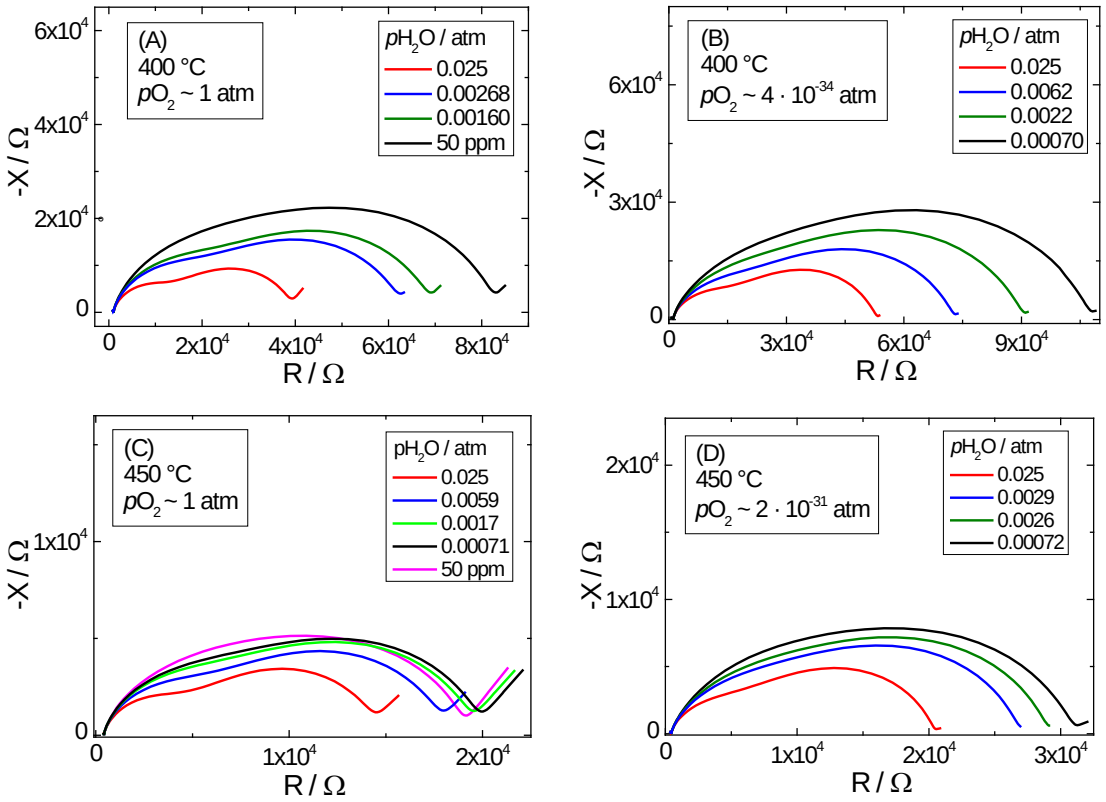

Fig. 10: Impedance spectra recorded for ETC2 as a function of pH_2O under oxidizing (left) and reducing (right) conditions at 400 °C (top) and 450 °C (bottom).

It is seen that the electrode resistance (arc 4) is reduced upon introduction of hydrogen, and that both R_2 and R_3 increases with decreasing pH_2O both under reducing and oxidising conditions. In other words, the essential characteristics of the grain boundary related process (as reflected by R_2) and the chemical polarization (as reflected by R_3) remain while changing pH_2O in both oxidising and reducing atmospheres, despite the change in the electrode resistance (R_4). Moreover, no significant effect of changing the oscillation voltage (within 2 mV – 2.5 V) on the impedance spectra recorded at 360 and 400 °C was observed. In total, this suggests that possible effects of electrode polarization are less than that caused by the grain boundaries under zero DC bias condition.

If electrode polarization is significant, the sample as a whole (from electrode to electrode) becomes polarized. The length scale of electrode polarization is therefore much longer than in the case of grain boundary polarization, *i.e.* 4 µm vs. 1.2 mm for ETC2. We would therefore expect that electrode polarization has a longer time constant. Thus, prior to recording impedance spectra as a function of DC bias, the time-dependent behaviour of the impedance at a constant frequency was recorded while applying DC bias. The frequency was set within the frequency range corresponding to that of arc 3, *e.g.* 2 Hz at 400 °C (cf. Fig. 3A and B). Representative time-dependencies of the real part of the impedance are shown in Fig. 11.

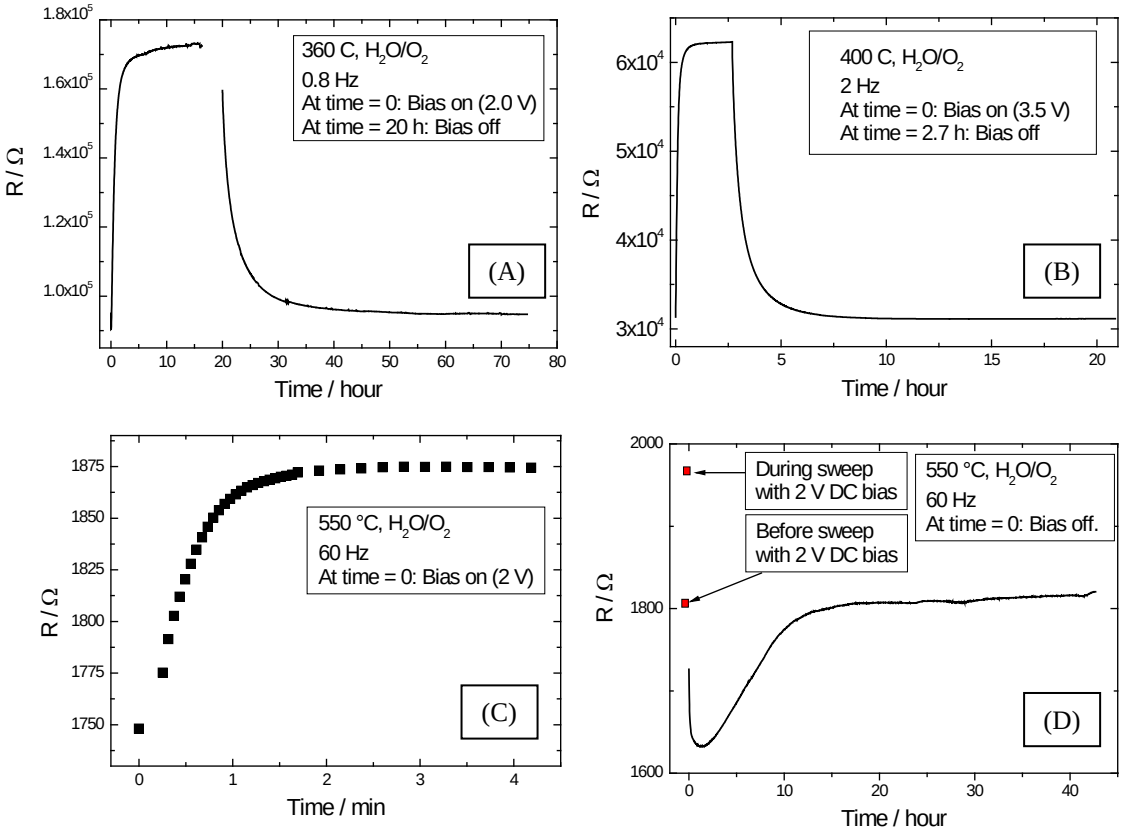

Fig. 11. Time-dependencies of the real part of the impedance upon and after application of bias at 360 (A), 400 (B) and 550 °C (C and D). The frequencies were set to a value corresponding to the frequency range of arc 3.

Upon application of bias, the impedance increased before levelling off after some time. At 360 and 400 °C (Fig. 11A and B), the impedance relaxed to its initial level in a "simple" manner when the DC bias was turned off. At 500 and 550 °C, the impedance initially decreased – rapidly reaching values lower than before the bias was applied – followed by a slow increase, eventually levelling off at the initial value. On basis of these observations, suitable waiting times were chosen so that impedance spectra were recorded when the impedance had become constant with time. Moreover, in order to ensure that no sample degradation took place upon application of bias, impedance spectra at zero bias were recorded in between those with DC bias.

Fig. 12 compares impedance spectra recorded at 360 and 550 °C as a function of water vapour pressure and applied DC bias.

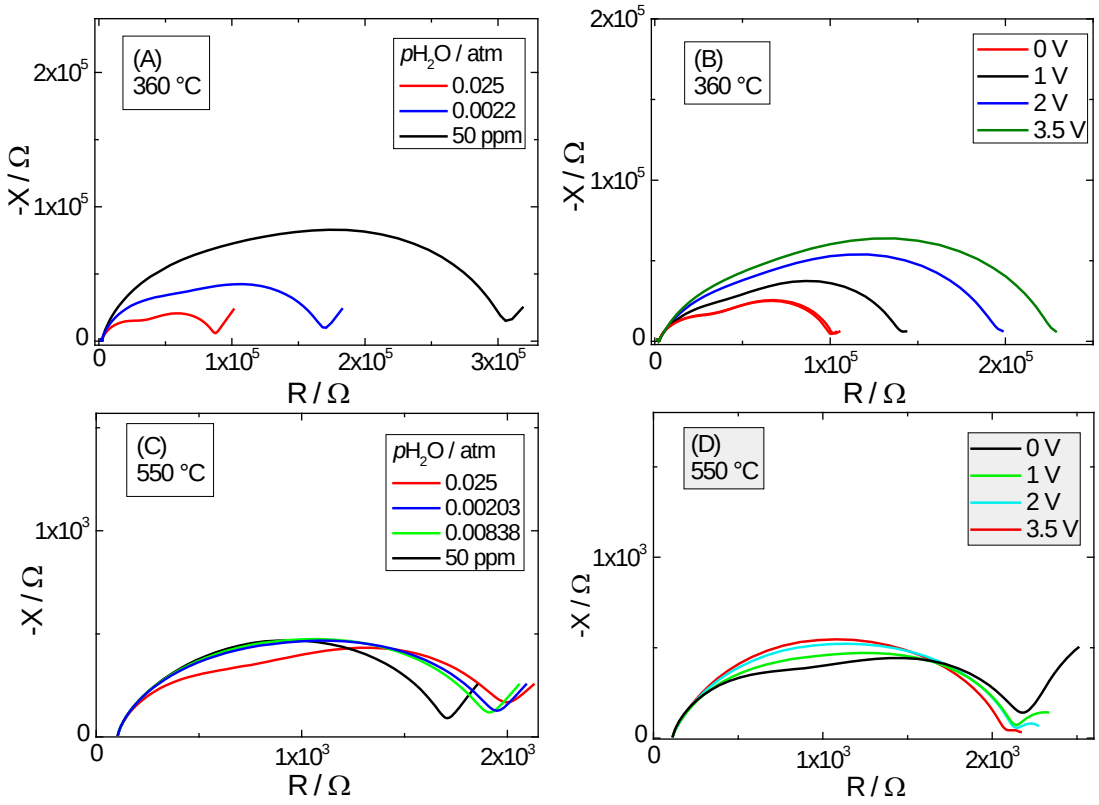

Fig. 12: Impedance spectra recorded under oxidizing condition for ETC2 as a function of pH_2O (left) and as a function of applied DC bias (right).

The electrode related resistance (R_4) decreases with increasing DC bias, which is typical for activation of electron-transfer reactions. Fig. 13 shows the DC bias dependence of R_2 – using the high frequency fitting approach – and it is seen that R_2 is increasing slightly with DC bias at 360 and 400 °C.

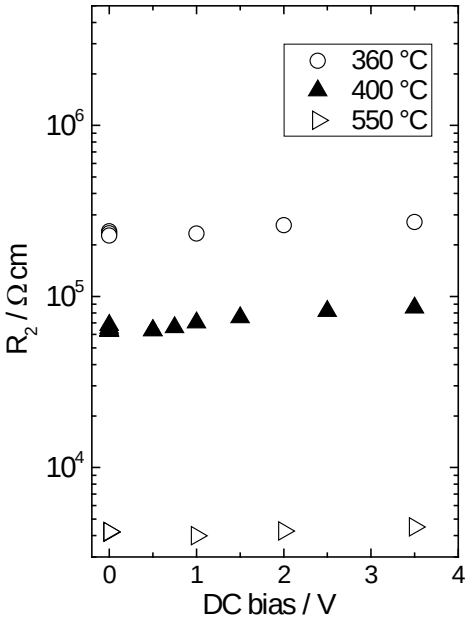

Fig. 13. The resistance of arc 2 as a function of DC bias in oxidising conditions for ETC2. R_2 was extracted from the impedance spectra from a fitting approach in which only the high frequency part of the spectra were fitted into $(R_1Q_1)(R_2Q_2)$ or $R_1(R_2Q_2)$.

The rather small change in R_2 implies that it is mainly R_3 which constitutes to the increase of R_2 + R_3 with increasing DC bias at 360 and 400 °C (*cf.* Fig. 12B). At 550 °C, R_2 is essentially independent of DC bias, whereas R_3 decreases slightly. It is interesting to note that applying a relatively small DC bias across the sample and decreasing pH_2O have similar effects on R_3. This indicates that also the electrodes can polarise the grains of ETC2.

Dependence of DC bias on the grain boundary resistance has previously been reported for acceptor doped CeO_2 [19,20] and $SrTiO_3$ [21,22]. In these studies, the charge carriers were reported to be depleted in the grain boundary space-charge layers, resulting in a relatively high grain boundary resistance, similar to the situation in this study. The authors reported a decrease in the grain boundary resistance when the applied DC bias per grain boundary was in the order of hundreds of mV; thus comparable with the space-charge potentials in the materials.[2] The decrease in the grain boundary resistance in CeO_2 was attributed to an overall increase in the concentration of charge carriers in the space-charge layers upon application of DC bias [20].

In the present study, up to 3.5 V DC was applied on ETC2. This sample had an average grain size of ~ 4 µm and a sample thickness of 1.2 mm, making the current pass on average 300 grain boundaries between the electrodes. Thus, assuming that the grain boundaries were the only cause for the 3.5 V voltage drop, the average voltage drop per grain boundary was 3.5 V / 300 ~ 12 mV, much lower than typical values for space-charge potentials. The fact that the grain boundary resistance (as reflected by R_2) in our case increases slightly at the lower temperatures with increasing DC bias also disagrees with an anticipated increase in concentration of the depleted charge carriers upon application of DC bias. We therefore conclude that the reason for the observed effects of DC bias on ETC2 is different from what was discussed above for CeO_2 and $SrTiO_3$.

In order to understand the DC bias dependence of the recorded impedance spectra, it may be fruitful to first picture how the grain boundaries polarize the individual grains. We expect that this happens on a rather short timescale (rather high frequencies) due to the short length scale of the grains, hence making it observable in the impedance spectra. The concentration profiles of oxygen vacancies and protons within the individual grains on a time scale reflected by arc 3 are schematically shown in Fig. 14A. The concentration profile of the oxygen vacancies is created as a result of the blocking of oxygen vacancies at the grain boundaries. Due to the requirement of local electroneutrality, the proton profile changes accordingly.

[2] Reported space-charge potentials for CeO_2 range from 0.3 to 0.5 V [23,24] and for $SrTiO_3$ from 0.5 to 1.8 V [25].

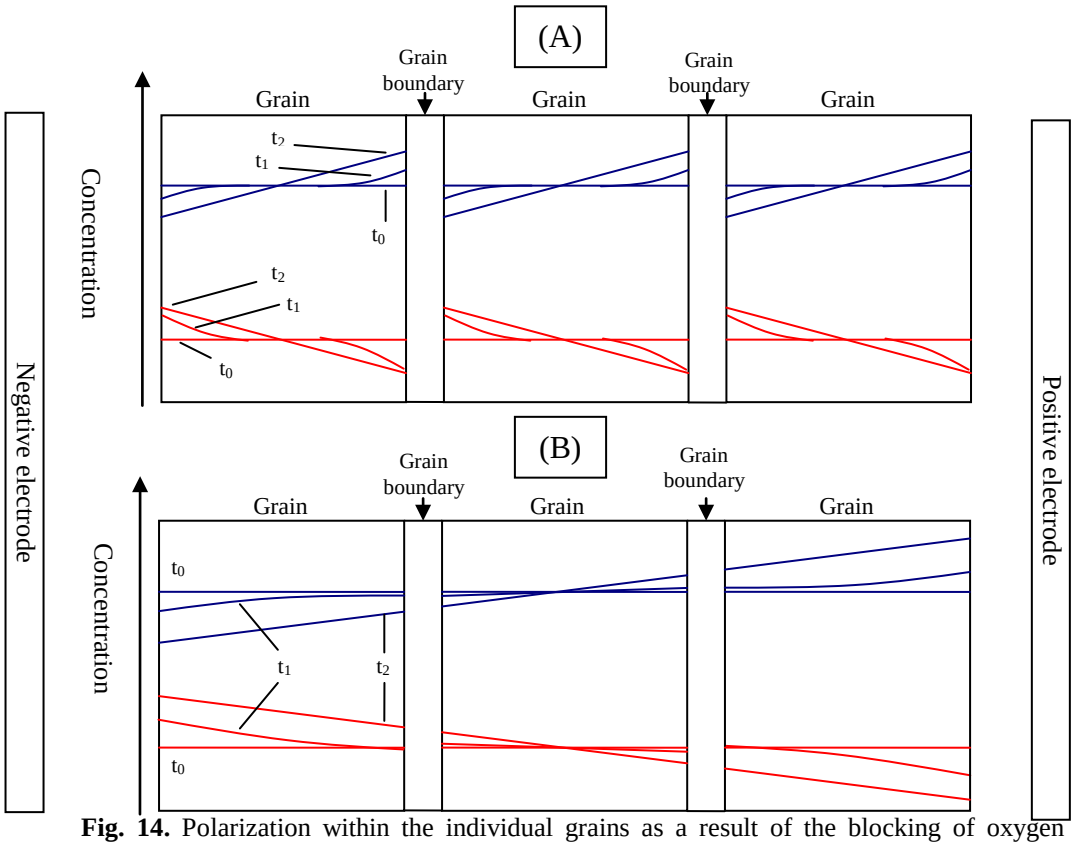

Fig. 14. Polarization within the individual grains as a result of the blocking of oxygen vacancies at the grain boundaries (A) and within the sample as a whole as a result of blocking of oxygen vacancies at the electrodes (B). The concentration profiles of oxygen vacancies are sketched in blue, protons in red. The different concentration profiles correspond to different times (*i.e.* different frequencies during an impedance spectrum). In (A) t_0 corresponds to high frequencies (within arc 1 and arc 2), t_1 and t_2 corresponds to lower frequencies within arc 3. In (B), the indicated times corresponds to lower frequencies than recorded in the impedance spectra.

On the other hand, upon application of a DC bias, the partially blocking electrodes may add to the polarization of the grains. In this case, the concentration profiles extend across the whole sample. The time dependencies given in Fig. 11 suggest that a rather long time constant is associated with this polarization, in line with the length scale of the entire sample as compared to individual grains. The concentration profiles that evolve during the electrode polarization are sketched in Fig. 14B, and it is seen that the grain boundaries close to the positive electrode will contain fewer protons with time, whereas an increase will be encountered on the left hand side. Then, during the recording of the impedance spectra with DC bias, we are probing concentration profiles caused from both electrode and grain boundary polarization. Consequently, when the DC bias has acted for sufficiently long time, the measured R_3 is larger than at zero bias.

We should finally consider how the concentration profiles that pass through the whole sample may influence on the grain boundary resistance, as reflected by R_2. After polarization, the grain boundaries close to the negative electrode of Fig. 14B should exhibit higher proton conductivity and the grain boundaries close to the positive electrode should exhibit lower proton conductivity. It is not straightforward to estimate the overall effect of the proton concentration profile on R_2 as the

measured resistance reflects the resistance of all of the grain boundaries. We may initially guess that the effect on R_2 of moving protons from one side of the sample to the other should average out, in total leaving R_2 essentially unchanged. On the other hand, as compared to the high frequency situation at zero DC bias (*cf*. Fig. 14A, $t = t_0$), the concentrations of protons and oxygen vacancies at the opposite interfaces between grain interior and the space-charge layers are no longer equal, as indicated in Fig. 14B. In turn, this asymmetry in concentrations may lead to a reduced overall proton concentration in the space-charge layers, which in turn may increase the grain boundary resistance as reflected by R_2. We should also take into account that the DC bias dependences of R_2 at 360 and 400 °C are rather small – at least smaller than the water vapour dependences of R_2 (Fig. 9). We realise that at present we can not provide a satisfactorily explanation for a possible positive DC bias dependences of R_2.

4. Summary and concluding remarks

The electrical properties of ceramics of $(Er_{1-x}Ca_x)_2Ti_2O_{7-x}$ (x = 0.02 and 0.005) with low and high contents of Si impurities at the grain boundaries were investigated. In grain interior, oxygen vacancies were found to be the major charge carrier, with protons as a minor contributor at the lower temperatures. For all samples, the complex impedance revealed two additional processes – with associated capacitances in the "grain boundary range" – which were dependent on water vapour pressure and hydrogen isotope. We therefore suggested that protons inherently play a role in the grain boundary related properties of Ca-doped $Er_2Ti_2O_7$.

The resistance associated to the second arc decreased with increasing water vapour pressure, and displayed a relatively higher water vapour dependency than that of the grain interiors. We suggested assigning this resistance to the resistance of the space-charge layers adjacent to the grain boundary core, in agreement with the seemingly inherent nature of the electrical properties of this contribution. Since the oxygen vacancies are doubly charged, their depletion will be quadratic compared to the singly charged protons in the space-charge layers. This makes the role of the protons as charge carriers in the space-charge layers more prominent.

The impedance of the third contribution in the Nyquist plots was suggested to be caused by chemical polarization induced by grain boundaries. This was supported by the tear-drop shape of this contribution, the different response on the characteristic frequency when changing either the water vapour pressure or the hydrogen isotope in the surrounding gas, and a good agreement between the experimentally and calculated value for the chemical capacitance.

The effect of applying a DC bias during the impedance measurements was investigated on one sample. A significant effect on the impedance related to the chemical polarization was seen upon application of DC signals in the range 0.5–3.5 V, while that of the space-charge layers changed much less. It was observed that the DC signal dependency on the impedance of the third contribution was similar to that of water vapour pressure, indicating that also the electrodes can polarise the grains of Ca-doped $Er_2Ti_2O_7$.

To the best knowledge of the author, the present contribution is the first report of chemical polarization in a mixed oxide ion and protonic conductor. In order to further investigate the different aspects related to this, samples with well defined microstructures or preferentially a bi-crystal should be beneficial. Obviously, it would also be interesting to investigate other material systems which exhibit mixed ionic conductivity.

Acknowledgements

The author wishes to thank Dr. Despoina Maria Kepaptsoglou, Department of Physics, University of Oslo, for carrying out the TEM investigations.

References

[1] X. Guo, J. Fleig, J. Maier, J. Electrochem. Soc. 148 (2001) J50.
[2] X. Guo, J. Fleig, J. Maier, Solid State Ionics 154-155 (2002) 563.
[3] H. Fjeld, R. Haugsrud, A.E. Gunnaes, T. Norby, Solid State Ionics 179 (2008) 1849.
[4] J.M. Porras-Vazquez, A.G. De la Torre, E.R. Losilla, M.A.G. Aranda, Solid State Ionics 178 (2007) 1073.
[5] K. Amezawa, J.-i. Yamada, N. Kitamura, Y. Tomii, T. Handa, N. Yamamoto, Solid State Ionics 176 (2005) 341.
[6] X. Guo, R. Waser, Progress in Materials Science 51 (2006) 151.
[7] J. Jamnik, X. Guo, J. Maier, Applied Physics Letters 82 (2003) 2820.
[8] J. Jamnik, Chemical and Biochemical Engineering Quarterly 21 (2007) 15.
[9] W. Lai, S.M. Haile, J. Am. Ceram. Soc. 88 (2005) 2979.
[10] W.C. Chueh, W. Lai, S.M. Haile, Solid State Ionics 179 (2008) 1036.
[11] J. Jamnik, J. Maier, J. Electrochem. Soc. 146 (1999) 4183.
[12] J. Jamnik, J. Maier, S. Pejovnik, Electrochimica Acta 44 (1999) 4139.
[13] T. Norby, Solid State Ionics 28-30 (1988) 1586.
[14] B.A. Boukamp, Equivalent circuit for Windows Ver. 1.2 (2008).
[15] E.E. Erickson, D. Gray, K. Taylor, R.T. Macaluso, L.A. LeTard, G.S. Lee, J.Y. Chan, Mater. Res. Bull. 37 (2002) 2077.
[16] J. Jamnik, J. Maier, Physical Chemistry Chemical Physics 3 (2001) 1668.
[17] J. Jamnik, Solid State Ionics 157 (2003) 19.
[18] H. Fjeld, D.M. Kepaptsoglou, R. Haugsrud, T. Norby, Solid State Ionics 181 (2010) 104.
[19] X. Guo, S.B. Mi, R. Waser, Electrochemical and Solid State Letters 8 (2005) J1.
[20] R. Meyer, X. Guo, R. Waser, Electrochemical and Solid State Letters 8 (2005) E67.
[21] I. Denk, J. Claus, J. Maier, J. Electrochem. Soc. 144 (1997) 3526.
[22] S. Rodewald, J. Fleig, J. Maier, J. Am. Ceram. Soc. 84 (2001) 521.
[23] X. Guo, W. Sigle, J. Maier, J. Am. Ceram. Soc. 86 (2003) 77.
[24] H.J. Avila-Paredes, K. Choi, C.-T. Chen, S. Kim, J. Mater. Chem. 19 (2009) 4837.
[25] R.A. De Souza, Physical Chemistry Chemical Physics 11 (2009) 9939.

5. Summarizing discussion and outlook

The articles making up this thesis have addressed different factors that affect ionic transport in oxides. In PAPER I we investigated the proton mobility in $LaNbO_4$ through a second order phase transition. In the remaining three PAPERs II-IV and MANUSCRIPT A, focus was on the influence of grain boundaries on the overall ionic transport in polycrystalline samples. This chapter extends and links the discussions within PAPER II, III and IV and MANUSCRIPT A, and will at certain points be more speculative than in the individual works.

5.1 Space-charge layer effects in ionic conductors

On basis of literature that have emerged the two last decades, it has become evident that grain boundaries in many solid oxidic ionic conductors are intrinsically more resistive than the grain interiors. Fluorite and perovskite structured oxides, in which oxygen diffusion proceeds according to an oxygen vacancy mechanism, have so far attracted most attention. The inherent low ionic conductivity of grain boundaries has been reported to originate from depletion of oxygen vacancies in negatively charged space-charge layers in the vicinity of the positively charged grain boundary core. Examples from the literature include stabilized ZrO_2 [1-4], CeO_2 [5-8], $LaGaO_3$ [9-11], and $SrTiO_3$ [12,13]. For CeO_2, electrons accumulate in the space-charge layers, resulting in additional n-type electronic conductivity in the grain boundaries [5]. The depletion of the doubly charged oxygen vacancies is quadratic compared to the singly charged electron holes. This results in a higher electronic transport number in the grain boundaries compared to that of the grain interiors in both $LaGaO_3$ [9,10] and $SrTiO_3$ [12,13].

The investigation of BZY (PAPER II) revealed that the grain boundaries conducted electrons in addition to protons, analogous to the situation in CeO_2. Based on annealing experiments of $LaNbO_4$ undertaken in various atmospheres (PAPER III), the grain boundary conductivity of $LaNbO_4$ was found to exhibit a higher functional dependency on water vapour pressure than the grain interior conductivity does. We rationalised this behaviour by noting – as above – that the concentration of doubly charged oxygen vacancies should decay much more steeply in the space-charge layers than that of the singly charged protons. The situation is similar to that of singly charged electronic defects vs. oxygen vacancies in $LaGaO_3$ and $SrTiO_3$. Similar results were also obtained in the case of $Er_2Ti_2O_7$ (PAPER IV and MANUSCRIPT A); the relative contribution of protons to the grain interior conductivity (dominated by oxide ions) was here, however, lower than for $LaNbO_4$. All together, this

shows that the grain boundary core-space-charge layer model can be successfully applied on oxides that conduct protons.

For perovskite structured $SrTiO_3$, which is probably the most studied oxide with respect to space-charge effects, the vast amount of studies point to an accumulation of oxygen vacancies being the origin of the positive charge in the grain boundary core (see Ref. 14 and references therein). The same seems to hold for fluorite structured ZrO_2 and CeO_2 [15,16]. It is therefore interesting to note that negatively charged space-charge layers also can be concluded to exist and play a role in oxides with other types of crystal structures than the fluorite-type and perovskite structures, *i.e.* the fergusonite-type structure ($LaNbO_4$) and the pyrochlore structure ($Er_2Ti_2O_7$).

A positively charged core can result from a surplus of one or more types of positively charged defects, comprising oxygen vacancies, protons, cation interstitials and electron holes. The core will also become positively charged if acceptors, oxygen interstitials, cation vacancies or electrons are depleted from the core. In line with the argumentation given by De Souza in Ref. 14, we can rule out the native negatively charged defects (*i.e.* except the acceptor), because in $LaNbO_4$ and $Er_2Ti_2O_7$ they are too few that their depletion alone would create a high enough charge in the core. Since the band gaps of these oxides are rather high, the concentration of electron holes is probably low, suggesting that also a possible electron hole accumulation in the core is not the main contributor to the core charge. One may argue that due to elastic misfit between the acceptor and the host cation, the acceptor concentration is possibly higher in the core than in the grain interiors. Assuming that formation of cation interstitials in $LaNbO_4$ and $Er_2Ti_2O_7$ is energetically difficult due to the high charge number of the cations, we are left with accumulation of oxygen vacancies and protons as the probable reason for the positively charged core in $LaNbO_4$ and $Er_2Ti_2O_7$. On these bases, it is tempting to speculate that the formation of oxygen vacancies (and/or protons after hydration) in the grain boundary core is a common feature for oxides that form oxygen vacancies upon acceptor doping.

For the spinel $MgO \cdot nAl_2O_3$, the grain boundary core charge was reported to be negative [17,18]. It was suggested that magnesium vacancies, and not oxygen interstitials, residing in the core were responsible for the minus core charge [18]. Theoretical calculations have shown that anti-site defects ($Al_{Mg}^{\bullet}$ and $Mg_{Al}^{/}$) dominate in $MgO \cdot nAl_2O_3$ [19]. According to the same study, cation vacancies have lower formation energies than the anion Frenkel reaction. We, therefore, speculate that also in this case, the majority defect in the core is an intrinsic defect which has a favourable defect formation energy in grain interior.

Finally, it is interesting to mention rutile TiO_2 where the core charge shifts from positive to negative upon switching from acceptor to donor dopant [20,21]. The authors suggest that for

donor-doped TiO_2, cation vacancies form in the core. In acceptor doped TiO_2 either oxygen vacancies or cation interstitials could be the reason for the positively charged core; however, the authors suggest cation interstitials as the most probable. Thus, also in the case of TiO_2, intrinsic defects (and not the dopant) seem to rule the sign of the core charge.

5.2 Grain boundary core hydration

In PAPER II we proposed that the space-charge potential in $BaZrO_3$ changes as a function of water vapour pressure by suggesting a defect reaction where oxygen ions residing in the grain boundary core are preferentially protonated while the oxygen vacancies in the grain interior are preferentially filled, altogether increasing the positive charge of the core. We will in the following elaborate further on this concept in light of some recent publications.

As discussed in Section 5.1, a positively charged grain boundary core will form when oxygen vacancies redistribute from grain interior to the grain boundary core. For a material where ionic defects dominate at the expense of electronic defects (concentration wise), we would expect that the charge of the grain boundary core is unaffected by pO_2 and, correspondingly, that the space-charge potential is unchanged while changing pO_2. In oxides which accommodate cations with various valence states, electronic defects become more important and may contribute significantly to the core charge. A negative pO_2 dependency of the ratio of grain boundary resistance to grain interior resistance has been observed for two bicrystals of Fe-doped $SrTiO_3$: one with a symmetrical low-angle grain boundary of tilt angle = 5.4 ° [22], and one with a mixed asymmetrical grain boundary of asymmetrical tilt angle = 12 ° [23]. Consequently, for these bicrystals the space-charge potential decreases with increasing pO_2. On basis of the various models proposed in Ref. 14, it seems as the decrease in the space-charge potential with pO_2 occurs because the acceptors (Fe^{3+}) in the grain interiors becomes oxidised. This results in a lower bulk concentration of oxygen vacancies, eventually leading to a slight decrease in the space-charge potential with increasing pO_2.

If protons in the form of hydroxide ions can settle in the core, they compete with oxygen vacancies for the same core sites. The concentration of both species in the core will in that case depend on their grain interior concentrations (which are tuneable by means of pH_2O and temperature), the Gibbs energy change in redistributing one defect from grain interior to the core ($\Delta g_{V_O^{\bullet\bullet}}$ and $\Delta g_{OH_O^{\bullet}}$), the loss in configurational entropy due to the confinement of the species in the grain boundary core and the electrostatic energy expended in the redistribution of the charged species. This scenario was considered by De Souza [14], and it was shown that the concentration of protons in the core could exceed that of the oxygen vacancies when $\Delta g_{V_O^{\bullet\bullet}}$ and $\Delta g_{OH_O^{\bullet}}$ were rather equal – even for a much smaller grain interior proton

concentration. In this respect, it may be commented that the preferential redistribution of protons occurs as a result of the less amount of electrostatic energy expended on the redistribution of the singly charged protons. The effect of electrostatics makes the redistribution of protons increasingly favourable compared to the oxygen vacancies with increasing $|\Delta g_{\mathrm{def}}|$.

The above analysis implies that additional sites in the core, which are not occupied by oxygen vacancies, can be filled by protons (hydroxide groups), resulting in an increased core charge. This is in line with the hydration reaction we suggested in PAPER II

$$\mathrm{H_2O(g)} + \mathrm{V}_{\mathrm{O,gi}}^{\bullet\bullet} + 2\mathrm{O}_{\mathrm{O,core}}^{\mathrm{x}} = \mathrm{O}_{\mathrm{O,gi}}^{\mathrm{x}} + 2\mathrm{OH}_{\mathrm{O,core}}^{\bullet}.$$

Thus, if $\Delta g_{\mathrm{V_O^{\bullet\bullet}}}$ is moderate (making some core sites available), an increased space-charge potential is to be expected if $p\mathrm{H_2O}$ is increased, as we observed for BZY in PAPER II. However, if all available core sites are already occupied by oxygen vacancies due to a high $|\Delta g_{\mathrm{V_O^{\bullet\bullet}}}|$, a change in $p\mathrm{H_2O}$ will not influence the space-charge potential. Based on the estimated protonic grain interior and grain boundary conductivity for $\mathrm{LaNbO_4}$, it appears that the space-charge potential is independent of $p\mathrm{H_2O}$ under the experimental conditions investigated in this thesis. Correspondingly, oxygen vacancies govern the core charge in $\mathrm{LaNbO_4}$ under the investigated conditions, implying that $\Delta g_{\mathrm{V_O^{\bullet\bullet}}}$ is more negative than $\Delta g_{\mathrm{OH_O^{\bullet}}}$.

5.3 Chemical polarization in mixed proton and oxide ion conductors

In PAPER IV and MANUSCRIPT A we suggested that selectively blocking grain boundaries induced chemical polarization in the grains of Ca-doped $\mathrm{Er_2Ti_2O_7}$. Does the same phenomenon occur in other oxides with mixed proton and oxide ion conductivity? If so, under what experimental conditions can we expect to observe this?

In a polycrystal, the grains will become chemically polarized if the transport numbers are different in grain interior and in the grain boundaries. If negatively charged space-charge layers govern the grain boundary resistance, protons will always be more predominating as charge carriers than oxygen vacancies in the grain boundaries as compared to in the grain interiors. Hence, we would not expect chemical polarization in relatively pure proton conductors. This is probably the reason why no impedance related to chemical polarization seemed to appear in the impedance spectra for $\mathrm{BaZrO_3}$ and $\mathrm{LaNbO_4}$ under the experimental conditions investigated here.

In MANUSCRIPT A, we derived an expression for the total chemical capacitance, and it was found to be proportional to the average grain size squared. In our case, when the measured

chemical capacitance was multiplied by the geometric factor of the samples (sample thickness divided by electrode area) to obtain a capacitance value in units of F/cm, the value was in the high-end of the range which is commonly assigned to transport across grain boundaries. With a smaller grain size, the measured chemical capacitance could be much smaller. It is therefore possible that the grain boundary impedance and the contribution related to chemical polarization merge when observed in a Nyquist plot. With larger grain size, we may expect values in the “electrode range”. We therefore speculate that some previous investigators of mixed proton and oxide ion conductors have interpreted chemical polarization impedance as impedance related to the processes taking place at the electrodes.

With increasing temperature, an oxide that contains protons will dehydrate and form oxygen vacancies. Mixed proton and oxide ion conductivity is therefore to be expected at elevated temperatures. With increasing temperatures, mobilities are also increasing, and the resulting conductivity for an oxide with mixed proton and oxide ion conductivity could therefore be so high that the time constant of the chemical polarization is too high to be observed in a Nyquist plot.

5.4 Outlook

This thesis has addressed ionic transport in oxides on different length scales. By means of first principles calculations, the proton migration path was investigated on an atomic level. Space-charge layers have a spatial extent in the order of nanometres and can therefore be considered as a nanodimensional structure. The role that space-charge layers play for the concentrations of different charge carriers have been studied indirectly by electrical measurements and observed using transmission electron microscopy. Finally, the transport properties of homogenous grains, typically µm-sized, have been studied.

In the race for better electrochemical energy converters, one may say that two strategies are pursued; one that searches for novel materials, and one that aims to improve already existing materials and technology. For both strategies, knowledge about the ionic transport on various length scales is decisive. With the arsenal of complex fabrication techniques that emerges, it is expected that transport in nanodimensional regions can be tuned. In turn, this will lead to substantial improvements in the performance of electrochemical energy converters.

References for Chapter 5 (Summarizing discussion and outlook)

[1] X. Guo, Solid State Ionics 81 (1995) 235.
[2] X. Guo, physica status solidi a, 183 (2001) 261.
[3] X. Guo, W. Sigle, J. Fleig, J. Maier, Solid State Ionics 154-155 (2002) 555.
[4] T. Nakagawa, I. Sakaguchi, N. Shibata, K. Matsunaga, T. Yamamoto, H. Haneda, Y. Ikuhara, Journal of Materials Science 40 (2005) 3185.
[5] X. Guo, W. Sigle, J. Maier, Journal of the American Ceramic Society 86 (2003) 77.
[6] T.S. Zhang, J. Ma, H. Cheng, S.H. Chan, Materials Research Bulletin 41 (2006) 563.
[7] H.J. Avila-Paredes, S. Kim, Solid State Ionics 177 (2006) 3075.
[8] H.J. Avila-Paredes, K. Choi, C.-T. Chen, S. Kim, Journal of Materials Chemistry 19 (2009) 4837.
[9] H.J. Park, S. Kim, Journal of Physical Chemistry C 111 (2007) 14903.
[10] H.J. Park, S. Kim, Solid State Ionics 179 (2008) 1329.
[11] S. Kim, Monatshefte für Chemie 140 (2009) 1053.
[12] X. Guo, J. Fleig, J. Maier, Journal of the Electrochemical Society 148 (2001) J50.
[13] X. Guo, J. Fleig, J. Maier, Solid State Ionics 154-155 (2002) 563.
[14] R.A. De Souza, Physical Chemistry Chemical Physics 11 (2009) 9939.
[15] Y.Y. Lei, Y. Ito, N.D. Browning, T.J. Mazanec, Journal of the American Ceramic Society 85 (2002) 2359.
[16] A. Tschöpe, Journal of Electroceramics 14 (2005) 5.
[17] Y.M. Chiang, W.D. Kingery, Journal of the American Ceramic Society 73 (1990) 1153.
[18] N. Nuns, F. Beclin, J. Crampon, Journal of the American Ceramic Society 92 (2009) 870.
[19] J.A. Ball, S.T. Murphy, R.W. Grimes, D. Bacorisen, R. Smith, B.P. Uberuaga, K.E. Sickafus, Solid State Sciences 10 (2008) 717.
[20] J.A.S. Ikeda, Y.M. Chiang, Journal of the American Ceramic Society 76 (1993) 2437.
[21] J.A.S. Ikeda, Y.M. Chiang, A.J. Garrattreed, J.B. Vandersande, Journal of the American Ceramic Society 76 (1993) 2447.
[22] R.A. De Souza, J. Fleig, J. Maier, Z.L. Zhang, W. Sigle, M. Ruhle, Journal of Applied Physics 97 (2005.
[23] Z.L. Zhang, W. Sigle, R.A. De Souza, W. Kurtz, J. Maier, M. Ruhle, Acta Materialia 53 (2005) 5007.

List of abbreviations and notation

$Acc^{/}$	Acceptor dopant
c	Volume concentration
D	Random diffusion coefficient
e	Elementary charge
F	Faraday's constant
f	Frequency
j	$j = \sqrt{-1}$
K	Equilibrium constant
k_B	Boltzmann's constant
L_D	Debye length
N_{gi}	Density of grain interior sites
N_c	Density of grain boundary core sites
p	Partial pressure
$Q(x)$	Net charge density in the space-charge layer
Q_c	Grain boundary charge per unit area
R	Ideal gas constant
T	Absolute temperature
u	Electrical mobility
u_0	Pre-exponential term of mobility
w_c	Grain boundary core width
X	Site fraction
z	Charge number

Γ_0 Attempt frequency

$\Delta_d G^0$ Standard molar Gibbs energy of the defect reaction

$\Delta_d H^0$ Standard molar enthalpy of the defect reaction

ΔH_{mob} Enthalpy of mobility

$\Delta_d S^0$ Standard molar entropy of the defect reaction

$\Delta\varphi(0)$ Space-charge potential

ε Permittivity

ε_0 Vacuum permittivity

ε_r Dielectric constant

η Electrochemical potential

λ^* Space-charge layer width

μ Chemical potential

σ Conductivity

τ_0 Relaxation frequency

φ Electric potential

ω Angular frequency

ω_0 Characteristic frequency

Superscripts and subscripts

Conductivity: H and O are used as subscripts to denote proton and oxide ion conductivity, respectively. When the locus of the conductivity has to be specified, gi and gb are used as subscripts for grain interior and grain boundaries, respectively. When necessary, they are combined and separated with a comma, *e.g.* $\sigma_{gb,H}$ for grain boundary proton conductivity.